A comprehensive atlas of the aging vertebrate brain reveals signatures of progressive proteostasis dysfunction

Domenico Di Fraia[1,*], Antonio Marino[1,*], Jae Ho Lee[2,*], Erika Kelmer Sacramento[1], Mario Baumgart[1], Sara Bagnoli[3], Pedro Tomaz da Silva[4,5], Amit Kumar Sahu[1], Giacomo Siano[3], Max Tiessen[1], Eva Terzibasi-Tozzini[3], Julien Gagneur[4,6,7], Judith Frydman[2,#], Alessandro Cellerino[1,3,#], and Alessandro Ori[1,#,$]

[1] Leibniz Institute on Aging - Fritz Lipmann Institute (FLI), Jena, Germany
[2] Department of Biology, Stanford University, Stanford, CA, USA
[3] BIO@SNS, Scuola Normale Superiore, Pisa, Italy
[4]School of Computation, Information and Technology, Technical University of Munich, Garching, Germany
[5] Munich Center for Machine Learning, Munich, Germany
[6] Computational Health Center, Helmholtz Center Munich, Neuherberg, Germany
[7] Institute of Human Genetics, School of Medicine, Technical University of Munich, Munich, Germany

* Equal contribution
# Correspondence should be address to: jfrydman@stanford.edu , alessandro.cellerino@leibniz-fli.de or alessandro.ori@leibniz-fli.de
$ Lead contact

ABSTRACT

Protein homeostasis is disrupted in aging and neurodegenerative diseases, yet, the specific impact of aging on brain proteostasis remains poorly understood. Here, we measured and integrated the effects of aging on the transcriptome, translatome, and multiple layers of the proteome in the brain of a short-lived killifish. We find that aging causes a decoupling between transcriptome and proteome. This leads to decreased abundance of proteins enriched in basic amino acids such as DNA/RNA-binding proteins and increased levels of others, independent of mRNA changes. Chronic proteasome impairment *in vivo* induces aging signatures in lysosomes and mitochondria. However, it does not recapitulate the age-related decoupling between transcripts and proteins. Instead, aberrant translation pausing and ensuing reduced ribosome availability reprogram the proteome independently of transcription. The age-linked changes in protein biogenesis likely enhance aggregation and reduce availability of key protein complexes, thus contributing to proteome dysfunction and aging hallmarks in older brains.

Keywords: brain, aging, proteome, translation, ribosome, proteasome, mitochondria, killifish, protein aggregation, post-translational modification

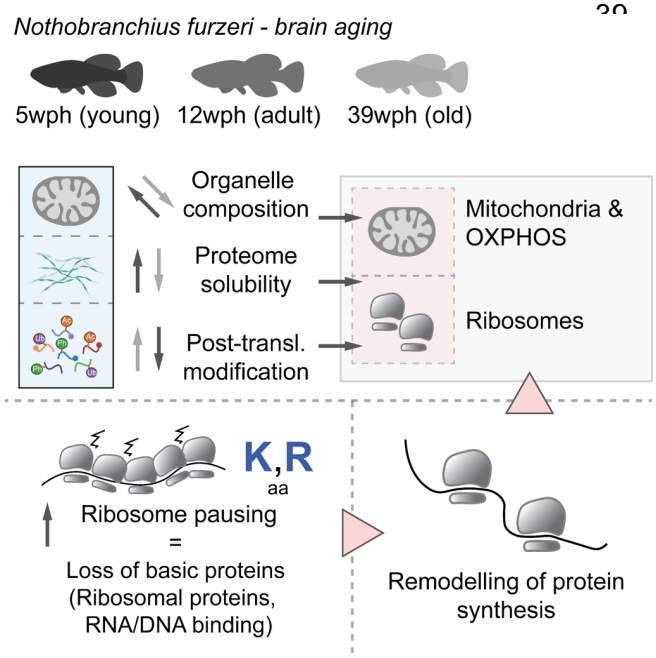

Highlights:

- A resource of protein solubility, organelle composition and PTMs in the aging vertebrate brain
- Proteostasis alterations converge on mitochondria, ribosomes and biosynthetic pathways
- Basic proteins, e.g., DNA/RNA binding, are reduced due to translation pausing
- Decreased ribosome availability reprograms protein synthesis in old brains

Introduction

Aging is the primary risk factor for most neurodegenerative diseases. Both aging and neurodegeneration are characterized by a disruption in protein homeostasis, also known as proteostasis, which ultimately leads to the progressive accumulation of protein aggregates. Proteostasis involves multiple mechanisms that maintain a balanced and functional proteome. These mechanisms include the regulated coordination of protein synthesis and degradation, as well as correct protein localization within cells, and fine-tuning of their function through post-translational modifications (PTMs). Preserving proteostasis is essential to ensure that an adequate supply of protein building blocks is available for assembling cellular structures such as multi-protein complexes and organelles. Additionally, it also prevents the accumulation of misfolded and "orphan" protein complex subunits that are susceptible to aggregation.

Several possible mechanisms are suggested to contribute to age-related proteostasis impairment in the brain (J. Labbadia and Morimoto 2015; Hipp, Kasturi, and Hartl 2019)For example, age-dependent enhanced ribosome collisions and stalling have been identified in old yeast cells and nematodes as leading to a decline in proteostasis through overwhelmed quality control pathways and increased aggregation (Stein et al. 2022). Age-dependent changes in protein synthesis have also been observed in rodents and other organs beyond the brain (Anisimova et al. 2020; Kluever et al. 2022; Ori et al. 2015). Further, accumulation of ribosomes at isolated 3'-UTR has been observed in mouse and human aging brains (Sudmant et al. 2018). On the other side, a decline in protein clearance pathways is also implicated in aging phenotypes (Vilchez, Saez, and Dillin 2014; Hansen, Rubinsztein, and Walker 2018). For instance, a partial decrease of proteasome activity, an early event during brain aging, can contribute to the loss of stoichiometry of the ribosome and other protein complexes (Kelmer Sacramento et al. 2020). Also, increased activity of deubiquitinating enzymes leads to the accumulation of a subset of proteins that can influence lifespan in nematodes (Koyuncu et al. 2021).

Although all these individual studies have documented changes in specific aspects of the transcriptome and proteome during aging, as well as age-dependent alterations in aggregation and post-translational modification, a comprehensive and coordinated analysis of these changes is currently lacking.

Understanding and integrating the impairment of proteostasis in the aging vertebrate brain is particularly relevant for human neurodegenerative diseases. We reason that to comprehend the mechanisms of proteostasis decline and its connections to other hallmarks of aging requires an integrative analysis. This should comprise the integration of several aspects of proteostasis in aging as well as their interplay and mechanistic relationships. To bridge the knowledge gap arising from the separate investigation of these aspects in different model systems, we conducted a comprehensive investigation of proteostasis in the aging brain of the short-lived killifish *Nothobranchius furzeri*. We chose killifish because of the spontaneous emergence of aging brain phenotypes, including cognitive decline (Valenzano et al. 2006), neuronal loss (S. Bagnoli et al. 2022), accumulation of protein aggregates (Matsui, Kenmochi, and Namikawa 2019), reduced proteasome activity (Kelmer Sacramento et al. 2020), aggregation of prion-like proteins (Harel et al. 2022), and mis-localization and aggregation of disease-relevant proteins, such as the RNA-binding protein TDP-43 (Louka et al. 2022).

Using this model system, we integrated biochemical and omics techniques to systematically measure the effects of aging on the transcriptome, translatome, and multiple layers of the proteome and applied computational approaches to investigate the relationships between these different aspects. We established a protocol for long-term partial inhibition of proteasome activity to investigate whether this specific perturbation of proteostasis is sufficient to replicate age-related brain phenotypes *in vivo*. Finally, we performed Ribo-Seq to directly assess the contribution of mRNA translation to proteome alterations and to quantify ribosome stalling and pausing in the aging vertebrate brain. Our analyses provide a compelling hypothesis to explain the lack of correspondence between transcriptome and proteome changes, an evolutionary conserved (Janssens et al. 2015; Wei et al. 2015; Walther et al. 2015; David et al. 2010; Takemon et al. 2021; Gerdes Gyuricza et al. 2022; Kelmer Sacramento et al. 2020), yet understudied aspect of age-related proteostasis impairment that has been linked to neurodegeneration in humans(Dick et al. 2023). We demonstrate that age-dependent translation dysfunction, leading to aberrant elongation pausing and increased aggregation can account for age-related alterations of the proteome independently of changes in mRNA levels.

Results

Multi-layer characterization of proteome alterations in the killifish aging brain

Aging can influence different aspects of protein homeostasis. To obtain an unbiased characterization of the effect of aging on the brain proteome we employed a multi-layered approach to interrogate major modes of protein regulation. We generated datasets describing changes in protein and mRNA levels, protein subcellular localization, detergent insolubility, and post-translational modifications (PTMs) in the aging brain of killifish (Figure 1A and S1A). First, we captured proteome-wide variation in subcellular localization using an approach based on differential centrifugation coupled with quantitative mass spectrometry (LOPIT-DC) (Geladaki et al. 2019) and analyzed pools of adult (12 weeks post-hatching = wph) and old (39 wph) killifish brains (Figure S1B, Table S1). We used a list of well-annotated organelle markers (Gatto, Breckels, and Lilley 2019) to evaluate organelle separation by LOPIT-DC (Figure 1B and S1C, D) and to confirm the reproducibility of organelles sedimentation between adult and old brains (Figure S1E). We then employed a tailored statistical approach (see methods, Figure S1F) to identify age-dependent changes in protein sedimentation profiles (Figure 1C, Table S1). The most prominent changes affected multiple mitochondrial and lysosomal proteins among others, including the mitochondrial transporters SLC25A32 and SLC25A18, and the lysosomal and vesicle trafficking proteins RAB14 and CCZ1 (Figure 1D). We interpret these alterations of sedimentation as an indication of partial reorganization of the mitochondrial and lysosomal proteome during aging that correlates with the well-described dysfunction of these organelles during aging and neurodegenerative diseases.

In parallel, we used the same pools of samples to assess age-dependent changes in protein solubility. We complemented our previous analysis of SDS insoluble aggregates in the killifish aging brain (Kelmer Sacramento et al. 2020) with a more fine-grained analysis of protein solubility. Thus, we exposed brain homogenates to a series of detergent combinations of increasing strength, separated soluble and insoluble fractions by ultracentrifugation (as described in (Tebbenkamp and Borchelt 2009), Figure S2A, Table S1), and quantified protein abundances across fractions using mass spectrometry. Principal component analysis showed reproducible detergent-based fractionation in adult and old brains (Figure S2B) and GO enrichment analysis confirmed the expected partitioning of cellular components as a function of detergent strength (Figure S2C and S2D). In agreement with previous findings from other species (Vecchi et al. 2020; Walther et al. 2015) and the spontaneous age-related accumulation of protein aggregates in killifish brain (Matsui, Kenmochi, and Namikawa 2019; Harel et al. 2022; Kelmer Sacramento et al. 2020), we observed an overall increase of protein detergent-insolubility in old samples (Figure S2E). By comparing detergent insolubility profiles between adult and old brains (Figure S2F-G), we identified 410 protein groups changing detergent insolubility with aging (Figure 1E, Table S1). While many of these proteins exhibited increased insolubility to detergents in old brains, there were instances where aging was linked to decreased insolubility to detergents. This indicates that factors other than protein aggregation, such as alterations in protein interactions or localization, could be responsible for the observed changes in detergent insolubility.

Next, we examined the effects of brain aging on multiple PTMs, using a sequential enrichment strategy followed by quantification of age-dependent changes in protein ubiquitylation,

acetylation, and phosphorylation in the aging brain (Figure S3A, Table S2). We quantified PTM-carrying peptides normalized for protein changes (see methods, Figure S3) and identified age-related changes for 534 phosphorylated, 618 ubiquitylated, and 190 acetylated peptides (P<0.05, Figure 1F). The general increase in the number of affected PTM peptides with aging emphasized its overall impact on the proteome beyond protein abundance (Figure 1F-G). Integration of phosphorylation data with experimentally derived kinase-substrate relationships (Johnson et al. 2023) indicates a remodeling of kinase signaling in the aging brain. Besides an increased activity (i.e., increased phosphorylation of predicted targets) for kinases involved in the regulation of immune responses, we reported enhanced activity for kinases of the protein kinase C family, e.g., PKN1, PKN2, PKCA, whose hyperactivation is linked to Alzheimer's disease (Alfonso et al. 2016; Morshed et al. 2021; Bai et al. 2020). Our data also reveals the decreased activity of kinases responsible for the phosphorylation of splicing factors and other RNA processing proteins, e.g. CDC2-like kinases 2 and 4 (CLK2 and CLK4, Figure 1H-I). These data suggest a convergence between aging and neurodegeneration concerning altered signaling pathways in the brain and hints at dysfunctional RNA processing in the aging brain.

To more systematically investigate the convergence between brain aging and neurodegenerative diseases, we queried our datasets for killifish orthologs of proteins encoded by genes that have been genetically linked to neurodegeneration in humans (Table S3). We found several of these proteins to be affected by aging in killifish in at least one of the proteomic datasets analyzed (Figure 1J). These include changes in subcellular fractionation and detergent insolubility (Figure S4A-B), as well as 23 PTM sites conserved between killifish and humans (Figure S4C-D-E). The microtubule-associated protein Tau (MAPT) was notably affected by aging across multiple proteomic layers. MAPT showed a prominent increase in detergent insolubility in old brains (Figure 1E), an alteration associated with human aging and neurodegenerative diseases (Guillozet et al. 2003; Chatterjee et al. 2023; Wang and Mandelkow 2015). Additionally, we detected an age-dependent increase in phosphorylation and ubiquitylation of conserved residues in the microtubule-binding domain (MBD) of MAPT, a region sensitive to PTMs and associated with Tau pathological aggregation (Figure 1K and S4D) (L. Li et al. 2022; Datta et al. 2021; Wang and Mandelkow 2015). We validated the spontaneous increase of MAPT/Tau phosphorylation in old killifish brains using immunofluorescence staining for a conserved phosphorylated epitope of Tau (AT100) (Figure 1L).

Together, our analyses comprehensively establish how aging affects the brain proteome along multiple axes beyond protein abundance, using a consistent model organism and age groups. This thorough characterization of the proteome reveals several potential connections between aging, specific molecular events, and genetic factors associated with neurodegeneration, which are relevant to humans. To make this resource easily accessible to the scientific community, we have developed a web application at https://genome.leibniz-fli.de/shiny/orilab/notho-brain-atlas/ (credentials will be available after final publication)

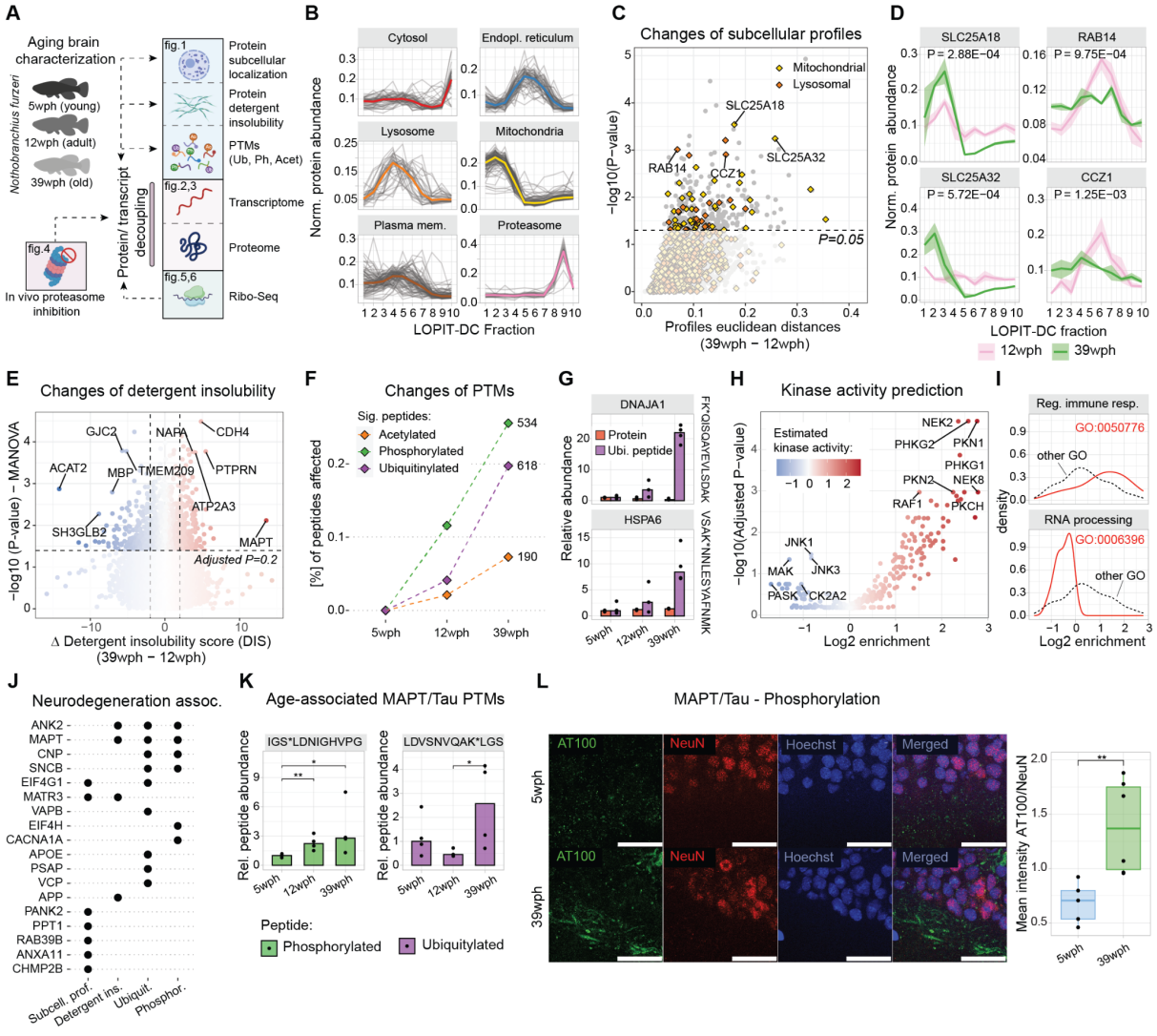

Figure 1: Aging affects protein subcellular localization, detergent insolubility and post-translational modifications. A) Overview of the datasets generated in this study (wph= weeks post-hatching). B) Organelle markers protein profiles from LOPIT-DC (12 wph). The x-axis indicates the different fractions of the LOPIT-DC experiment. The y-axis indicates protein distribution across fractions. The median profiles of each organelle are highlighted by a colored solid line. C) Scatterplot depicting protein relocalization scores in the aging killifish brain. The x-axis indicates the median replicate Euclidean distance of the profiles between the two conditions. Y-axis indicates the -log10 P-value of the Hotelling T-squared test between adult (12 wph) and old (39 wph) profiles (N=4 pools per age group). D) Examples of sedimentation profiles for selected proteins with altered subcellular fractionation profiles. In each of the plots, the x-axis indicates the 10 fractions obtained from LOPIT-DC. The y-axis indicates the total protein distribution along the 10 fractions for adult (12 wph, pink) and old (39 wph, green) fish. Shaded areas indicate 50% of the replicate distribution. P-values indicate the results of the Hotelling T2 test (N=4 pools per age group). E) Volcano plot depicting protein detergent insolubility changes in the aging killifish brain. The x-axis indicates the difference in detergent insolubility score (see methods) expressed as old vs. adult. Higher values indicate increased detergent insolubility in the old brain. Y-axis indicates the -log10 of the MANOVA test between adult and old profiles (N=4 pools per age group). Significant changes are highlighted by dashed lines (MANOVA adjusted P<0.2 and absolute Δ Detergent insolubility score >2). F) Post-translationally modified peptides affected by aging. The y-axis (left) indicates the percentage of affected sites in each dataset when compared to the young samples (*P*<0.05, moderated Bayes T-test, N=3-4). G) Barplots showing relative abundances of ubiquitylated peptides from DNAJA1 and HSPA6 across age groups (purple bars). The corresponding protein abundances are displayed as reference (red bars). On the side is reported the sequence of the identified peptide, N=3-4. H) Volcano plot showing changes in estimated kinase activity (using the algorithm from (Johnson et al. 2023)) based on phosphoproteomics data from old (39 wph) vs. young (5 wph) fish brains. The x-axis indicates changes in estimated kinase activity. The y-axis indicates FDR corrected -log10(P-value, Fisher's test). I) Density

distribution for kinases involved in the regulation of immune response (GO:0050776, upper panel) and RNA processing (GO:0006396, lower panel) against all other kinases from panel H. x-axis indicates the log2 Kinase activity enrichment value. J) Heatmap showing alterations of proteins linked to neurodegenerative diseases. Significant alterations in each dataset (P<0.05) are marked by black dots. K) Barplots displaying significantly changing (P<0.05, moderated Bayes T-test) MAPT/Tau phosphorylated (green) and ubiquitylated (purple) peptide. The values represent relative abundances to the young (5 wph) age group after correction for protein changes (see methods, Figure S3B). Asterisks indicate the P-value of the moderated Bayes T-test (N=3-4). L) (Left panel) Immunofluorescence stainings for phosphorylated (AT100) Tau in brain cryo-sections of young and old Nothobranchius furzeri. The stainings were normalized over the amount of NeuN in order to account for the different amounts of neuronal cells between young and old (N=5) animals. Scale bars = 20µm. (Right panel) Boxplot representation of mean intensity for phosphorylated Tau normalized over the amount of NeuN.The p-value indicates the results of a two-sample Wilcoxon test. *P ≤ 0.05; **P ≤ 0.01, ***P ≤ 0.001, ****P ≤ 0.0001. Related to Figure S1,S2,S3,S4 and Table S1,S2,S3.

Loss of basic proteins independently of transcription is a feature of the aging brain

We utilized our extensive datasets to investigate the mechanisms driving age-related changes in proteostasis. One intriguing hallmark of an aging brain, whose mechanisms are poorly characterized, is the loss of correlation between changes in gene transcripts (mRNA) and corresponding protein changes, a phenomenon known as "decoupling". The widespread occurrence of decoupling during aging across species suggests that it may be an important contributor to proteome dysfunction with age. To further investigate this aspect and how it might be connected to other proteome alterations, we combined our datasets with quantification of age-related changes in gene transcripts and protein levels which we obtained from proteomics and RNA sequencing (RNAseq) data (Figure 2A-B and S5A-H). By fitting a null distribution on the measured differences between protein and transcript changes, which we refer to as "decoupling score", we identified subsets of proteins displaying "positive protein-transcript decoupling", i.e., protein level higher than expected from changes of its corresponding transcript, or "negative protein-transcript decoupling", i.e., protein level lower than expected from changes of its corresponding transcript (Figure 2B and 2C, Table S4).

The decoupling scores displayed a median shift towards negative values (Figure 2C) due to an overall skew towards negative fold changes at the proteome level (Figure S5D), which was independent of sample normalization (Figure S5C). To assess the reproducibility of the decoupling metric, we compared the decoupling scores of this study to the decoupling scores of an independent transcriptome and proteome aging brain dataset that we previously generated (Kelmer Sacramento et al. 2020). Supporting our observations, there was a significant positive correlation between these datasets (Figure S5I), despite technical differences in the quantitative proteomics workflows: tandem-mass tags (TMT) based quantification (Kelmer Sacramento et al. 2020) compared to label-free Data Independent Acquisition (DIA, this study).

We then applied a multiple linear regression model to interrogate the association between the measured decoupling scores (response variable, N=1188 complete observation) and distinct biophysical properties of transcripts and proteins (N=9 features). Our model explained 31% of the decoupling variance (Adjusted R^2 = 0.31, Figure 2D). We detected estimated protein absolute abundance (see methods, **β**=0.36, P < 2.20E-16) and protein half-life (as described in (Fornasiero et al. 2018), **β**=0.31, P < 2.20E-16) as the parameters with the highest

correlation with positive decoupling (higher protein levels than expected from transcript changes, Figure 2E). On the other hand, the parameters with the highest correlation with negative decoupling (i.e. lower protein levels than expected from transcript changes) were relative transcript abundance (expressed as log2 transcripts per million (TPM) $\boldsymbol{\beta}$=-0.26, P < 2.20E-16) and proportion of basic amino acids ($\boldsymbol{\beta}$=-0.13, P = 4.30E-03, Figure 2D and 2E). We subsequently employed a second regression model, with protein amino acid composition as the sole predictor variable. Our analysis revealed significant correlations between negative decoupling and the content of lysine, proline, glutamine, and arginine (Figure 2F). These findings reveal that basic amino acid content has a significant aggregated impact on "negative" decoupling with aging, i.e. the loss of protein levels relative to mRNA.

Since higher content of basic amino acids is a known feature of nucleic acid binding proteins. Therefore, we investigated the age-dependent behavior of proteins involved in DNA repair and experimentally defined RNA-binding proteins (Caudron-Herger et al. 2021). Both these groups of proteins showed an age-dependent decrease of protein- but not transcript-levels (Figure 2G and H). On the other hand, myelin components, e.g., myelin basic protein (MBP) and myelin protein P0 (MPZ), and intermediate filament proteins, e.g. glial fibrillary acidic protein (GFAP) and alpha-internexin (INA), showed decreased transcript- but not protein-levels with aging (Figure 2I), likely due to their long half-lifes and low turnover rates.

Together, our data identify specific classes of proteins that experience "decoupling" between protein and transcript levels in the aging vertebrate brain. We identify distinct biophysical and biochemical characteristics linked to different patterns of dysregulation between protein and transcript levels. This suggests the presence of shared molecular attributes that contribute to aging-linked decoupling phenomena.

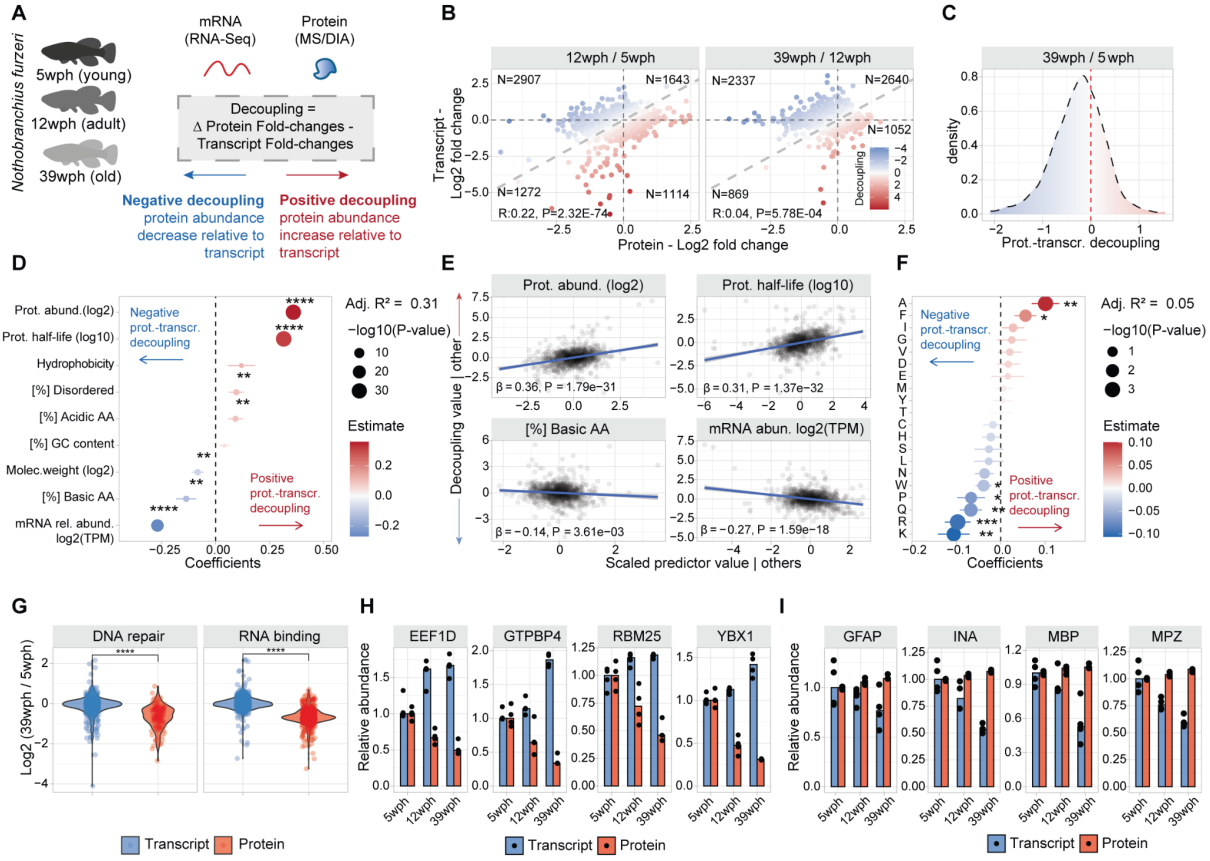

Figure 2: Protein-transcript decoupling affects highly abundant and basic proteins in opposite manners. A) Workflow describing the characterization of protein-transcript decoupling in the killifish aging brain. Age-related changes in transcriptome and proteome are compared to compute the decoupling metrics. For a specific protein, positive decoupling values indicate a relative increase in protein abundance compared to its transcript, while negative decoupling indicates a relative decrease in protein abundance compared to its transcript. B) Scatterplot comparing protein- (x-axis) and transcript-level (y-axis) fold changes in killifish aging brain. The color of each dot represents the decoupling score calculated as the difference between log2 transformed fold changes measured at the protein and transcript levels. Grey dashed lines indicate the equal changes between transcript and protein and, therefore, a zero decoupling score. C) Density distribution of decoupling scores for the comparison of 39 wph vs. 5 wph. On the right part, highlighted in red are positive decoupling events (increase in protein abundance compared to the transcript), while on the left in blue are negative decoupling events (decrease in protein abundance compared to the transcript). Significant changes are defined as Q-value < 0.1. D) Multiple linear regression analysis of decoupling scores based on biophysical features of transcripts or proteins as predictors. The x-axis indicates the estimate of the regression coefficient for each feature, while the size of the dots and asterisks represent the -log10 P-values of the F-test. E) Added variable plot between selected biophysical features and decoupling scores. F) Multiple linear regression analysis of decoupling scores based on percentage of protein amino acid composition as predictors. The x-axis indicates the estimate of the regression coefficient for each feature, while the size of the dots and asterisks represent the -log10 P-values of the F-test. G) Transcript and protein level fold changes for RNA binding and DNA repair proteins for the comparison of 39 wph vs. 5 wph. H and I) Selected examples of proteins showing negative (H) and positive (I) decoupling in the aging killifish brain, N=3-4. *P ≤ 0.05; **P ≤ 0.01, ***P ≤ 0.001, ****P ≤ 0.0001. Related to Figure S5 and Table S4.

Decoupling correlates with changes in detergent-insolubility and affects ribosomes and respiratory chain complexes

To explore the interconnections among the various dimensions of proteome changes in the aging brain, we conducted a gene set enrichment analysis for each layer of the proteome alterations. We then used principal component analysis (PCA) to summarize the normalized enrichment scores (NES) and K-means clustering to identify Gene Ontology (GO) terms that showed correlated changes (Figure 3A, Figure S6A, see methods). By calculating Pearson's correlation coefficient between enrichment scores across datasets, we could define relationships between different layers of aging-linked changes. We found a positive correlation between protein-transcript decoupling and increased detergent insolubility, a hallmark of protein aggregation (Pearson's R = 0.28, P < 2.20E-16), as well as protein phosphorylation (Pearson's R = 0.26, P = 6.67E-08), while other alterations, for instance, changes in protein ubiquitylation, showed a smaller correlation value (Pearson's R = 0.11, P = 1.23E-02, Figure 3B).

To unbiasedly identify the most prominently affected cellular components in our analysis, we ranked GO terms by calculating the values of their projections on the first two principal component axes. We found that the highest-ranking terms were related to components of the mitochondrial respiratory chain and ribosomes (Figure 3C). These two sets of protein complexes were often affected by aging in opposite ways (Figure 3C). Components of the respiratory chain showed a progressive decrease in their transcripts together with a stable or modest increase of the corresponding protein levels (Figure 3D-E, Figure S6B). Respiratory chain proteins also showed an overall increase in detergent insolubility with aging (Figure 3F-G). Importantly, these alterations primarily affected respiratory chain components but not mitochondrial proteins in general (Figure S6C). To corroborate these findings, we interrogated our subcellular fractionation data (Figure S1). This analysis allowed us to identify two key aspects: (i) changes in the protein composition of aged mitochondria, notably a significant decrease in the relative abundance of mitochondrial ribosomes and an increase in the relative abundance of oxidative phosphorylation (Figure 3H and Figure S6D), and (ii) altered subcellular distribution of specific mitochondrial proteins (Figure S6E-F). These analyses provide support for a global remodeling of the mitochondria during aging.

Both cytosolic and mitochondrial ribosomal protein levels progressively decreased during aging (reaching, on average, a ~25% reduction in old brains), while their corresponding transcripts increased (Figure 3I-J, Figure S6G-H). The reduced level of ribosomal proteins was accompanied by a decreased detergent insolubility (Figure 3K-L, S6H-I). This alteration might be related to the loss of ribosome stoichiometry and partial mis-/disassembly that we previously described in the old killifish brain (Kelmer Sacramento et al. 2020). Interestingly, we noticed similar patterns for other large complexes rich in basic amino acids, like RNA polymerase II (Figure S6J-K), that might indicate common mechanisms altering the homeostasis of these key complexes. These results show a significant association between protein-transcript decoupling and other protein alterations in the aging brain that affect ribosomes and mitochondrial respiratory chain complexes preferentially and in opposite directions.

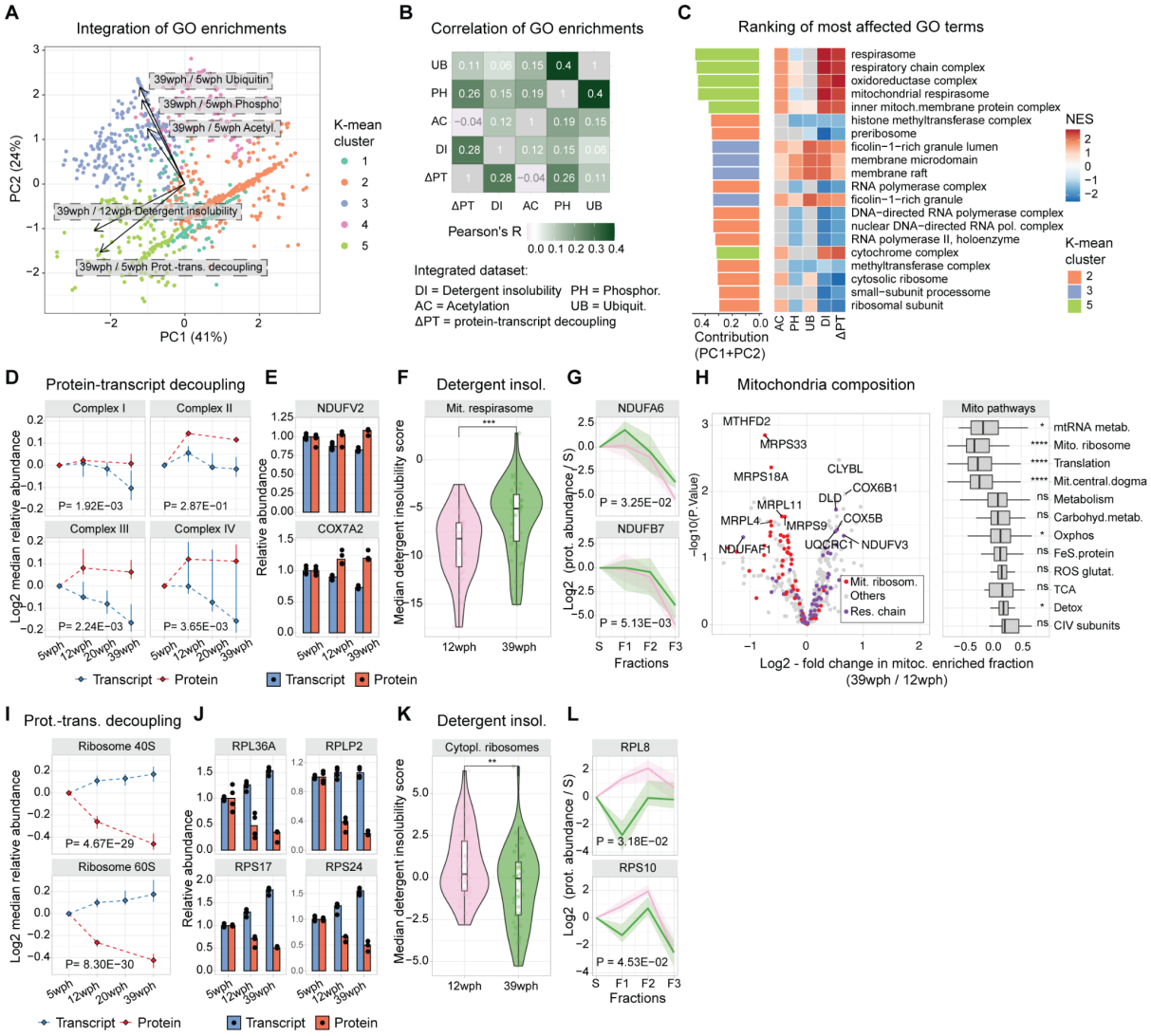

Figure 3: Ribosomes and respiratory chain complexes are major nodes affected in the aging brain. A) Principal component analysis (PCA) showing the relationship between different age-related proteome alterations. PCA was performed on normalized enrichment scores (NES) calculated by gene set enrichment analysis for each dataset. Every dot represents a GO term (cellular component). Arrows show the contribution of each dataset to the first two principal components. Colors indicate different clusters of GO terms obtained by k-means clustering. B) Heatmap showing pairwise correlations of NES values across the different datasets. DR = Detergent insolubility, ΔPT = protein-transcript decoupling induced by aging, AC=Acetylation, PH=Phosphorylation, UB=Ubiquitylation. C) Top-ranking GO terms displaying the strongest contribution to the PCA analysis. GO terms were ranked by summing scores along the first two principal components. The barplot colors indicate the cluster membership of the GO terms, as shown in (A). The heatmap shows the NES values for each of the respective terms across the different datasets. Gray tiles indicate GO terms that were not covered in the given dataset. D) Line plots showing transcript (blue) and protein (red) median abundance for respiratory chain proteins across age groups. Each point summarizes the median log2 protein or transcript quantity for the indicated complex relative to the 5 wph age group (set to 0). The line bars indicate 50% of the distribution across N=3-4 pools per age group. P-values indicate the results of a MANOVA test run on the two multivariate distributions. E) Selected examples of respiratory chain proteins displaying positive protein-transcript decoupling, N=4 pools. F) Violin plot displaying detergent insolubility score for proteins of the mitochondrial respirasome (GO:0070469). Each dot represents the median insolubility score of each protein across N=4 pools per age group; asterisks indicate the results of a two-sample Wilcoxon test G) Examples of detergent insolubility profiles for respiratory chain proteins displaying increased detergent insolubility with aging. The x-axis indicates the different detergent insolubility fractions: S=soluble, F1:F3=fractions after solubilization with buffers of increasing detergent strength (see methods, Figure

S2A). The y-axis indicates log2 protein quantities relative to the soluble (S) fraction. The shaded area indicates 50% of the distribution across N=4 pools per age group. H) On the left, the volcano plot displays changes in mitochondrial proteome composition in response to aging. The x-axis indicates the log2 mitochondrial proteome fold changes, and the y-axis indicates the -log10 P-value of the moderated Bayes T-test. On the right, a box plot showing the effect of aging on different groups of mitochondrial pathways (annotation from MitoCarta 3.0). Each group was tested against the rest of the mitochondrial proteins using a two-sample Wilcoxon test, corrected for multiple testing using FDR correction. Only groups with Adjusted P-value<0.1 are shown. I) Line plots showing transcript (blue) and protein (red) median abundance for ribosomal proteins across age groups. Each point summarizes the median log2 protein or transcript quantity for the indicated complex relative to the 5 wph age group (set to 0). The line bars indicate 50% of the distribution across N=3-4 pools per age group. J) Selected examples of ribosomal proteins showing negative protein-transcript decoupling, N=3-4. K) Violin plot displaying detergent insolubility score for cytoplasmic ribosomal subunits. Each dot represents the median insolubility score of each protein across N=4 pools per age group. L) Examples of detergent insolubility profiles for ribosomal proteins displaying decreased detergent insolubility with aging. The x-axis indicates the different detergent insolubility fractions: S=soluble, F1:F3=fractions after solubilization with buffers of increasing detergent strength (see methods, Figure S2A). The y-axis indicates log2 protein quantities relative to the soluble (S) fraction. The shaded area indicates 50% of the distribution across N=4 pools per age group. *P ≤ 0.05; **P ≤ 0.01, ***P ≤ 0.001, ****P ≤ 0.0001. Related to Figure S6.

Proteasome impairment recapitulates organelle-specific aging hallmarks, but not protein-transcript decoupling

Protein degradation by the ubiquitin-proteasome system has a major role in regulating protein levels and contributes to the maintenance of key organelles and protein complexes, including ribosomes and mitochondria. Previous studies (Kelmer Sacramento et al. 2020; Hipp, Kasturi, and Hartl 2019; Gray, Tsirigotis, and Woulfe 2003) have shown a connection between brain aging and a decline in proteasome activity. Consequently, we investigated the effects of a mild but extended experimentally-induced reduction of proteasome activity on brain aging phenotypes. To this end, we simulated the impairment observed during aging by imposing a chronic reduction of proteasome activity in adult killifish. We optimized *in vivo* dosage of bortezomib, a dipeptide that binds with high affinity and blocks the catalytic site of the proteasome, to maintain a ~50% inhibition in the brain of adult killifish over 4 weeks without inducing overt toxicity and affecting animal well-being (Figure 4A, Table S5). GO enrichment analysis of brain proteome and transcriptome changes showed induction of adaptive responses to bortezomib characterized by over-representation of terms related to the proteasome (Figure 4A) and specific alterations of the proteostasis network (Figure S7A). These include increased protein levels of proteasome activators (PSME1/PA28α, PSME3/PA28γ, and PSME4/PA200) and increased mRNA levels of key autophagy genes such as *ATG5* and *ATG7* (Figure 4B). Some of these adaptive responses, e.g., increased levels of the small heat shock protein HSPB1 (also known as HSP27) and HSPA6, a member of the HSP70 family, were also detected in the brain of old killifish (Figure 4B). Immunofluorescence analysis of lysosomes revealed a marked increase in their area, volume, and sphericity both upon proteasome impairment (Figure 4C) that replicates morphological changes observed during aging (Figure S7B). Lysosomal swelling is also a typical characteristic of lysosomal storage disorders (de Araujo et al. 2020) and increased lysosomal size has also been linked to TDP-43 related Fronto-Temporal Dementia (FTD-TDP43) (Stagi et al. 2014). We also noted that proteasome impairment induced a global decrease in the level of mitochondrial proteins, which was entirely due to post-transcriptional mechanisms (Figure 4D). Consistently, we did not detect changes in master regulators of mitochondrial genes

(Figure S7C). We validated the decreased mitochondrial content by quantifying the ratio of mitochondrial DNA (mtDNA) to nuclear DNA and showed that similar to aging, proteasome impairment also induced a significant reduction of mtDNA (Figure 4D-S7D).

Next, we asked whether proteasome impairment could also recapitulate the age-related protein-transcript decoupling that we characterized. As expected, proteasome impairment led to increased abundance of shorter-lived proteins, consistent with the role of the ubiquitin-proteasome system in regulating their turnover (Figure S7E). Combined analysis of RNAseq and proteome data showed that proteasome impairment indeed induced protein-transcript decoupling (Figure S7F, Table S5). However, when we applied the same multiple linear regression models used for aging, we found that the biophysical properties associated with decoupling by bortezomib are distinct from those associated with decoupling during aging (Figure S7F). Consistently, the decoupling values caused by proteasome impairment or aging were negatively correlated (Spearman Rho = -0.25, P < 2.20E-16, Figure 4E), also for the specific cases of ribosomes (Figure 4F) and respiratory chain complexes (Figure 4G). Together, our findings reveal that partial and chronic inhibition of the proteasome elicits specific adaptive responses in adult killifish, some of which are also observed in aged brains. However, proteasome impairment alone is not able to fully recapitulate age-linked proteome changes, most prominently the age-related protein-transcript decoupling.

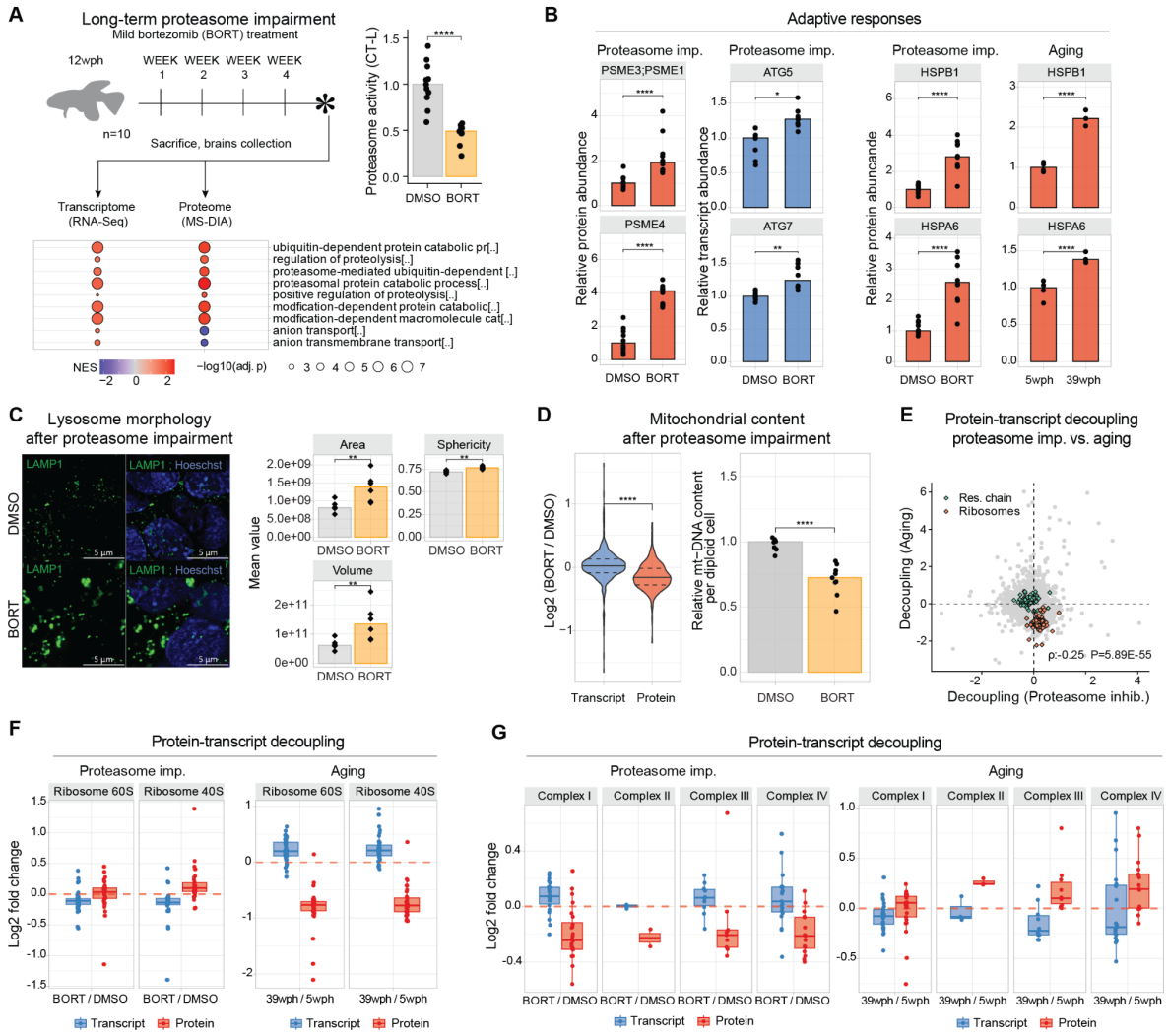

Figure 4: Effects of four weeks *in vivo* proteasome impairment on the killifish brain. A) Adult killifish (12 wph, N=10) were treated for 1 month, every week, with an intraperitoneal injection of the proteasome inhibitor bortezomib or vehicle control (DMSO). The bottom panel shows a Gene Set Enrichment Analysis (GSEA) of the proteasome impairment sample (BORT/DMSO). Color code indicates the normalized enrichment score (NES) while dot size indicates the -log10 of the adjusted P-value of the Kolmogorov-Smirnov tests (Holm's correction). The top-right panel shows quantification of chymotrypsin-like (CT-L) proteasome activity in brain lysates following repeated injections of bortezomib or DMSO control. Asterisks indicate the results of a two-sample Wilcoxon test, N=10. B) (Left panel) Barplot showing normalized protein quantity (relative to DMSO control, set to 1) of selected proteins (red) and transcript (blue) involved in the proteostasis network and their correspective in aging (Right panel). Asterisks indicate the Q-value of the differential abundance testing performed with a two-sample T-test on the peptide abundances N=10. C) (Left panel) Immunofluorescence stainings for lysosome (LAMP1) in brain cryo-sections of control and treated *Nothobranchius furzeri*. Scale bars = 5µm. (Right panel) Barplot representation of lysosome morphology features in control (grey) and Bortezomib treated (orange) samples. The y-axis represents the mean value of the different morphology features in each replicates (N=6). D) (Left panel) Effect of proteasome impairment on mitochondrial transcripts and proteins. Asterisks indicate the results of a two-sample Wilcoxon test. (Right panel) Quantification of mitochondrial DNA (mt-DNA) from killifish brains. Relative mtDNA copy number was calculated using real-time quantitative PCR with primers for 16S rRNA mitochondrial gene and Cdkn2a/b nuclear gene for normalization (N=10). Asterisks indicate the results of two-sample Wilcoxon tests. E) Comparison of decoupling scores measured in aging (old vs. young comparison, y-axis) and upon partial proteasome impairment (bortezomib vs. DMSO, x-axis), proteins related to the respiratory chain (green) and ribosomal proteins (orange) are shown. Spearman correlation was selected due to the presence of outliers in the distribution. F) Comparison of decoupling induced by aging and proteasome impairment for ribosomes. G) Comparison of decoupling induced

by aging and proteasome impairment for oxidative phosphorylation proteins. *P ≤ 0.05; **P ≤ 0.01, ***P ≤ 0.001, ****P ≤ 0.0001. Related to Figure S7, Table S5.

Translation pausing correlates with decreased levels of basic proteins in old brains

Our results suggest that factors other than proteasome dysfunction contribute to the dysregulation of protein homeostasis during aging. One potential alternative mechanism is the differential translation of specific mRNAs at old age, which could contribute to the age-related discrepancy between transcript and protein levels. Therefore, we assessed changes in translation output, estimated from transcript occupancy by ribosomes, via a Ribo-Seq experiment in the killifish aging brain (Figure 5A, Table S6). Quality assessment of the reads showed the characteristic tri-nucleotide periodicity (Figure S8A) and overall reproducibility across replicates (Figure S8B). We compared age-related changes in ribosome occupancy and mRNA levels and observed the expected positive correlation (R=0.25, *P* < 2.20E-16, Figure S8C). We then estimated changes in translation efficiency (TE) from RNA-Seq and Ribo-Seq (see methods) and compared them to proteome data. In line with previous findings in the rat brain (Ori et al. 2015), we observed a stronger positive correlation between the changes of TE and protein abundance (R=0.32, *P* < 2.20E-16, Figure 5B) than between changes of transcript and protein abundance (R=0.23, *P* < 2.20E-16). Changes in TE led to consistent alterations in protein levels for specific proteins, such as members of the Complex IV of the respiratory chain, where increased TE was associated with higher steady-state protein levels (Figure 5C and S8D). Intriguingly, this was not the case for other protein complexes, including ribosomes, RNA polymerase II and other nucleic-acid binding proteins involved in DNA repair, where increased TE was associated with a paradoxical reduction of steady-state protein levels (Figure 5C, 5D, and S8D). These two modalities of protein regulation act independently of transcript regulation. In summary, we found that for some proteins, changes in TE with aging can amplify transcriptional changes, e.g., for proteasomes (Figure 5D), or compensate for transcript regulation, e.g., for respiratory chain complexes (Figure 5D and S8D). However, for some proteins, TE alone cannot explain the divergence between proteome and transcriptome, as in the case of ribosomal proteins (Figure 5D).

Recent studies showed that aging is associated with translation dysfunction in yeast and nematodes, whereby enhanced elongation pausing leads to ribosome collisions, abortive translation of stalled mRNAs and aggregation of their encoded nascent polypeptides(Stein et al. 2022). To assess if a similar effect of aging on translation could explain the apparent incongruence between mRNA and protein levels observed in aged killifish brains, we queried our Ribo-Seq data for signatures of translation pausing (i.e., analysis of pairs of highly occupied codons, see Experimental Procedures). Indeed, this analysis revealed an overall increase in site-specific pausing in the aging brain (Figure 5E, Table S6). Additionally, disome analysis provided evidence for increased ribosome collisions in the old brain (Figure 5F). Ribosome collision and stalling have been associated with changes in the ubiquitylation of ribosomal proteins (Meyer et al. 2020; Higgins et al. 2015; Yan et al. 2019). To assess the detection of these changes in the killifish system, we induced ribosome stalling in killifish cells using anisomycin and validated the appearance of a higher molecular weight band in immunoblot against the 40S subunit RPS3 (Figure S8E). A similar higher molecular weight band was detectable in aging killifish brains, and its ratio to total RPS3 increased with age

(Figure S8F). This enhanced ubiquitination was in contrast with multiple other sites of ribosomal protein ubiquitylation detected by mass spectrometry as these were, for most ribosomal proteins, reduced with aging (Figure S8G). Together, these data support an increase of ribosome collision in the aging killifish brain. Of note, similar to what is observed in yeast and nematodes, aging also causes a progressive decrease of a subset of proteins involved in ribosome quality control (RQC) in aged killifish brains (Figure S8H). Such impairment of RQC may exacerbate ribosome collision and stall with age and may also disrupt the degradation of stalled mRNAs, leading to their accumulation in the aged cells.

Analysis of the correlation between our measured proteomic features and translation alterations with age identified a positive correlation between translation pausing and increased detergent insolubility, which is considered a hallmark of aggregation (Figure 5G). These alterations affected key proteostasis network components such as the proteasome (Figure S8I). Remarkably, stretches enriched in basic residues (arginine and lysine), as well as glycine, were enriched at both pausing (Figure 5H) and disome sites (Figure S8J). These features are consistent with previous observations from yeast and nematodes (Stein et al. 2022) and suggest a link between pausing, protein aggregation and proteostasis collapse in the aging vertebrate brain. Interestingly, the same residues (arginine and lysine) were associated with decreased protein levels in our decoupling model (Figure 2F). Consistently, we detected a significant correlation between translation pausing and protein-transcript decoupling (Figure 5I, R=-0.17, P < 2.20E-16). This indicates that translation pausing can explain a substantial fraction of the cases where reduced protein abundance is uncoupled from transcript regulation. More specifically, we observed increased pausing on transcripts coding for ribosomal and RNA-binding proteins, which exhibit a depletion at the protein level not reflected in their transcripts. At the same time, components of the respiratory chain did not show any remarkable deviation from the overall pausing distribution (Figure 5I), although different complexes showed distinct pausing profiles (Figure S8K). Alterations in translation efficiency and pausing have been linked to changes in mRNA half-life (Sharma et al. 2021; Chan et al. 2018; Schwartz and Parker 2000). Therefore, we estimated age-related alterations in mRNA half-life by calculating changes between exonic and intronic reads (Gaidatzis et al. 2016). Interestingly, we observed that in old brains transcripts encoding for ribosomal proteins and RNA-binding proteins showed increased half-life compared to the rest of the transcriptome (Figure 5J), suggesting that the increase in transcript levels might not be the result of increased transcription of these genes. Together these results show that increased ribosome occupancy does not necessarily result in enhanced protein synthesis in the aging brain, possibly due to increased pausing at some mRNAs. Furthermore, translation pausing is associated with signatures of ribosome collisions, which correlate with changes in protein solubility. We thus propose that translation dysfunction may represent the underlying cause for the decreased levels of ribosomal proteins and other nucleic-acid binding proteins in the aging brain. Taken together, our data suggest a link between translation pausing, protein aggregation and proteome alterations affecting proteostasis in the aging vertebrate brain.

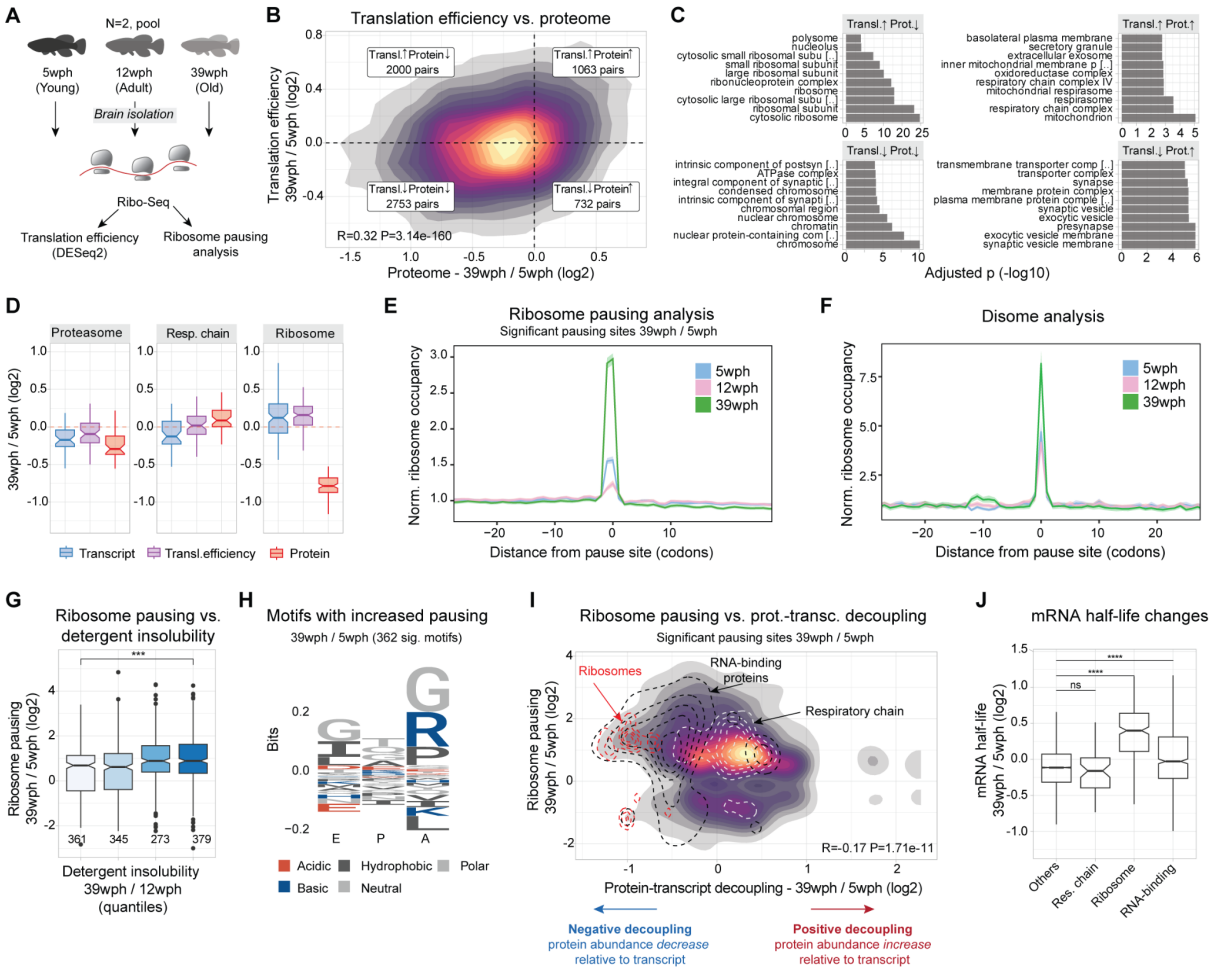

Figure 5: Increased translation pausing in the aging killifish brain. A) Workflow of the experiment. Ribosome profiling was performed on Young (5 wph), Adult (12 wph), and Old (39 wph) *Nothobranchius furzeri* brains. Each (N=2) replicate consisted of a pool of 10-15 animals depending on the age group. B) 2-D density plot showing the relationship between age-related changes in protein abundance (x-axis) and changes in translation efficiency (y-axis). In each quadrant are summarized the number of protein and transcript pairs. C) GOEnrichmet analysis (ORA) on each quadrant shown in B. The x-axis indicates the -log10(adjusted P-value) of the Fisher test with Holm correction. D) Boxplot displaying differential modes of regulation, for example, protein complexes. On the x-axis are displayed the different datasets: Transcriptome (green), Translation efficiency (purple), and Proteome (red) for 26S Proteasome, oxidative phosphorylation, and cytoplasmic ribosomes. E) Lineplot showing the normalized ribosome distribution at different pausing sites for different age groups. The x-axis represents the distance (in codons) from the pausing site, while on the y-axis the normalized ribosome occupancy is shown. F) Lineplot showing the normalized disome ribosome distribution at different disome pausing sites for different age groups. The x-axis represents the distance (in codons) from the disome pausing site, while on the y-axis the normalized ribosome occupancy is shown. G) Boxplot showing the relationship between solubility and ribosome pausing. On the x-axis, the solubility values are grouped according to quantiles. Each quantile holds for 25% of the protein distribution. On the y-axis, the log2 fold changes in pausing for each significant (Adjusted P-value < 0.05) pausing site. Numbers in black indicate the number of observations in each of the distributions. H) Weblogo for residues that display a strong increase in pausing (Pause score > 10) in 39 wph/5 wph. The y-axis displays the relative frequencies of the different residues, while the x-axis displays the different ribosome positions (E, P, A). I) 2-D density plot showing the relation between significant changes in pausing (Adjusted P-value < 0.05) displayed on the y-axis and the decoupling metrics (x-axis). Each point in the distribution represents a significantly altered pausing site. Contour lines indicate the distribution of cytoplasmic ribosomes (red), RNA-binding proteins (black), and oxidative phosphorylation (white). J) Boxplot showing mRNA half-life estimate changes (see methods) between 39 wph and 5 wph. The x-axis represents different selected categories. Asterisk indicates the results of a two-sample Wilcoxon test with Holm correction. *P ≤ 0.05; **P ≤ 0.01, ***P ≤ 0.001, ****P ≤ 0.0001. Related to Figure S8, Table S6.

Proposing a possible model for a reshaping of translation in the aging brain

The results presented so far point to alterations in protein synthesis in old brains leading to a reduction of ribosomal proteins, among others. We hypothesized that the ensuing lower levels of ribosomes, particularly in light of increased load on the RQC machineries, may in turn lead to a vicious cycle of dysfunction. Altered ribosome concentration has been known to directly impact the translation of specific mRNAs, as observed in a group of inherited diseases collectively referred to as 'ribosomopathies' (Mills and Green 2017; Khajuria et al. 2018). We thus attempted to extend a model proposed by (Mills and Green 2017; Khajuria et al. 2018) to the aging scenario. The original model predicts that the protein output of specific mRNAs can be influenced by ribosome availability depending on transcript-specific translation initiation rate k_i (where k_i refers to the affinity of specific mRNAs sequences to bind ribosomes) (Mills and Green 2017; Khajuria et al. 2018). Under these assumptions, a decrease in ribosome concentration can, for example, increase protein synthesis from transcripts that have a high translation initiation rate by lowering the total ribosome load on them and therefore relieving trafficking and pausing events (Figure 6A). To test this hypothesis in the context of aging brain, we estimated k_i from killifish 5'-UTR sequences based on experimental data (Noderer et al. 2014), and modeled the estimated synthesis rate as described in (Mills and Green 2017; Khajuria et al. 2018) (see methods, Figure 6A, Table S7). In agreement with the model, a subset of killifish transcripts displayed an increase in predicted synthesis rate as a function of decreased ribosome concentration (orange cluster in Figure 6A and Table S7). To test these predictions on our experimental data, we selected a specific set of proteins showing decreased translation pausing and increased protein abundance in our decoupling model (60 proteins, bottom right quadrant in Figure 5I). We then estimated their predicted synthesis rates as a function of ribosome concentration. Consistent with the experimental data, the relative synthesis of this subset of proteins was predicted to increase following a reduction of ribosome concentration (Figure 6B). Approximately one-third of these proteins were mitochondrial (including 7 components of the respiratory chain), and another prominent fraction belonged to proteins related to neuron projections (Figure 6B). Intriguingly, the absence of ribosomal proteins in this subset, despite their high k_i value, indicates distinct translation dynamics for these proteins resulting from their increased elongation pausing during aging. These results provide evidence that reduced ribosome concentration in aged brains, likely triggered by aberrant pausing events, might remodel a subset of the proteome independently of transcript levels and regulation (Figure 6C).

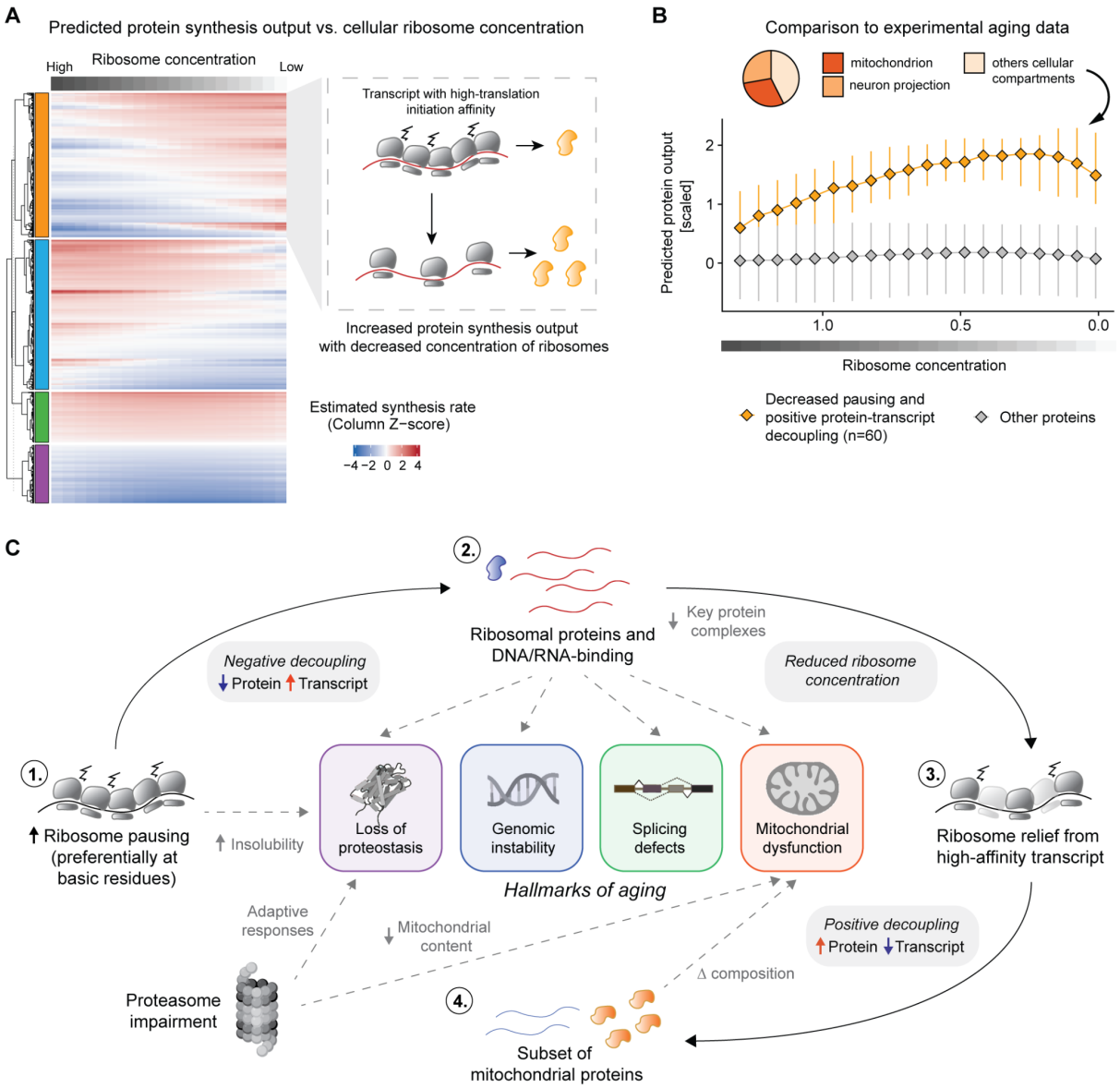

Figure 6: **Reduced ribosome levels can lead to translation reprogramming in the aging brain.** A) Heatmap showing the estimated protein output, modeled as described in Mills and Green 2017. Each column in the heatmap indicates the estimated protein output for a specific ribosome concentration. Transcripts are clustered with a hierarchical clustering using the "ward D2" algorithm on the dissimilarity (1 - Person's correlation) measure. For display purposes, the heatmap represents 5000 rows randomly sampled from all datasets. In the right panel, an illustrative example of a cluster displaying increased estimated protein output as a function of reduced ribosome levels. For these transcripts, the general ribosome decrease is predicted to relieve trafficking and pausing, leading to overall improved protein production. B) Lineplot showing the estimated protein output for transcript displaying decreased ribosome pausing in the Ribo-Seq data (median per transcript log2 Pausing 39 wph / 5 wph < 0 and Adjusted P-value <=0.15) and increased protein levels relative to the transcript in the decoupling model (orange). The x-axis represents the simulated decreased ribosomal concentration, while the y-axis indicates the estimated protein output, as shown also in A. C) Schematic representation of the translation reprogramming model and its connection with the relevant hallmarks of aging. Aging is associated with increased ribosome collision and pausing on ribosomal proteins, leading to a ~25% reduction of ribosome levels. This generalized decrease of available ribosomes could drive the translation of other high-affinity mRNAs leading to increased protein levels in the aging brain. Related to Table S7.

Discussion

Our work provides an integrated view of the changes in the diverse mechanisms comprising proteostasis and illuminates how they contribute to the remodeling of the vertebrate brain proteome during aging. We demonstrate that aging brains exhibit profound alterations in their proteome, manifested as changes in protein synthesis, solubility, post-translational modification and, organelle composition compared to younger ones. We also observe significant changes in the composition of their proteome, such as an overall reduction in ribosome levels, that do not correspond to changes in mRNA abundance. Our analysis further suggests that such proteome changes are driven in significant measure by alterations in translation, including increased elongation pausing at specific polybasic stretches. A corollary of these changes is that aging protein synthesis may no longer respond faithfully to changes in transcriptional programs. Accordingly, we observe that increased ribosome occupancy does not necessarily translate to higher protein synthesis in aged brains. Furthermore, we identify limitations in adaptive responses, such as the ones to proteasome impairment, which are only partially mounted in old brains. By unraveling these age-dependent events and understanding their underlying logic, we begin to establish connections between proteostasis alterations and other hallmarks of aging. These include mitochondrial and lysosomal dysfunction as well as aberrant RNA synthesis, splicing and, genome stability, given that translation of proteins involved in these processes is affected by age (Figure 6C).

Based on our observations, we propose that there are at least three different modalities in which protein production can be affected in the aging brain: (i) transcriptional modulation, i.e., changes in protein production that are influenced by the level of mRNA. For example, in the case of proteasomes, where decrease in protein abundance with age is associated with lower levels of mRNAs (Figure 5D). (ii) Translational modulation, i.e., changes in protein production that occur at the level of translation efficiency. This is exemplified by some components of the respiratory chain, particularly Complex IV, that show increased protein levels in old brains. In this case, reduced levels of mRNA are compensated by higher ribosome occupancy and more efficient protein synthesis (Figure S8D). (iii) Translational pausing, i.e., a specific type of modulation where prevalently proteins rich in basic amino acids, such as ribosomal and other nucleic acid binding proteins, experience increased translation stalling. This correlates with higher levels of mRNA but subsequently leads to unproductive protein synthesis.

The aging-linked changes in protein biosynthesis that we describe have two direct implications. First, the availability of a subset of protein complexes, notably those containing regions enriched in basic amino acids, is reduced in the aging brain. These complexes include those involved in all the major steps of protein biosynthesis, including ribosomes themselves but also other RNA-binding proteins involved in splicing, as well as RNA and DNA polymerases and DNA repair proteins. Interestingly, previous studies have proposed a translation control mechanism for this class of proteins influenced by the presence of lysine and basic amino acids (Arthur et al. 2015). All biological functions linked to these protein complexes have been shown to decline or become perturbed with age, and indeed their dysfunction is recognized as “hallmarks of aging”. Perhaps, the common biophysical properties of the components of these protein complexes make them vulnerable to translation dysfunction with aging. Consequently, the observed impairment of protein biosynthesis with aging may contribute to other aging hallmarks that generally depend on nucleic acid binding proteins (López-Otín et al. 2023). The interplay of these processes in all the major steps of

protein synthesis may amplify these dysfunctions in a vicious feedback loop that further impairs proteostasis. Of note, individual manipulation of any of these pathways has been shown to ameliorate aging phenotypes (Schumacher et al. 2021; Bhadra et al. 2020; Bozukova et al. 2022; Gyenis et al. 2023; Debès et al. 2023; Gonskikh and Polacek 2017).

The second implication is that aging leads to a change in the protein composition of organelles, in particular mitochondria. Remodeling of protein biosynthesis leads to a reduction of mitochondrial ribosomes, similarly to other basic proteins, while components of the respiratory chain are maintained or even increased, as in the case of Complex IV. These observations based on bulk tissue measurements were corroborated by more direct analysis of the composition of mitochondria from subcellular fractions and by other age-dependent alterations of mitochondrial proteins, e.g., in detergent insolubility and sedimentation profiles. A compositional change of the brain mitochondrial proteome with age aligns with previous observations from other species (Ingram and Chakrabarti 2016), and with ultrastructural and functional alterations reported in aging and age-associated diseases (Heiby and Ori 2022). We also found that other aspects of mitochondria aging in the brain, i.e., reduced mtDNA content, were instead dependent on decreased proteasome activity, highlighting the convergence of multiple aging mechanisms in determining the levels and composition of key cellular structures such as mitochondria (Figure 6C).

Our data demonstrate that increased translation pausing during aging is an evolutionarily conserved phenomenon (Stein et al. 2022). Future analyses should clarify the mechanistic and/or regulatory events leading to increased translation pausing with age and their relationship with other age-related alterations of ribosomes, including loss of stoichiometry and aggregation (Kelmer Sacramento et al. 2020). One of the mechanisms potentially contributing to increased translational pausing could reside in the decrease in ATP levels that is typically observed in old tissues (Miyoshi et al. 2006; Braeckman, Houthoofd, and Vanfleteren 2002; Gkotsi et al. 2014; Espada et al. 2020). This reduction in energy levels might alter the decoding kinetics for specific non-optimal codons, such as the ones encoding basic amino acids (Bazzini et al. 2016; da Silva et al. 2023), leading to a decreased synthesis rate for these proteins. We also identified distinctive changes in protein ubiquitylation in ribosomal proteins, some of which have been previously associated with ribosome collision induced by different types of translation or proteotoxic stress (Higgins et al. 2015; Yan et al. 2019). However, it remains unclear whether these modifications are a cause or consequence of increased pausing. For ribosomes, decoupling in aging manifests as a decrease in protein levels together with a progressive increase in transcript levels. These findings are consistent with several observations. First, an age-dependent increase of transcripts encoding for ribosomal proteins has been observed by single-cell RNAseq in multiple cell types of the murine brain (Ximerakis et al. 2019). Accordingly, increased levels of transcripts encoding for ribosomal proteins were one of the most consistent transcriptional signatures of longevity shared across multiple tissues and mammalian species (Tyshkovskiy et al. 2023). Interestingly, our results suggest that this increase might not result from increased transcription but rather from increased mRNA stability. Decreased abundance of ribosomal proteins with age has been described in multiple organs in mice (Yu et al. 2020), as well as in nematodes (Koyuncu et al. 2021), and the protein half-life of ribosomes is affected by aging in the mouse brain (Kluever et al. 2022). These data suggest that similar mechanisms might affect ribosomes in different cell types and organs during mammalian aging. Translation pausing may also represent a converging pathophysiological mechanism shared between

aging and neurodegenerative diseases, as ribosome stalling has been linked to perturbation of proteostasis in different types of neurodegenerative diseases (Z. Wu et al. 2019; Rimal et al. 2021; S. Li et al. 2020; Aviner et al. 2022).

Other mechanisms that have not been investigated in this study can additionally contribute to protein-transcript decoupling. For instance, age-dependent impairment of protein degradation by the autophagy-lysosome system can lead to the accumulation of specific proteins (Aman et al. 2021), as has been shown for myelin basic protein (MBP) in microglia (Safaiyan et al. 2016). Interestingly, although induction of initial stress response was congruent in aging and after proteasome impairment, a compensatory activation of autophagy was induced by proteasome impairment in adults but not during aging. This discrepancy explains, at least in part, the anti-correlation that we observed between bortezomib-induced and age-related decoupling and leaves open the interesting question of why aging brains fail to mount a compensatory response to proteasome dysfunction. In this regard, it is noteworthy that aging impairs the ability to respond to heat shock in *C. elegans (Johnathan Labbadia and Morimoto 2015)*. In addition, stalling of RNA polymerase II has been described to occur with aging, thereby skewing the output of transcription in a gene-length dependent manner (Gyenis et al. 2023), consistent with a systemic loss of long transcripts observed in multiple aging tissues and species (Stoeger et al. 2022). A reduction in the abundance of specific transcripts could increase transcriptional noise, lead to an imbalance in the stoichiometry of protein complexes, but also alter the relationship between mRNA and protein levels, especially for long-lived proteins.

Finally, our work might contribute to the understanding of the relationship between aging and the risk of neurodegenerative diseases. We provide an unprecedented resource (accessible at https://genome.leibniz-fli.de/shiny/orilab/notho-brain-atlas/, credentials will be available after final publication) of proteome alterations in the aging vertebrate brain and show that multiple proteins and signaling pathways associated with neurodegeneration in humans become perturbed in different ways during physiological aging in killifish. Such alterations might underlie convergent mechanisms between aging and mutations that increase the risk of neurodegeneration in old individuals.

Limitations of the study: (i) Our analyses are based on measurements performed on bulk brain tissue and, therefore, can be interpreted only as an average effect across different cell types and brain regions. In addition, phenomena occurring in rare cell populations might be missed by our analysis. (ii) Our findings are based on steady-state levels and do not allow us to estimate the impact of aging on the synthesis and degradation of transcript and protein directly. In the future, pulse-chase experiments performed *in vivo* using labeled nucleotides and amino acids could enable a more direct investigation of mRNA and protein turnover dynamics in aging. (iii) Some of our data lack spatial resolution, which could be critical to study highly specialized cells such as neurons and discern proteome differences between, e.g., cell body and synapses. (iv) Although we demonstrate that several aging phenotypes that we describe are conserved across species, we cannot exclude that some effects might be restricted to killifish and, therefore, not transferable to other species.

Acknowledgments

The authors gratefully acknowledge support from the FLI Core Facilities Proteomics, Sequencing, and the Fish Facility as well as the Stanford Genomics Facility. A.O. is supported by the German Research Council (Deutsche Forschungsgemeinschaft, DFG) via the Research Training Group ProMoAge (GRK 2155), the Else Kröner Fresenius Stiftung (award number: 2019_A79), the Fritz-Thyssen Foundation (award number: 10.20.1.022MN), the Chan Zuckerberg Initiative Neurodegeneration Challenge Network (award numbers: 2020-221617, 2021-230967 and 2022-250618), and the NCL Stiftung. J.H.L. was supported by the National Institute on Aging of the National Institutes of Health under Award Number T32 AG000266, and research by NIH grants GM05643319 and AG054407 to J.F. A.C. is supported by the German Research Council (Deutsche Forschungsgemeinschaft, DFG, award numbers CE 257/9-1 and CE 257/9-2), by Next Generation EU (PNRR), "Tuscany Health Ecosystem", THE project code ECS 00000017 and the Italian Ministry of University and Research (MUR) with the program "Joined research for Special Status Schools" PRO3. The content is solely the responsibility of the author(s) and does not necessarily represent the official views of the National Institutes of Health. The FLI is a member of the Leibniz Association and is financially supported by the Federal Government of Germany and the State of Thuringia.

Author contributions

Conceptualization: DDF, AM, JF, AC, AO
Data curation: DDF, AM, JHL, AKS, MT
Investigation: DDF, AM, JHL, EKS, MB, SB
Methodology: DDF, AM, JHL, EKS, MB, SB
Project administration: AO, AC
Data analysis: DDF, AM, JHL, PS, GS
Supervision: ETT, JG, JF, AC, AO
Visualization: DDF, AM, JHL, SB
Writing – original draft: DDF, AM, AO
Writing – review & editing: JHL, EKS, MB, SB, PS, AKS, GS, JF, AC

Declaration of interest

Authors declare no competing interests.

Supplementary information

Figure S1: Subcellular fractionation of the killifish aging brain by LOPIT-DC
Figure S2: Protein detergent insolubility changes in the killifish aging brain
Figure S3: Analysis of protein post-translational modifications in the killifish aging brain
Figure S4: Age-associated alterations of proteins linked to human neurodegenerative disorders
Figure S5: Proteome and transcriptome characterization of the killifish aging brain
Figure S6: Alterations of ribosomal and respiratory chain proteins
Figure S7: Effect of proteasome impairment on the killifish brain
Figure S8: Ribosome profiling in the killifish aging brain

Table S1: Proteome alterations in the aging brain. Data from LOPIT-DC experiment and proteome insolubility characterization
Table S2: Post-translational modification changes in the killifish aging brain
Table S3: Killifish orthologs of proteins associated with neurodegenerative disease in humans
Table S4: Proteome and transcriptome data and protein-transcript decoupling in the aging brain
Table S5: Proteasome impairment in the killifish aging brain. Tables for Proteome, Transcriptome and protein-transcript decoupling induced by the proteasome impairment treatment
Table S6: Ribosome-sequencing experiment in the killifish aging brain. Data for translation efficiency and ribosome pausing analysis
Table S7: Estimate of protein synthesis rate as a function of ribosome concentration decrease

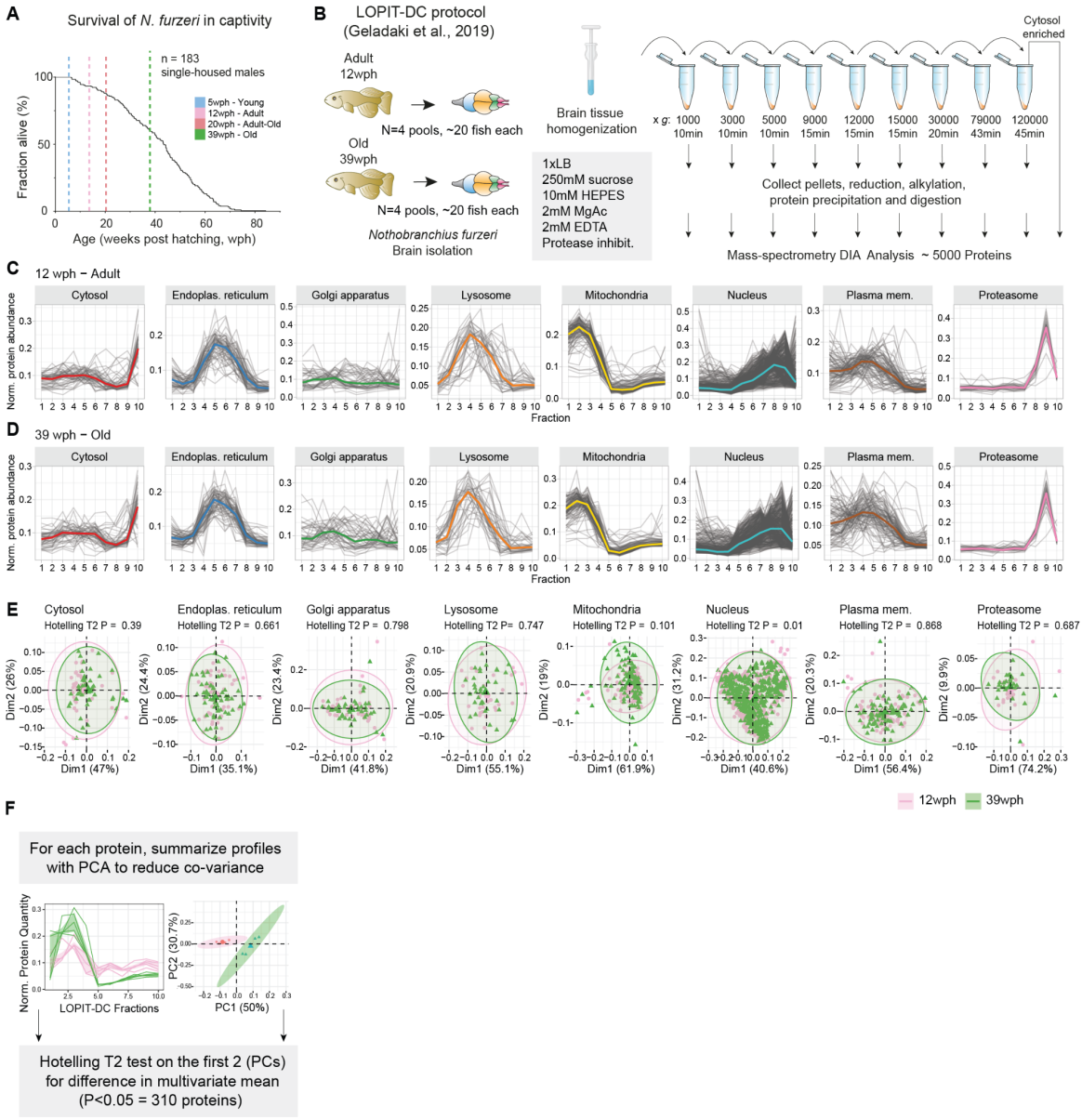

Figure S1: Subcellular fractionation of the killifish aging brain by LOPIT-DC. A) Survival curves of *Nothobranchius furzeri* MZM-0410 strain in captivity (data from (Baumgart et al. 2016)). The survival of *Nothobranchius furzeri* was investigated by tracking the occurrence of deaths starting at the age of 5 weeks post-hatching (wph), which corresponds to sexual maturity. This study includes data from four age groups highlighted by vertical dashed lines. The analyzed strain was derived from the wild with a median lifespan of 7-8 months. B) Scheme of the LOPIT-DC experiment. The protocol was adapted to brain tissue from Geladaki et al. 2019; see methods for details. C-D) Organelle markers protein profiles from LOPIT-DC. The x-axis indicates the different fractions. The y-axis indicates protein abundance estimates derived from label-free Data Independent Acquisition mass spectrometry. Protein quantities were normalized by dividing the protein quantity in each fraction by the sum of the protein quantity along fractions. Each profile represents the median across replicates (N=4 pools). The median profiles of each organelle are highlighted by a colored solid line. Profiles obtained from adult (12 wph, panel C) and old (39 wph, panel D) fish are shown. E) Principal component analysis for different organelles markers in the LOPIT-DC fractions. Organelle markers from 12 wph (pink) and 39 wph (green) are shown. Each dot represents the median profile across (N=4 pools) replicate for each condition. F) Computational strategy used to identify age-related changes in protein sedimentation profiles. Related to Figure 1 and Table S1.

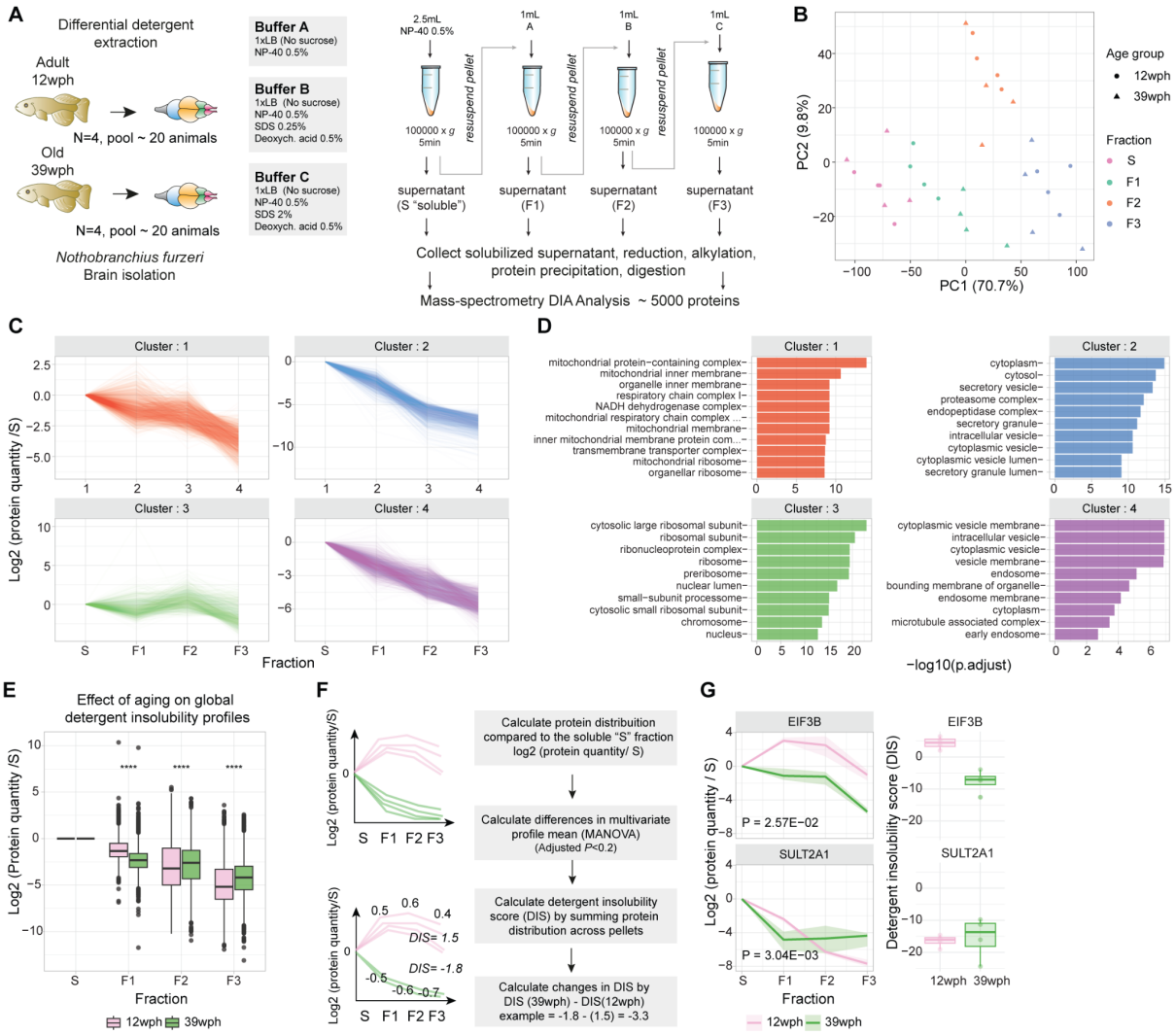

Figure S2: Protein detergent insolubility changes in the killifish aging brain. A) Scheme of the differential detergent extraction experiment. The protocol was adapted to brain tissue from Tebbenkamp and Borchelt, 2009 (see methods). B) Principal component analysis based on proteomics data from fractions obtained by differential detergent extraction. C) K-means clustering of detergent insolubility profiles. On the y-axis, the log2 protein quantity relative to the soluble "S" fraction, each profile represents the median across both conditions and (N=4 pools) replicates. D) GO enrichment overrepresentation analysis (ORA) of proteins assigned to each cluster against the rest of the identified proteome. On the x-axis, the -log10 of the adjusted P-value (Holm correction) of the Fisher's Test is reported. Colors refer to the different clusters displayed in panel C. E) Boxplot depicting detergent insolubility profiles for all the proteins quantified across age groups. The y-axis indicates the log2 transformed value of protein quantity in each fraction relative to the soluble (S) fraction. Asterisks indicate the results of a two-sample Wilcoxon test. F) Computational strategy used for calculating differences in detergent insolubility profile across age groups. A MANOVA test was performed on each protein profile to detect significant changes in the multivariate mean between 12 wph (adult) and 39 wph (old samples), N=4 pools per age group. The detergent insolubility score (DIS) was calculated by summing the log2 protein quantity (relative to the soluble S fraction). Higher DIS indicate proteins that are relatively more abundant in insoluble fractions (F1:F3) than the soluble one (S). G) Example profiles of top hits proteins displaying changes in detergent insolubility with aging. EIF3B is an example of a protein that displays decreased detergent insolubility with age, while SULT2A1 displays increased detergent insolubility with age. For the left panel, the y-axis represents the log2 protein quantity in each fraction relative to the first soluble (S) fraction. Dark lines indicate the median between replicates, while shaded areas represent 50% of the replicate distribution, N=4 pools per age group. On the right panel, boxplots show the Detergent insolubility score (calculated as the sum of the log2 protein quantity relative to the first soluble (S) fraction) for the same proteins. Related to Figure 1 and Table S1. *P ≤ 0.05; **P ≤ 0.01, ***P ≤ 0.001, ****P ≤ 0.0001.

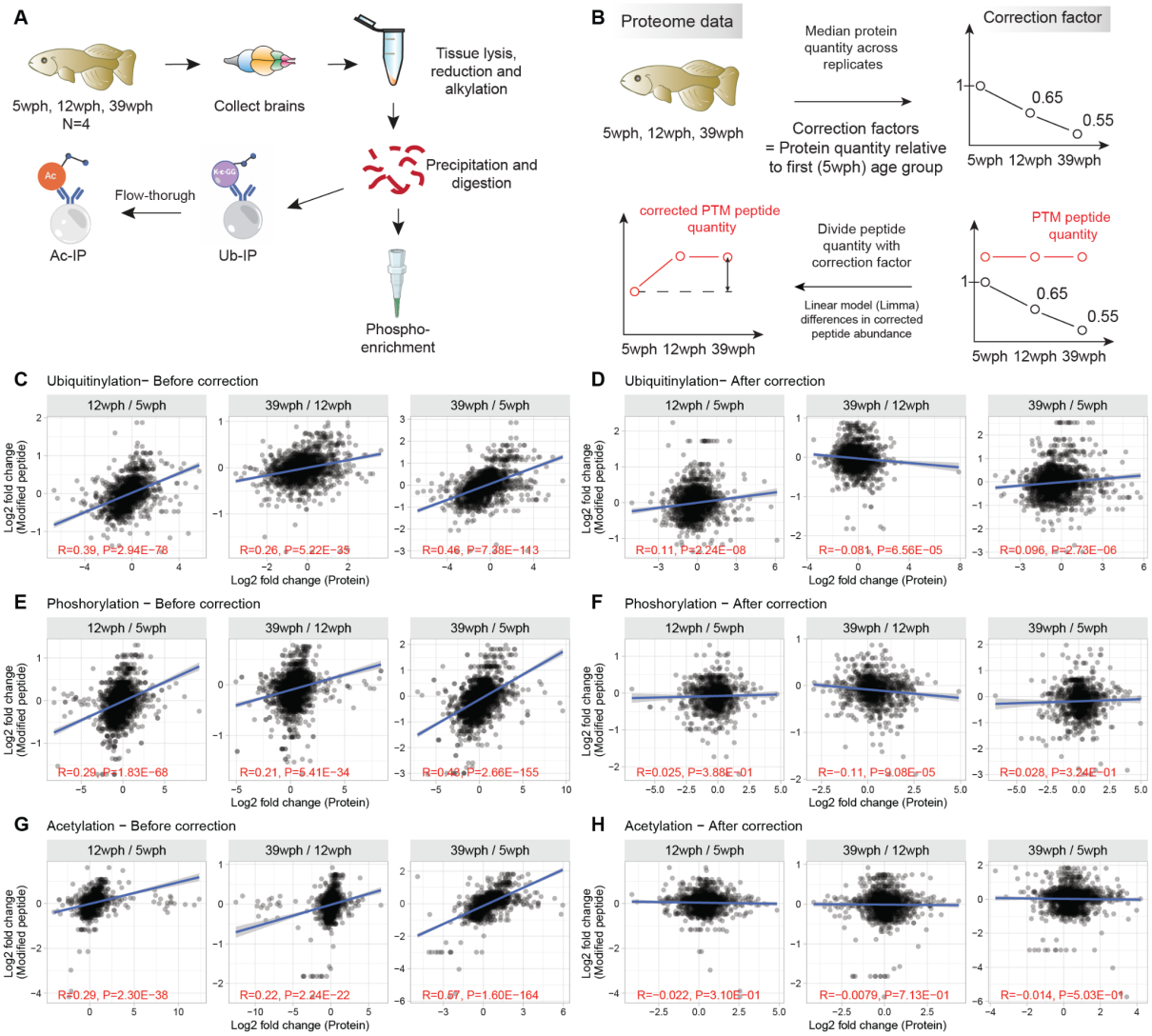

Figure S3: Analysis of protein post-translational modifications in the killifish aging brain. A) Workflow for the enrichment of post-translational modified peptides from in killifish brain. B) Correction strategy for detecting stoichiometric changes in post-translationally modified peptides. Correction factors were computed for each protein and condition relative to the 5 wph (young) age group. Quantities of the modified peptides were divided by the corresponding protein correction factor, and age-related changes were tested using *limma* (Ritchie et al. 2015). C-H) Relationship between age-related abundance changes of modified peptides vs. corresponding protein, before (left panels) and after (right panels) correction. The red text indicates the test results for the association between paired samples using Pearson's product-moment correlation coefficients. Related to Figure 1 and Table S2.

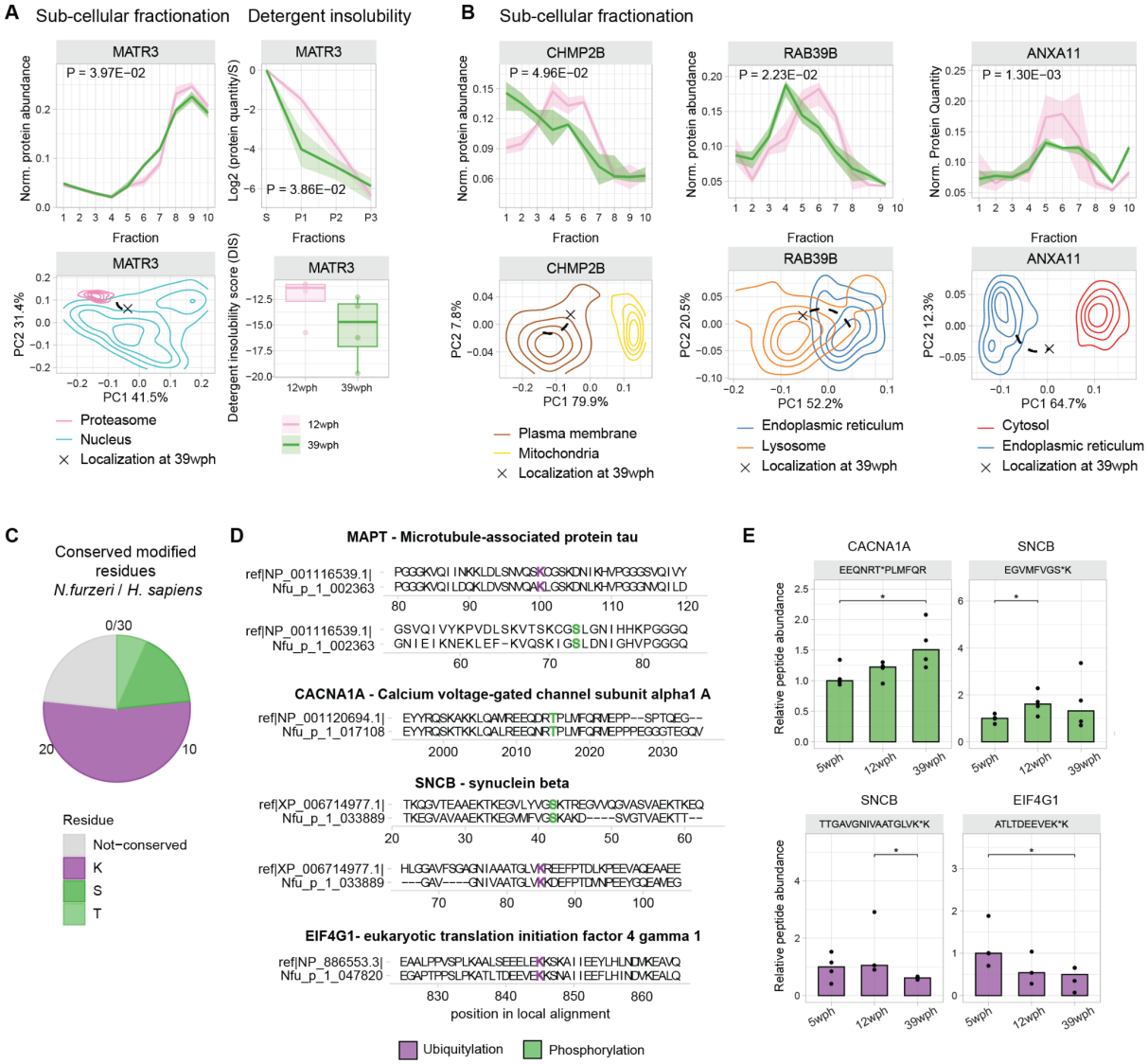

Figure S4: Age-associated alterations of proteins linked to human neurodegenerative disorders. A-B) Examples of proteins changing their subcellular localization profile or detergent insolubility. The top panels indicate either subcellular fractionation profiles (as in Figure 1D) or detergent insolubility profiles. For subcellular fractionation, in each of the plots, the x-axis indicates the 10 fractions obtained from LOPIT-DC and the y-axis indicates the total protein distribution along the 10 fractions for adult (12 wph, pink) and old (39 wph, green) fish. Shaded areas indicate 50% of the (N=4 pools) replicate distribution. P-values indicate the results of the Hotelling T2 test. For detergent insolubility profiles, the x-axis indicates the different detergent insolubility fractions: S=soluble, F1:F3=fractions after solubilization with buffers of increasing detergent strength (see methods, Figure S2A). The y-axis indicates log2 protein quantities relative to the soluble (S) fraction. The shaded area indicates 50% of the distribution across N=4 pools per age group. In the bottom panels, the PCA plot represents relocalization for each protein. The contour line represents the density distribution of the different organelles (calculated as the median between 12 wph and 39 wph), and the position of the protein at 39 wph is highlighted with a cross. The organelles represented are the ones that possess the higher absolute changes in the log2 ratios between Euclidean distances from the protein in the two age groups. Only for panel A, the boxplot on the right side indicates the detergent insolubility score in the two age groups. C) Pieplot showing conserved modified residues between *Nothobranchius furzeri* and humans that display changes in abundance with aging. Data refers to proteins involved in neurodegenerative diseases in humans. D) Local sequence alignments between *Nothobranchius furzeri* proteins (bottom sequence) and best human BLAST hit (upper sequence) for different proteins involved in neurodegenerative diseases. Modified residues are highlighted in purple (ubiquitylation) and green (phosphorylation). E) Barplots displaying significantly changing (P<0.05, moderated Bayes T-test) of modified peptides for the proteins shown in panel D. Asterisks indicate the P-value of the moderated Bayes T-test (N=3-4).

The values represent relative abundances to the young (5 wph) age group after correction for protein changes (see methods, Figure S3B). Related to Figure 1 and Table S3.

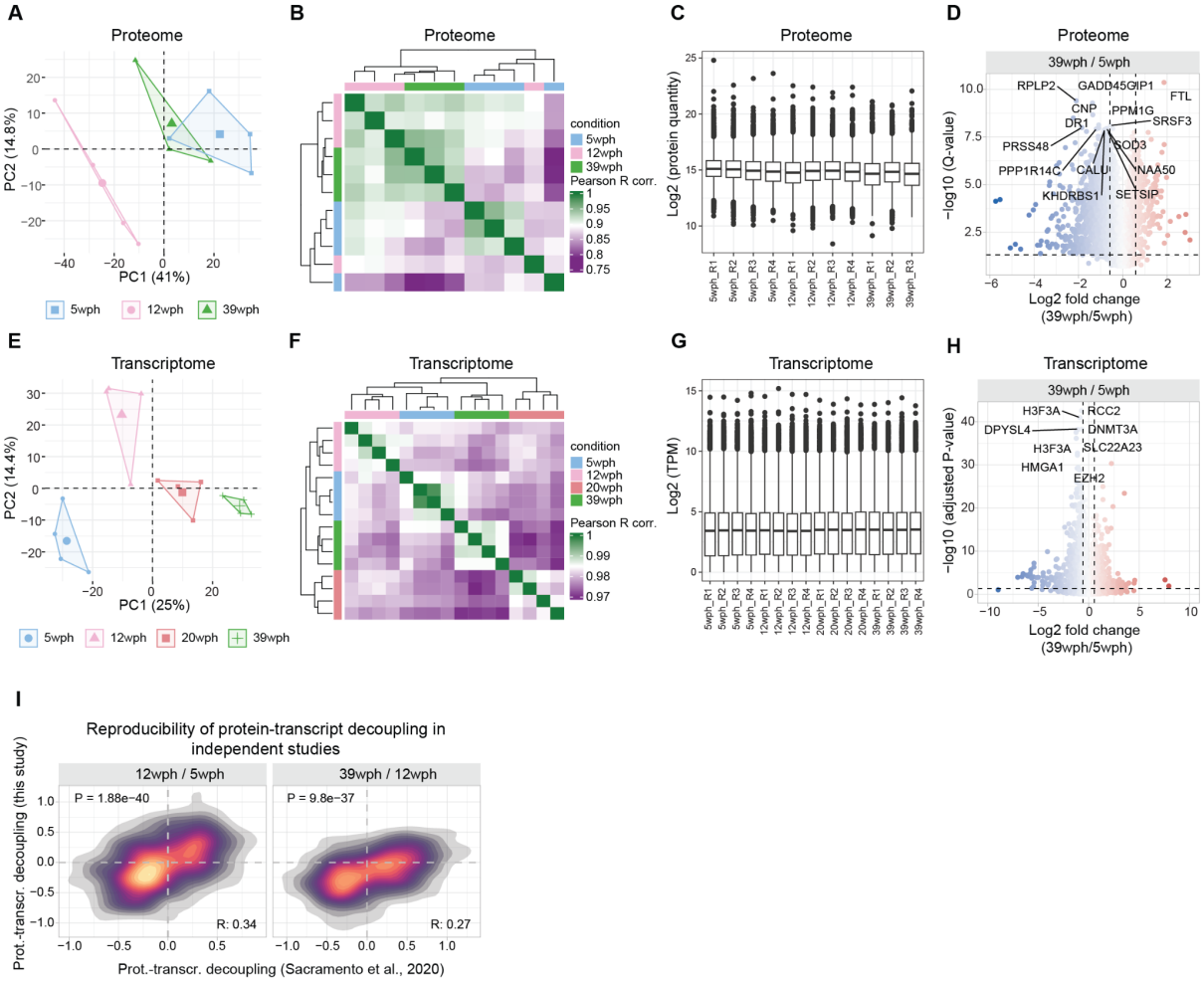

Figure S5: Proteome and transcriptome characterization of the killifish aging brain. A) Principal component analysis of proteomics data. B) Correlation heatmap between samples from the aging brain proteome data. Pairwise Pearson's R correlation coefficient was calculated on the log2 transformed protein abundances. C) Boxplot displaying the distribution of log2 transformed and normalized protein abundances. D) Volcano plot highlighting significant protein abundance changes in the aging brain (39 wph vs. 5 wph). Dashed lines indicate the threshold used to select differentially abundant proteins (absolute log2 FC > 0.58 and -log10 Q-value < 0.05) E) Principal component analysis of transcriptomics data. F) Correlation heatmap between samples from the aging brain transcriptome data. Pairwise Pearson's R correlation coefficient was calculated on the log2 transformed transcript per million reads (TPM). G) Boxplot displaying the distribution of log2 transformed and normalized transcript counts (TPM). H) Volcano plot highlighting significant transcript abundance changes in the aging brain (39 wph vs 5 wph). Dashed lines indicate the threshold used to select differentially expressed genes (absolute log2 FC > 0.58 and -log10 Adjusted P-value < 0.05). For displaying purposes, the X-axis range was limited to a -10:10 range leading to the exclusion of 1 gene. I) 2-D density plot showing the correlation between protein-transcript decoupling during aging in this study, displayed on the y-axis, and protein-transcript decoupling described in Sacramento et al., (2020) (x-axis). Related to Figure 2 and Table S4.

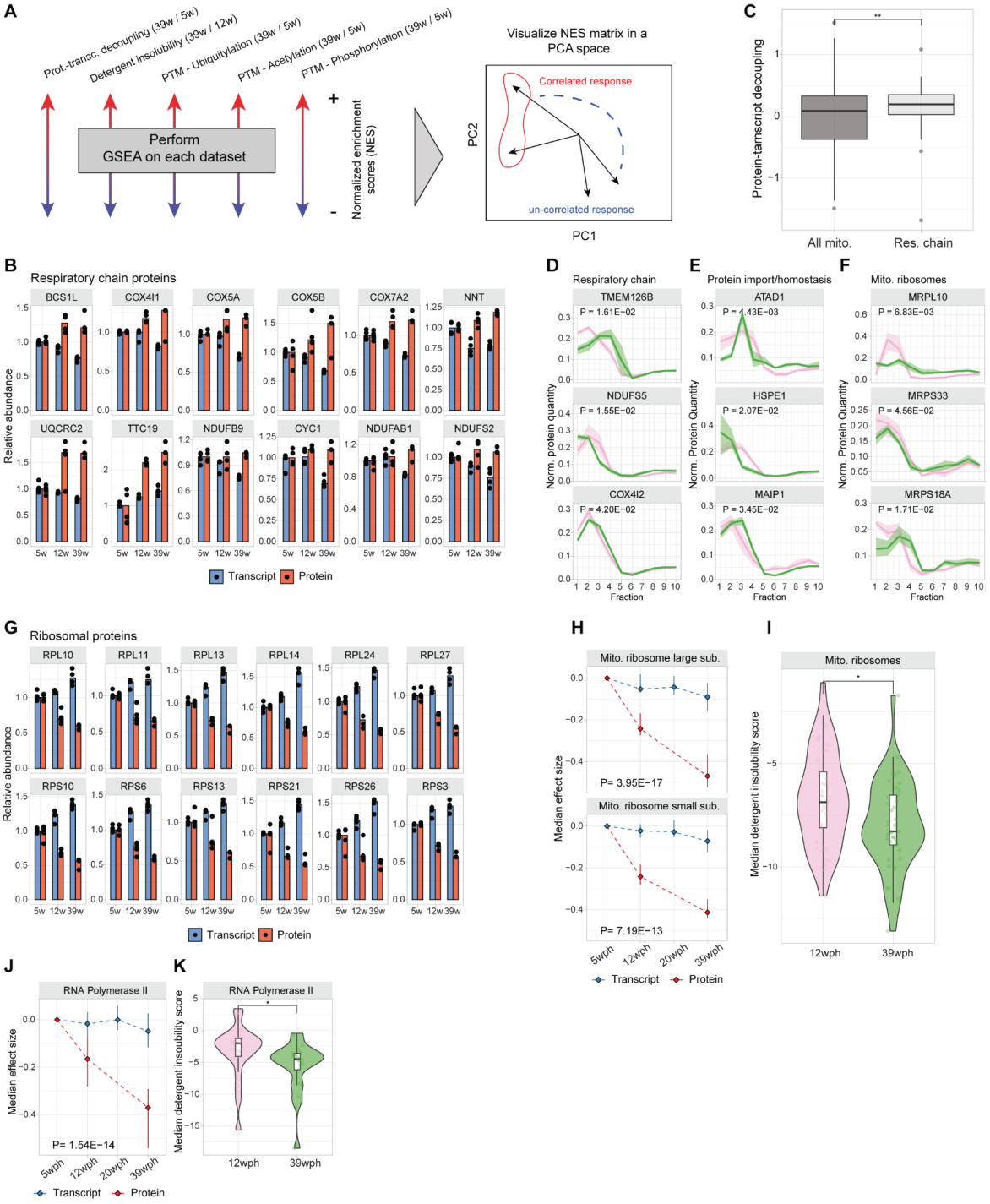

Figure S6: Alterations of ribosomal and respiratory chain proteins. A) Scheme of data integration strategy. For each dataset, a gene set enrichment analysis (GSEA) was performed using GO terms for cellular components. The normalized enrichment scores (NES) from each dataset were combined in a matrix and used as input for principal component analysis. B) Barplot showing transcript and protein abundances for oxidative phosphorylation protein. All the values were normalized to the 5 wph (young) age group (set to 1), N=3-4. C) Boxplot depicting the distribution of protein-transcript decoupling values (as defined in Figure 2A) for oxidative phosphorylation (light gray) proteins against the rest of the mitochondrial proteome (dark gray). Asterisks indicate the results of a two-sample Wilcoxon test. D-F) Examples of mitochondrial proteins that display changes in subcellular fractionation with aging. The x-axis indicates the 10 fractions obtained from LOPIT-DC, and the y-axis indicates the total protein distribution along the 10 fractions for adult (12 wph, pink) and old (39 wph, green) animals. Shaded areas indicate 50% of the replicate distribution from N=4 pools per group. P-values indicate the results of the Hotelling T2 test. G) Barplot showing transcript and protein abundances for cytoplasmic ribosomal protein. All the values were

normalized to the 5 wph (young) age group (set to 1), N=3-4. H) Line plot showing the trajectories for transcriptome (blue) and proteome (red) of mitochondrial large and small ribosomal subunits. Each point summarizes the median distribution of the log2 ratio of the quantities relative to the first (5 wph) age group, while the line bars indicate 50% of the distributions. P-values indicate the results of a MANOVA test run on the two multivariate distributions, N=3-4. I) Violin plot displaying detergent insolubility score for proteins of the mitochondrial ribosome (GO:0005761). Each dot represents the median insolubility score of each protein across N=4 pools per age group; asterisks indicate the results of a two-sample Wilcoxon test. J) Line plot showing the trajectories for transcriptome (blue) and proteome (red) for RNA Polymerase II enzyme. Each point summarizes the median distribution of the log2 ratio of the quantities relative to the first (5 wph) age group, while the line bars indicate 50% of the distributions. P-values indicate the results of a MANOVA test run on the two multivariate distributions, N=3-4. K) Violin plot displaying detergent insolubility score for proteins of the RNA Polymerase II enzyme (GO:0016591). Each dot represents the median insolubility score of each protein across N=4 pools per age group; asterisks indicate the results of a two-sample Wilcoxon test. *P ≤ 0.05; **P ≤ 0.01, ***P ≤ 0.001, ****P ≤ 0.0001. Related to Figure 3.

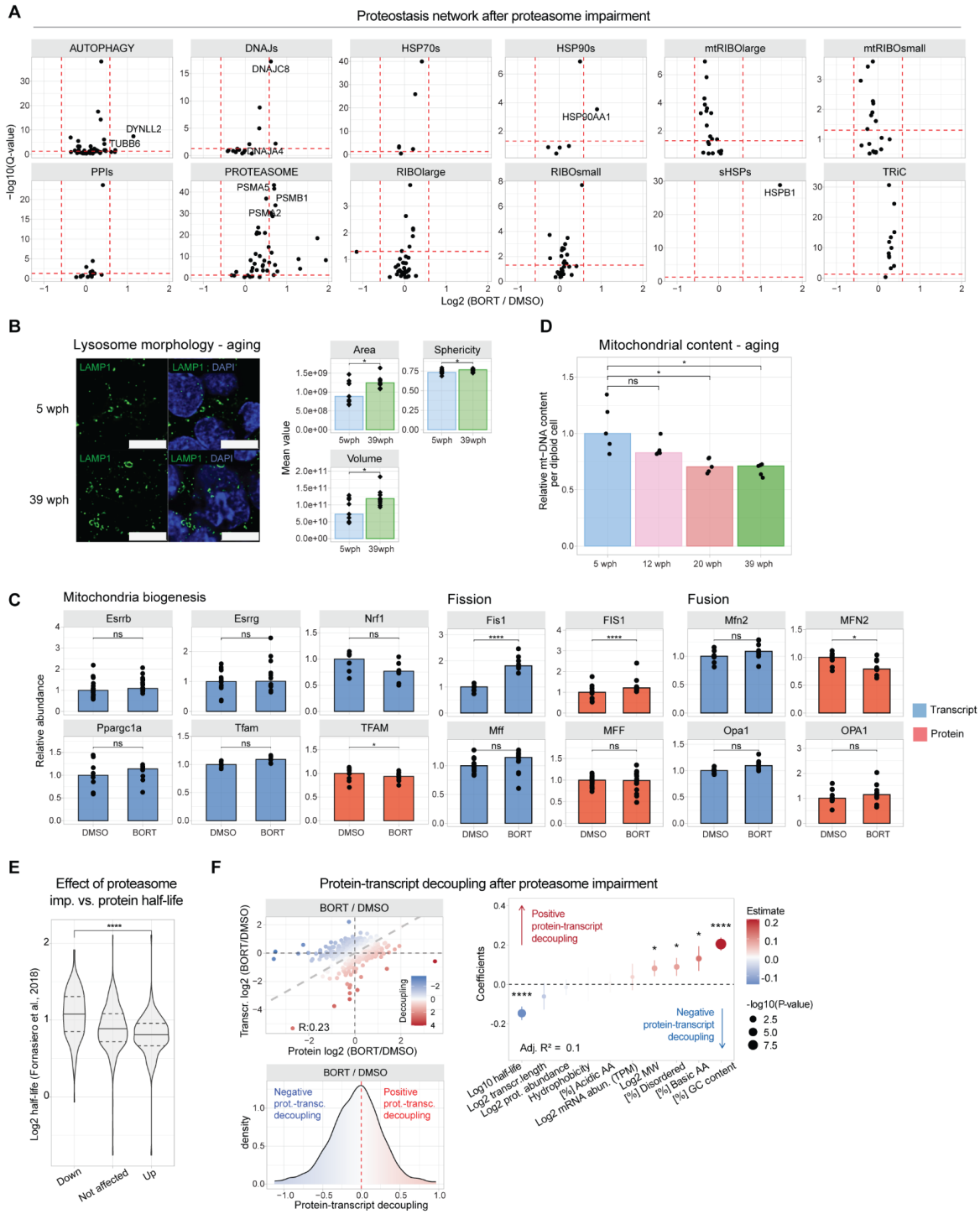

Figure S7: Effect of proteasome impairment on the killifish brain. A) Protein abundance changes induced by proteasome impairment for different components of the proteostasis network. B) (Right panel) Immunofluorescence stainings for lysosome (LAMP1) in brain cryo-sections of young (light blue) and old (green) *Nothobranchius furzeri*. Scale bars = 5µm. (Left panel) Barplot representation of lysosome morphology features in young (light blue) and old (green) samples. The y-axis represents the mean value of the different morphology features in each of the replicates (N=6).C) Effect of proteasome impairment on mitochondrial transcripts and proteins. For protein data, asterisks indicate the Q-value of the differential abundance testing performed with a two-sample T-test on the peptide abundances. For transcript data, asterisks indicate the Adjusted P-value of the differential abundance testing. N=10 . D) Quantification of mitochondrial DNA (mt-DNA) from killifish brains during aging. Relative mtDNA copy number was calculated using real-time quantitative PCR with primers for 16S rRNA mitochondrial gene and

Cdkn2a/b nuclear gene for normalization (N=5). Asterisks indicate the results of two-sample Wilcoxon tests. E) Violin plot showing the distribution of up and down-regulated proteins in response to proteasome impairment against their half-life as quantified in Fornasiero et al., 2018. Asterisks indicate the results of a two-samples Wilcoxon test. F) (Top left panel) Scatterplot comparing protein- (x-axis) and transcript-level (y-axis) fold changes in killifish after treatment with bortezomib. The color of each dot represents the decoupling score calculated as the difference between log2 transformed fold changes measured at the protein and transcript levels. Grey dashed lines indicate the equal changes between transcript and protein and, therefore, a zero decoupling score. (Bottom left panel) Density distribution of decoupling scores for comparing bortezomib vs. DMSO. On the right part, highlighted in red, are protein “gain” events (increase in protein abundance compared to the transcript), while on the left, in blue, are protein “loss” events (decrease in protein abundance compared to the transcript). (Right panel) Multiple linear regression analysis of decoupling scores in response to proteasome impairment based on biophysical features of transcripts or proteins as predictors. The x-axis indicates the estimate of the regression coefficient for each feature, while the size of the dots and asterisks represent the -log10 P-values of the F-test. *P ≤ 0.05; **P ≤ 0.01, ***P ≤ 0.001, ****P ≤ 0.0001. Related to Figure 4 and Table S5.

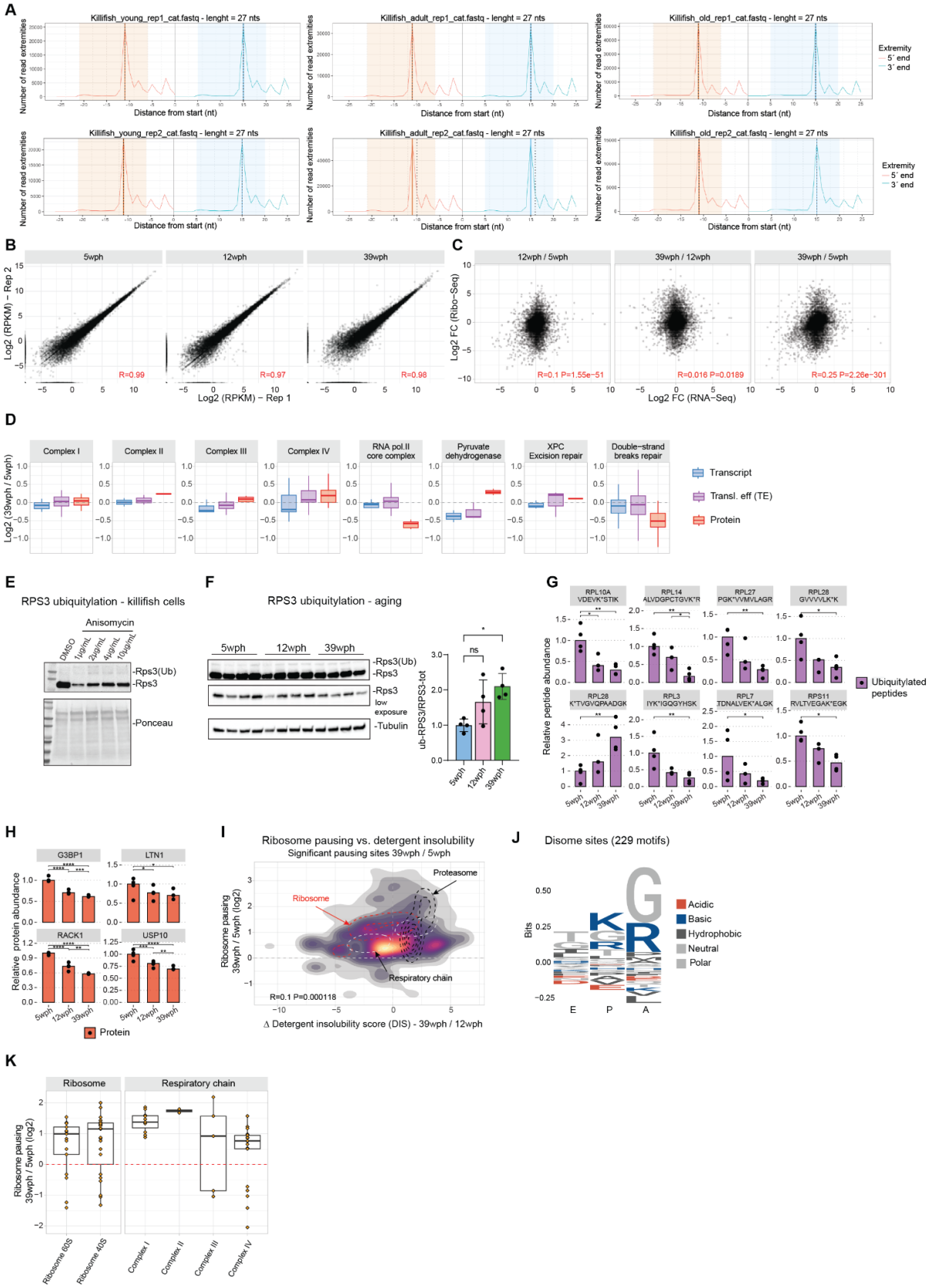

Figure S8: Ribosome profiling in the killifish aging brain. A) Tri-nucleotide plot showing characteristic triplet periodicity. The x-axis represents the distance from the starting codon (in nucleotide) and the y-axis the number of reads. B) Scatterplot showing the correlation between replicates for the Ribo-Seq experiment. On the different axis, the log2(RPKM) values from the different replicates are shown. C) Scatterplot showing the correlation between log2 fold changes for ribosome occupancy (y-axis) and changes in the transcriptome (x-axis) for different aging steps. D) Boxplot displaying differential modes of regulation for different protein complexes. On the x-axis are

displayed the different datasets: Transcriptome (green), Translation efficiency (purple), and Proteome (red). E) Immunoblot to detect RPS3 ubiquitylation in killifish cells treated with Anisomycin, which inhibits translation elongation and causes ribotoxic stress (Iordanov et al. 1997) for 24 hours. F) Immunoblot to detect RPS3 ubiquitylation across age groups. Barplot shows the ratio between the total RPS3 and its ubiquitylated fraction during aging. Asterisks indicate the results of an ordinary one-way ANOVA test (N=4). G) Barplots displaying significantly changing (P<0.05, moderated Bayes T-test) of ubiquitin-modified peptides for ribosomal proteins. Asterisks indicate the P-value of the moderated Bayes T-test (N=3-4). The values represent relative abundances to the young (5 wph) age group after correction for protein changes (see methods, Figure S3B). H) Barplot showing normalized protein abundance (relative to the first, 5 wph, age group set to 1) for factors associated with Ribosome-Quality-Control (RQC) pathways. The y-axis represents protein abundances relative to the first (5 wph) age groups. Asterisks indicate the Q-value of the differential abundance testing performed with a two-sample T-test on the peptide abundances, N=3,4 pools per group. I) 2-D density plot showing the relation between significant changes in pausing (Adjusted P-value < 0.05) displayed on the y-axis and changes in detergent insolubility metrics (x-axis). Each point in the distribution represents a significantly altered pausing site. Contour lines indicate the distribution of cytoplasmic ribosomes (red), Proteasome (black), and oxidative phosphorylation (white). J) Weblogo for disome pausing sites that display a strong increase in pausing (Pause score > 10). The y-axis displays the relative frequencies of the different residues, while the x-axis displays the different ribosome positions (E, P, A). K) Boxplot showing the distributions of pausing sites for cytoplasmic ribosomes (left panel) and respiratory chain complexes (right). Each dot represents a significantly altered (Adjusted P-value < 0.05) pausing site. The Y axis represents the log2 fold changes in pausing between 39 wph and 5 wph. *P ≤ 0.05; **P ≤ 0.01, ***P ≤ 0.001, ****P ≤ 0.0001. Related to Figure 5 and Table S6.

Materials and methods

Animal management practices

All experiments were performed in accordance with relevant guidelines and regulations. Fish were bred and kept in FLI's fish facility according to §11 of the German Animal Welfare Act under license number J-003798. The animal experiment protocols were approved by the local authority in the State of Thuringia (Veterinaer- und Lebensmittelueberwachungsamt; proteasome impairment: reference number 22-2684-04-FLI-19-010). Sacrifice and organ harvesting of non-experimental animals were performed according to §4(3) of the German Animal Welfare Act.

In vivo proteasome impairment

Adult animals (12–14 wph) were subjected to pharmacological intervention via intraperitoneal injections (IP) during a 4-weeks period of treatment. On each of the sixth day (t = 0, t = 6 d, t = 12d, t = 18d, t = 24d), fish were anesthetized with 200 mg/l buffered MS-222 (PharmaQ) and gently manipulated to deliver IP of Bortezomib at 500 µM or vehicle (1% DMSO in a physiological salt solution) at a dosage of 10 µl/g body weight. Animals from the same hatch were randomly allocated to the experimental groups. Both male and female fish were included in each experimental group. Individual brains from the fish were collected on the last day of treatment and snap-frozen in liquid nitrogen.

Proteasome activity assay

CT-L (chymotrypsin-like) proteasome activity was assayed with the hydrolysis of a specific fluorogenic substrate, Suc-LLVY-AMC (UBPBio, Catalog Number G1100). On the day of the experiment, brains were lysed in buffer (50 mM HEPES, pH 7.5 (Sigma Aldrich, H3375); 5 mM EDTA (Carl Roth, 8043.2); 150 mM NaCl (Carl Roth, 3957.1); 1 % (v/v) Triton X-100 (Carl Roth, 3051.3); 2 mM ATP (Sigma Aldrich, A2383) prepared with Milli-Q water) to a final estimated protein concentration of ~4 mg/mL and homogenized by sonication (Bioruptor Plus) for 10 cycles (30 sec ON/60 sec OFF) at high setting, at 4°C. Lysates corresponding to 10 µg protein were incubated in 50 mM Tris-HCl, pH 7.4, 5 mM MgCl2, 1 mM ATP, 1 mM DTT, 10% glycerol, and 10 µM proteasome substrate for 1 h at 37 °C. Specific proteasome activity was determined as the difference between the total activity of protein extracts and the remaining activity in the presence of 20 µM MG132 (Enzo Life Sciences, BML-PI102-0005). Fluorescence was measured by multiple reads for 60 min at 37°C by TECAN Kinetic Analysis (excitation 380 nm, emission 460 nm, read interval 5 min) on a Safire II microplate reader (TECAN).

Sample preparation for total proteome and analysis of PTMs

Snap-frozen brains were thawed and transferred into Precellys® lysing kit tubes (Keramik-kit 1.4/2.8 mm, 2 ml (CKM)) containing 150 µl of PBS supplemented with cOmplete™, Mini, EDTA-free Protease Inhibitor (Roche,11836170001) and with PhosSTOP™ Phosphatase Inhibitor (Roche, 4906837001). Based on estimated protein content (5% of fresh tissue weight), three to six brains were pooled to obtain ~1.5 mg of protein extract as starting material for each biological replicate. Tissues were homogenized twice at 6000 rpm for 30 s using Precellys® 24 Dual (Bertin Instruments, Montigny-le-Bretonneux, France), and the homogenates were transferred to new 2 ml Eppendorf tubes. Proteins were quantified using Pierce™ BCA Protein Assay Kit (Thermo Scientific, 23225), and 1.25 mg was processed for

further analysis. Volumes were adjusted using PBS and one-fourth of the volume equivalent of the 4× lysis (8% SDS, 100 mM HEPES, pH8) buffer was added. Samples were sonicated twice in a Bioruptor Plus for 10 cycles with 1 min ON and 30 s OFF with high intensity at 20 °C. The lysates were centrifuged at 18,407 x*g* for 1 min and transferred to new 1.5 ml Eppendorf tubes. Subsequently, samples were reduced using 10 mM DTT (Carl Roth, 6908) for 15 min at 45 °C and alkylated using freshly made 200 mM iodoacetamide (IAA) (Sigma-Aldrich, I1149) for 30 min at room temperature in the dark. An aliquot of each lysate was used for estimating the precise protein quantity using BCA (Thermo Scientific, 23225). Subsequently, proteins were precipitated using cold acetone, as described in (Buczak et al. 2020), and resuspended in 500 µl of digestion buffer (3 M urea, 100 mM HEPES pH 8.0). Aliquots corresponding to 20, 200, and 1000 µg protein were taken for proteome, phosphopeptides, and ubiquitylated/acetylated peptides enrichment, respectively, and digested using LysC 1:100 enzyme:proteins ratio for 4 hours (Wako sequencing grade, 125-05061) and trypsin 1:100 enzyme:proteins ratio for 16 hours (Promega sequencing grade, V5111). The digested proteins were then acidified with 10% (v/v) trifluoroacetic acid and desalted using Waters Oasis® HLB µElution Plate 30 µm (2, 10, and 30 mg, depending on the amount of starting material) following manufacturer instructions. The eluates were dried down using a vacuum concentrator and reconstituted in MS buffer A (5% (v/v) acetonitrile, 0.1% (v/v) formic acid). For PTM enrichment, peptides were further processed as described below. For Data Independent Acquisition (DIA) based analysis of total proteome, samples were transferred to MS vials, diluted to a concentration of 1 µg/µL, and spiked with iRT kit peptides (Biognosys, Ki-3002-2) prior to analysis by LC-MS/MS.

Sequential enrichment of ubiquitylated and acetylated peptides

Ubiquitylated and acetylated peptides were sequentially enriched starting from ~1000 µg of dried peptides per replicate. For the enrichment of ubiquitylated peptides, the PTMScan® HS Ubiquitin/SUMO Remnant Motif (K-ε-GG) kit (Cell Signaling Technology, 59322) was used following manufacturer instructions. The K-ε-GG modified enriched fraction was desalted and concentrated as described above, dissolved in MS buffer A, and spiked with iRT kit peptides prior to LC-MS/MS analysis.

The flowthrough fractions from the K- ε -GG enrichment were acidified with 10% (v/v) trifluoroacetic acid and desalted using Oasis® HLB µElution Plate 30 µm (30 mg) following manufacturer instructions. Acetylated peptides were enriched as described by Di Sanzo et al. 2021. Briefly, dried peptides were dissolved in 1000 µl of IP buffer (50 mM MOPS pH 7.3, 10 mM KPO_4 pH 7.5, 50 mM NaCl, 2.5 mM Octyl β-D-glucopyranoside) to reach a peptide concentration of 1 µg/µL, followed by sonication in a Bioruptor Plus (5 cycles with 1 min ON and 30 s OFF with high intensity at 20 °C). Agarose beads coupled to an antibody against acetyl-lysine (ImmuneChem Pharmaceuticals Inc., ICP0388-5MG) were washed three times with washing buffer (20 mM MOPS pH 7.4, 10 mM KPO4 pH 7.5, 50 mM NaCl) before incubation with each peptide sample for 1.5 h on a rotating well at 750 rpm (STARLAB Tube roller Mixer RM Multi-1). Samples were transferred into Clearspin filter microtubes (0.22 µm) (Dominique Dutscher SAS, Brumath, 007857ACL) and centrifuged at 4 °C for 1 min at 2000 x*g*. Beads were washed first with IP buffer (three times), then with washing buffer (three times), and finally with 5 mM ammonium bicarbonate (three times). Thereupon, the enriched peptides were eluted first in basic condition using 50 mM aqueous NH3, then using 0.1% (v/v) trifluoroacetic acid in 10% (v/v) 2-propanol and finally with 0.1% (v/v) trifluoroacetic acid. Elutions were dried down and reconstituted in MS buffer A (5% (v/v) acetonitrile, 0.1% (v/v) formic acid), acidified with 10% (v/v) trifluoroacetic acid, and then desalted with Oasis® HLB

µElution Plate 30 µm. Desalted peptides were finally dissolved in MS buffer A, spiked with iRT kit peptides and analyzed by LC-MS/MS.

Enrichment of phosphorylated peptides

Lysates (corresponding to ~200 µg of protein extract) were acetone precipitated, digested into peptides, and desalted, as described in ‘‘Sample preparation for total proteome and analysis of PTMs’’. The last desalting step was performed using 50 µl of 80% ACN and 0.1% TFA buffer solution. Before phosphopeptide enrichment, samples were filled up to 210 µl using 80% ACN and 0.1% TFA buffer solution. Phosphorylated peptides were enriched using Fe(III)-NTA cartridges (Agilent Technologies, G5496-60085) in an automated fashion using the standard protocol from the AssayMAP Bravo Platform (Agilent Technologies). In short, Fe(III)-NTA cartridges were first primed with 100 µl of priming buffer (100% ACN, 0.1% TFA) and equilibrated with 50 µL of buffer solution (80% ACN, 0.1% TFA). After loading the samples into the cartridge, the cartridges were washed with an OASIS elution buffer, while the syringes were washed with a priming buffer (100% ACN, 0.1% TFA). The phosphopeptides were eluted with 25 µL of 1% ammonia directly into 25 µL of 10% FA. Samples were dried down with a speed vacuum centrifuge and stored at −20 °C until LC-MS/MS analysis.

Subcellular fraction of killifish brain by LOPIT-DC

All the following steps were performed at 4°C, keeping samples on ice unless stated otherwise. Fresh brains from adult (12 wph) and old (39 wph) killifish were pooled to reach ~150 mg of wet tissue weight per biological replicate. A mixture of male and female fish was used. Fresh brain tissue was subsequently transferred to a 15 mL Potter homogenizer (Fisher Scientific, 15351321) together with 7.5 mL of lysis buffer (LB) (250 mM sucrose, 10 mM HEPES ph 8.0, 2 mM MgAc, 2 mM EDTA) supplemented with Protease Inhibitor (Roche,11836170001) and homogenized with ~60 gentle strokes. The brain homogenate was then transferred in a 15mL Falcon tube and treated with Benzonase (Merk, 70664) for 20 min at room temperature. An aliquot of 2.5 mL homogenate was collected for each sample and stored at -80°C to be later processed for differential detergent extraction (see below). The remaining 5 mL were transferred to a 5 mL Eppendorf tube and centrifuged at 500 x*g* for 5 min at 4°C to remove cell debris and unlysed cells. Subsequently, the clarified homogenate was centrifuged at 1000 x*g* for 13 min at 4°C and the resulting pellet was collected as the first subcellular fraction (01). Following one additional centrifugation at 1000 x*g* for 7 minutes, the supernatant was then divided into 4 x 1.5 mL Ultracentrifuge Tubes (Beckman) and processed for differential ultracentrifugation step with an Optima TLX-BenchTop Ultracentrifuge (Beckman, 8043-30-1197), using a TLA55 rotor (Beckman, 366725), using the following ultracentrifugation settings:

xg	*Time*	*Fraction*	*Temperature*
3000	10’	02	4°C
5000	10’	03	4°C
9000	15’	04	4°C
12000	15’	05	4°C
15000	15’	06	4°C
30000	20’	07	4°C
79000	43’	08	4°C
120000	45’	09	4°C
—	—	10 (final supernatant, cytosol enriched)	

Pellets from each centrifugation step were resuspended in 50 µL of PBS, and proteins were solubilized by adding 50 µL of 2x lysis buffer (200 mM HEPES pH 8.0, 100 mM DTT, 4% (w/v) SDS). For fraction 10 (cytosol enriched), 300µL was taken and supplemented with 300 µL of 2x lysis buffer. All the samples were then sonicated using a Bioruptor Plus (Diagenode) for 5 cycles with 60 sec ON and 30 sec OFF with max intensity, boiled for 10 min at 95°C, and a second sonication cycle was performed. The solubilized proteins were reduced with 200mM DTT for 15 min at 45°C and alkylated using freshly made 200mM IAA for 30 min at room temperature in the dark. Subsequently, proteins were precipitated using cold acetone, dissolved in 1 M guanidine HCl in 100 mM HEPES pH8.0, and digested using LysC and trypsin, as described in (Buczak et al. 2020). The digested proteins were then acidified with 10 % (v/v) trifluoroacetic acid and desalted using Oasis® HLB µElution Plate 30 µm following manufacturer instructions. The eluates were dried down using a vacuum concentrator and reconstituted in 5 % (v/v) acetonitrile, 0.1 % (v/v) formic acid. Samples were transferred directly to MS vials, diluted to a concentration of ~1 µg/µL, and spiked with iRT kit peptides prior to analysis by LC-MS/MS.

Differential detergent extraction

All the following steps were performed at 4°C, keeping samples on ice unless stated otherwise. For each replicate, 2.5 mL of brain homogenate was thawed on ice. After thawing, the homogenate was centrifuged at 500 x*g* for 5 min at 4°C to remove debris. The supernatant was collected, and 64 µL of 20% (v/v) IGEPAL Nonidet P-40 (Sigma) was added to reach an initial concentration of 0.5% (v/v). The homogenate was then divided into 4x 1.5mL ultracentrifuge tubes and sonicated in a Bioruptor Plus for 10 cycles with 30 min ON and 30 s OFF with max intensity at 24 °C. The homogenates were then loaded into a TLA55 rotor and ultracentrifuged with an Optima TLX-BenchTop Ultracentrifuge at 100,0000 x*g* for 5 min at 24°C. After ultracentrifugation, the supernatants were collected and stored as “soluble” (S) fraction. The remaining pellets were resuspended in 1mL of buffer A (10 mM HEPES pH 8.0, 2 mM MgAc, 2 mM EDTA, 0.5% NP-40), samples were mixed by vortexing, and sonicated in a Bioruptor Plus for 10 cycles with 30 s ON and 30 s OFF with max intensity at 24 °C. Samples

were then ultracentrifuged again at 100,0000 x*g* for 5 min at 24°C. The supernatants ("F1") were collected and the remaining pellets were resuspended in 1mL of buffer B (10 mM HEPES pH 8.0, 2 mM MgAc, 2 mM EDTA, 0.5% NP-40, 0.25% SDS, 0.5% deoxycholic acid), mixed, sonicated, and centrifuged as above. The supernatants ("F2") were collected and the remaining pellets were resuspended in 1mL of buffer C (10 mM HEPES pH 8.0, 2 mM MgAc, 2 mM EDTA, 0.5% NP-40, 2% SDS, 0.5% deoxycholic acid), mixed, sonicated, and centrifuged as above. The supernatants ("F3") and the remaining pellets were collected. All the collected samples were stored at -80°C until further analysis.

Data independent acquisition for proteome quantification

Peptides were separated in trap/elute mode using the nanoAcquity MClass Ultra-High Performance Liquid Chromatography system (Waters, Waters Corporation, Milford, MA, USA) equipped with trapping (nanoAcquity Symmetry C18, 5 µm, 180 µm × 20 mm) and an analytical column (nanoAcquity BEH C18, 1.7 µm, 75 µm × 250 mm). Solvent A was water and 0.1% formic acid, and solvent B was acetonitrile and 0.1% formic acid. 1 µl of the samples (~1 µg on column) were loaded with a constant flow of solvent A at 5 µl/min onto the trapping column. Trapping time was 6 min. Peptides were eluted via the analytical column with a constant flow of 0.3 µl/min. During the elution, the percentage of solvent B increased nonlinearly from 0–40% in 120 min. The total run time was 145 min, including equilibration and conditioning. The LC was coupled to an Orbitrap Exploris 480 (Thermo Fisher Scientific, Bremen, Germany) using the Proxeon nanospray source. The peptides were introduced into the mass spectrometer via a Pico-Tip Emitter 360-µm outer diameter × 20-µm inner diameter, 10-µm tip (New Objective) heated at 300 °C, and a spray voltage of 2.2 kV was applied. The capillary temperature was set at 300°C. The radio frequency ion funnel was set to 30%. For DIA data acquisition, full scan mass spectrometry (MS) spectra with a mass range 350–1650 m/z were acquired in profile mode in the Orbitrap with the resolution of 120,000 FWHM. The default charge state was set to 3+. The filling time was set at a maximum of 60 ms with a limitation of 3 × 106 ions. DIA scans were acquired with 40 mass window segments of differing widths across the MS1 mass range. Higher collisional dissociation fragmentation (stepped normalized collision energy; 25, 27.5, and 30%) was applied, and MS/MS spectra were acquired with a resolution of 30,000 FWHM with a fixed first mass of 200 m/z after accumulation of 3×10^6 ions or after filling time of 35 ms (whichever occurred first). Data were acquired in profile mode. For data acquisition and processing of the raw data, Xcalibur 4.3 (Thermo) and Tune version 2.0 were used.

Data processing for MS-DIA samples

Spectral libraries were created by searching the DIA or/and DDA runs using Spectronaut Pulsar (14.9.2 and 15.3.2, Biognosys, Zurich, Switzerland). The data were searched against species-specific protein databases (Nfu_20150522, annotation nfurzeri_genebuild_v1.150922) with a list of common contaminants appended. The data were searched with the following modifications: carbamidomethyl (C) as fixed modification, and oxidation (M), acetyl (protein N-term), lysine di-glycine (K-ε-GG), phosphorylated tyrosine (T) and serine (S) and acetyl-lysine (K-Ac) as variable modifications for the respective PTMs enrichments. A maximum of 3 missed cleavages were allowed for K-Ac and K-ε-GG modifications, 2 missed cleavages were allowed for phospho enrichment. The library search was set to 1 % false discovery rate (FDR) at both protein and peptide levels. DIA data were

then uploaded and searched against this spectral library using Spectronaut Professional (v14.9.2 and 15.3.2) and default settings. Relative quantification was performed in Spectronaut for each pairwise comparison using the replicate samples from each condition using default settings, except:

Dataset	***Software version***	***Test***	***Data Filtering***	***Imputation***	***Normalization***
Aging proteome	15.3.2	Unpaired t-test	Q-value	Global Imputing	True, Automatic
LOPIT-DC	14.9.2	NA	Q-value percentile 0.2	Run Wise Imputing	True, Global
Detergent insolubility	15.4.2	NA	Q-value percentile 0.2	Run Wise Imputing	False
Proteasome Inhibition	14.9.2	Unpaired t-test	Q-value	Global Imputing	True, Automatic
PTMs - Ubiquitin	15.4.2	–	Q-value percentile 0.2	Global Imputing	True, Automatic
PTMs - Phosphorylation	15.4.2	–	Q-value percentile 0.2	Global Imputing	True, Automatic
PTMs - Acetylation	15.4.2	–	Q-value percentile 0.2	Global Imputation	True, Automatic

Candidates and report tables were exported from Spectronaut and used for downstream analysis.

Immunoblot

Killifish brains and cells treated for 24 hours with anisomycin (Cell Signaling Technology, 2222) were lysed following as described in “Sample preparation for total proteome and analysis of PTMs”. Protein concentration was estimated by Qubit assay (Invitrogen, Q33211), and 30 µg of proteins were used. 4× loading buffer (1.5 M Tris pH 6.8, 20% (w/v) SDS, 85% (v/v) glycerin, 5% (v/v) β-mercaptoethanol) was added to each sample and then incubated at 95 °C for 5 minutes. Proteins were separated on 4–20% Mini-Protean® TGX™ Gels (BioRad, 4561096) by sodium dodecyl sulfate-polyacrylamide gel electrophoresis (SDS-PAGE) using a Mini-Protean® Tetra Cell system (BioRad, Neuberg, Germany, 1658005EDU). Proteins were transferred to a nitrocellulose membrane (Carl Roth, 200H.1) using a Trans-Blot® Turbo™ Transfer Starter System (BioRad, 1704150). Membranes were stained with Ponceau S (Sigma, P7170-1L) for 5 min on a shaker (Heidolph Duomax 1030), washed with Milli-Q water, imaged on a Molecular Imager ChemiDocTM XRS + Imaging system (BioRad) and destained by 2 washes with PBS and 2 washes in TBST (Tris-buffered saline (TBS, 25 mM Tris, 75 mM

NaCl), with 0.5% (v/v) Tween-20) for 5 min. After incubation for 5 min in EveryBlot blocking buffer (Biorad, 12010020), membranes were incubated overnight with primary antibodies against RPS3 (Bethyl Laboratories, A303-840A-T) or α-tubulin (Sigma, T9026) diluted (1:1000) in enzyme dilution buffer (0.2% (w/v) BSA, 0.1% (v/v) Tween20 in PBS) at 4 °C on a tube roller (BioCote® Stuart® SRT6). Membranes were washed 3 times with TBST for 10 min at room temperature and incubated with horseradish peroxidase coupled secondary antibodies (Dako, P0448/P0447) at room temperature for 1 h (1:2000 in 0.3% (w/v) BSA in TBST). After 3 more washes for 10 min in TBST, chemiluminescent signals were detected using ECL (enhanced chemiluminescence) Pierce detection kit (Thermo Fisher Scientific, Waltham, MA, USA, #32109). Signals were acquired on the Molecular Imager ChemiDocTM XRS + Imaging system and analyzed using the Image Lab 6.1 software (Biorad). Membranes were stripped using stripping buffer (1% (w/v) SDS, 0.2 M glycine, pH 2.5), washed 3 times with TBST, blocked, and incubated with the second primary antibody, if necessary.

RNA isolation for RNA-Seq analysis

Individual brains from the fish were collected and snap-frozen in liquid nitrogen. The protein amount was estimated based on fresh tissue weight (assuming 5% of protein w/w), and ice-cold 1x PBS with protease/ phosphatase inhibitors (Roche,11836170001, 4906837001) was added accordingly to a final concentration of 2 µg/µL. Samples were then vortexed (5 times) before sonication (Bioruptor Plus) for 10 cycles (60 sec ON/30 sec OFF) at the high setting, at 4 °C. The samples were then centrifuged at 3000 x*g* for 5 min at 4 °C, and the supernatant was transferred to 2 mL Eppendorf tubes. 1.5 mL of ice-cold Qiazol (Qiagen, 79306) reagent was added to 150 µL of homogenate, vortexed five times, and snap-frozen in liquid nitrogen. On the day of the experiment, samples were thawed on ice, vortexed five times, and incubated at room temperature for 5 min before adding 300 µL of chloroform. Samples were mixed vigorously, incubated for 3 min at room temperature, and centrifuged at 12000 x*g* for 20 min at 4 °C. The upper aqueous phase (600 µL) was carefully transferred into a fresh tube, and the remaining volume (phenol/chloroform phase) was kept on ice for DNA isolation. The aqueous phase was mixed with 1.1 volume of isopropyl alcohol, 0.16 volumes of sodium acetate (2 M; pH 4.0), and 1 µL of GlycoBlue (Invitrogen, AM9515) to precipitate RNA. After 10 min incubation at room temperature, samples were centrifuged at 12000 x*g* for 30 min at 4 °C. The supernatant was completely removed, and RNA pellets were washed by adding 80% (v/v) ethanol and centrifuging at 7500 x*g* for 5 min at 4 °C. The washing steps were performed twice. The resulting pellets were air-dried for no more than 5 min and dissolved in 10 µL nuclease-free water. To ensure full dissolution of RNA in water, samples were then incubated at 65 °C for 5 min, before storage at -80 °C.

RNA-Seq library preparation

Sequencing of RNA samples was done using Illumina's next-generation sequencing methodology (Bentley et al. 2008). In detail, quality check and quantification of total RNA was done using the Agilent Bioanalyzer 2100 in combination with the RNA 6000 pico kit (Agilent Technologies, 5067-1513). Total RNA library preparation was done by introducing 500 ng total RNA into Illumina's NEBNext Ultra II directional mRNA (UMI) kit (NEB, E7760S), following the manufacturer's instructions. The quality and quantity of all libraries were checked using Agilent's Bioanalyzer 2100 and DNA 7500 kit (Agilent Technologies, 5067-1506).

RNA-Seq sequencing

All libraries were sequenced on a NovaSeq6000 SP 300 cycles v1.5; paired-end 151 bp (one pair for each of the projects). Total RNA libraries were pooled and sequenced in three lanes. Small RNA libraries were pooled and sequenced in one lane. Sequence information was extracted in FastQ format using Illumina's bcl2FastQ v2.20.0.422, against the *Nothobranchius furzeri* reference genome (Nfu_20150522, annotation nfurzeri_genebuild_v1.150922). Alignment to the reference genome was performed using STAR (Dobin et al. 2012) with the following parameters: --outSAMmultNmax 1 --outFilterMultimapNmax 1 --outFilterMismatchNoverLmax 0.04 --sjdbOverhang 99 --alignIntronMax 1000000 --outSJfilterReads Unique. The deduplication step was performed using the umi_tool v1.1.1 (Smith, Heger, and Sudbery 2017), using the following parameters: extract --bcpattern= NNNNNNNNNNN`, `dedup --chimeric-pairs discard --unpaired-reads discard -- paired.

RNA-Seq quantification and differential expression

RNA-Seq data were then processed as follows: quantification was performed using featurecounts v2.0.3 (Liao, Smyth, and Shi 2013) with the following parameters -s 2 -p -B --countReadPairs. Differential expression analysis was performed using the DESeq2 package (v1.34.0) (Love, Huber, and Anders 2014). Raw count data were normalized using the transcript per million strategy.

Ribo-Seq library preparation

Ribosome profiling libraries were prepared following previously published protocol with modifications (Stein et al., 2022). 10~15 brain samples from fish were combined and lysed frozen using Cryo-Mill (Retsch, MM301) in the presence of 1ml of lysis buffer (20 mM Tris-HCl pH 7.5, 140 mM KCl, 5 mM MgCl2, 1 mM DTT, 100 µg/ml Cycloheximide, 1% Triton X-100, and 1 X Protease Inhibitor). Lysed powder was quickly thawed in a water bath at room temperature and spun at 21,000 g for 15 minutes at 4 °C to clear lysate. RNAse I (Invitrogen, AM2294) was added to 0.4U/µg of RNA and incubated at 25 °C for 45 minutes. Digestion was stopped by adding 0.4U/µg of SUPERaseIn RNAse Inhibitor (Invitrogen, AM2696). RNAse-treated lysate was layered on 900 µl sucrose cushion buffer (20 mM Tris-HCl pH 7.5, 140 mM KCl, 5 mM MgCl2, 1 mM DTT, 100 µg/ml Cycloheximide, 0.02U/µl SuperaseIn, 1M Sucrose), and spun at 100,000 rpm for 1 hour at 4 °C in TLA100.3 rotor. Resulting ribosome pellet was resuspended in 250 µl of lysis buffer with SuperaseIn and RNA was extracted using TRIzol reagent (Invitrogen, 15596026) following manufacturer's protocol. 27-34bp fragments were isolated from denaturing gel, ligated to adapter (NEB, S1315S), and ribosomal RNA was removed using RiboCop (Lexogen, 144.24) mixed with custom depletion DNA oligos (Table 2). Remaining fragments were reverse transcribed, circularized, and PCR amplified following the steps described previously (McGlincy and Ingolia 2017). Barcoded samples were pooled and sequenced using Hiseq 4000 (Illumina).

Imaging

Cryo-sections preparation and free-floating immunofluorescence

To prepare brain cryo-sections for free-floating immunofluorescence from 5 wph and 39 wph old killifish, brains were dissected and fixed ON in a solution of 4% paraformaldehyde PFA in PBS at 4°C. The samples were then equilibrated in a 30% sucrose solution ON at 4° and subsequently embedded in cryo-protectant (Tissue -Tek O.C.T. Compound; Sakura Finetek,

USA). Tissue slices of 50mm thickness were cut at a cryostat (Leica) and stored on glass slides (Thermo Fisher Scientific, USA).

Free-floating immunofluorescence experiments were performed by adapting previous protocols for classical on-slide immunofluorescence (Sara Bagnoli, Terzibasi Tozzini, and Cellerino 2023). Briefly, the sections were washed in PBS to remove the cryo-embedding medium and detached from the glass slide. The sections were then placed in 24-wells and performed two additional washes in PBS for 5 min each. Afterward, an acid antigen retrieval step (10 mM Tri-sodium citrate dihydrate, 0.05% tween, at pH 6) was performed by bringing the solution to boiling point in a microwave and adding 50ml of it in each well, leaving the solution for 5 minutes. This step was repeated two times.. 500 ml of blocking solution (5% BSA, 0.3% Triton-X in PBS) was then applied for 2 h. Primary antibodies (Phospho-Tau AT100, NeuN or Lamp1 Table 1) at the proper dilution were added in a solution of 1% BSA, 0.1% triton in PBS, and left overnight at 4°C in slow agitation on a rocker. Next day, the proper secondary antibodies (Table 1) at a 1:500 dilution were used in the same solution. After 2h of incubation, slices were washed three times with PBS, counter-stained with a solution 1:10000 of Hoechst 33342 (Invitrogen, USA) for two minutes and manually mounted under a stereomicroscope on Superfrost Plus glass slides (Thermo Fisher Scientific, USA). Finally, Fluoroshield mounting medium (Sigma, USA) was used and slices were covered with a coverglass (Thermo Fisher Scientific, USA).

Image acquisition

Imaging of lysosomal staining was performed with a Zeiss scanning confocal microscope (LSM900, Zeiss, Germany) equipped with an Airyscan module. Nine consecutive z planes with a step of 300nm were acquired with a 63x oil immersion objective (Plan-Apochromat 63x/1.4 Oil DIC M27, Zeiss, Germany) at a resolution of 2186x2186 pixels with the use of Airyscan. Images were then deconvoluted in the Zeiss Zen blue 3.7 suite using the Fast Iterative algorithm and exported as tiff for further analysis in Imaris (Bitplane, UK).

Samples processed for Tau stainings were imaged with an Axio Imager Z.2 (Zeiss, Germany) equipped with an Apotome slide using a 63x oil immersion objective (Plan-Apochromat 63x/1.4 Oil DIC M27, Zeiss, Germany). Z-stacks were realized by acquiring five consecutive z-planes at an interval of 1 micron. Images were then processed in imageJ (Fiji).

Lysosomes morphological analysis

To analyze the change in morphology of lysosomes in aging, we analyzed nine 5 wph samples and twelve 39 wph samples. To study morphological changes in case of proteostasis alteration, samples from six bortezomib-treated animals and six controls (DMSO treated) were analyzed. Tiff images were loaded in Imaris (Bitplane, UK) to recreate a 3D rendering of the samples. A version of the ‘Surfaces’ algorithm was created, optimizing the settings to realize an optimal mask of single lysosomes. Statistics obtained (Area, Volume, Mean intensity, and Sphericity) were extracted, and mean values for each animal were calculated. Data significance was tested using a two-tails T-test.

Mean fluorescence intensity analysis

To analyze differences in the amount of Tau phosphorylation between young (5 wph) and old (39 wph) *Nothobranchius furzeri* brain samples, we performed mean fluorescence intensity (MFI) analysis in the free license software ImageJ (Fiji). Since Tau is a neuronal protein, and the number of neurons between young and old animals varies, we normalized the MFI of Tau

staining over the MFI of NeuN, a neuronal-specific marker, in order to render the Tau MFI proportional to the number of neurons. Images were opened in ImageJ (Fiji), and median filtering (1px radius) was applied. The average intensity projection was realized, and MFI for the green channel (Tau) and red channel (NeuN) was measured and reported in an Excel table. Tau MFI for each animal was divided by the corresponding NeuN MFI, and the significance of the results was tested by a two-tails T-test.

Primary Antibody	**Producer**	**Catalog Number**	**Type**	**Working dilution**
Lamp1	Abcam	Ab24170	Polyclonal Rabbit	1:500
NeuN	Abcam	Ab177487	Monoclonal Rabbit	1:500
Phospho-Tau AT100	Thermo Fisher Scientific	MN1060	Monoclonal Mouse	1:400
Secondary Antibody				
AlexaFluor 488 anti-Rabbit	Invitrogen	A11001	Goat IgG	1:500
AlexaFluor 568 anti-Rabbit	Invitrogen	A11011	Goat IgG	1:500
AlexaFluor 488 anti-Mouse	Invitrogen	A11004	Goat IgG	1:500

Table 1: List of antibodies utilized in this work

Oligo #1	GGCCGTTACCGGCCTCACACCGTCCATGGGATGAGC/3BioTEG/
Oligo #2	CGGGCGAGACGGGCCGGTGGTGCGCCCGGGAAC/3BioTEG/
Oligo #3	CGCCTCCCCGCCTCACCGGGTAAGTGAAAAAACGATAAGAG/3BioTEG/
Oligo #4	GCACGCGCCGGGCGCTTGACACCAGAACCGAGAGC/3BioTEG/

Table 2: List of DNA oligonucleotides used for ribosomal RNA depletion

Data analysis

Protein subcellular localization by LOPIT-DC

For each age group and replicate, protein distribution profiles were calculated by dividing the scaled protein quantity in each fraction by the total sum of protein quantity across all fractions. Protein markers for the different compartments were taken from the Bioconductor package pRoloc (Crook et al. 2019), by mapping *Nothobranchius furzeri* entries onto *Homo sapiens* entries via orthologues mapping. To classify each of the proteins into a stable compartment, a support-vector-machine classifier with a radial kernel (Breckels et al. 2016) was used. Hyper-parameters *C* and *gamma* were selected via a grid-search approach using a 5-fold cross-validation iterated 100 times. The best *C* and *gamma* parameters were selected to classify the "unknown" proteome. Only classified proteins with an SVM-score > 0.7 were considered stable classification. To detect age-related changes in subcellular fractionation, a two-step approach was implemented. For each normalized protein profile, a principal component analysis was used to summarize the variance from the 10 fractions in each replicate and age group. After summarization, the first two principal component scores were used to perform a Hotelling T^2 test to detect changes in the multivariate protein profile mean. To estimate effect sizes, the median Euclidean distance between age groups was calculated for each protein profile (see Figure S1F).

Differential detergent extraction

A batch correction was applied to remove the effects of different batches of LC-MS/MS analysis using the limma::removeBatchEffect function from the limma package (Ritchie et al. 2015). Then, for each protein group, a detergent insolubility profile was generated by dividing the protein quantities from fractions F1:F3 by the quantity in the soluble (S) fraction, and log2 transformed. To detect significant changes in detergent insolubility profiles between age groups, a MANOVA test was applied to the detergent insolubility profiles using the standard function in the R programming language, and P-values were corrected for multiple testing using the FDR strategy. To estimate effect sizes, a detergent-insolubility-score (DIS) was calculated by summing the log2 transformed protein quantities in fractions F1:F3 relative to the S "soluble" fraction. For each age group and protein group, the median DIS between replicates was used to estimate the magnitude of changes in detergent insolubility: $\Delta DIS = DIS_{39wph} - DIS_{12wph}$. High values of ΔDIS indicate proteins that become more detergent resistant in the old (39 wph) samples (see Figure S2E).

Modified peptide abundance correction

For each enrichment, PTMs report tables were exported from Spectronaut. To correct the quantities of modified peptides for underlying changes in protein abundance across the age groups compared, correction factors were calculated using the aging proteome data. For each condition and protein group, the median protein quantity was calculated and then divided by the median protein quantity in the young (5 wph) age group. Each modified peptide was matched by protein identifier to the correction factor table. If a modified peptide was mapped to 2 or more proteins, the correction factor was calculated using the sum of the quantity of these proteins. Further, the correction was carried out by dividing peptide quantities by the mapped correction factors, and log2 transformed (see Figure S3). Differences in peptide quantities were statistically determined using the t-test moderated by the empirical Bayes method as implemented in the R package limma (Ritchie et al. 2015).

Kinase activity prediction from phosphoproteome data

Kinase activity prediction was calculated using the Kinase library (https://kinase-library.phosphosite.org/ea?a=de, (Johnson et al. 2023) using the differential expression-based analysis and default parameter.

GO enrichment analysis

Gene Set Enrichment Analysis (GSEA) was performed using the R package clusterProfiler (T. Wu et al. 2021), using the function gseGO. Briefly, *Nothobranchius furzeri* protein entries were mapped to the human gene name orthologues and given in input to the function to perform the enrichment. For GO term overrepresentation analysis (ORA), the topGO R package was used.

Identification of conserved PTMs sites

For the *Nothobranchius furzeri* proteins involved in neurodegenerative diseases (Figure 1J), a local alignment was performed with protein BLAST(v2.12.0+) (Altschul et al. 1990) with default parameters against the RefSeq human proteome (Taxon ID:9606). The top 10 hits from the BLAST search were retrieved, and each modified residue was mapped into the local alignment to identify the corresponding position in the human proteins. Each modified peptide was then considered conserved if at least one of the top 10 hits from the BLAST alignment had a corresponding residue in the modified amino acid position.

Calculation of protein-transcript decoupling and multiple linear regression

For aging brain proteome data and proteasome impairment samples, protein-transcript decoupling values were calculated as the difference in log2 fold changes between proteome and transcriptome. A null distribution was fitted on the decoupling values using the R package fdrtool (Strimmer 2008). Q-value < 0.1 was used as a threshold to reject the null hypothesis. The decoupling values from each protein-transcript pair were used as response variables in a multiple linear regression model. Predictors for the model were retrieved as follows: protein quantities were calculated as the median log2 protein quantity across all replicates from the proteomics DIA data. Protein quantities are estimated using the median peptide abundance as calculated by the Spectronaut software. mRNA abundance values were defined as the median log2(TPM) across all samples from the RNA-Seq aging dataset. Biophysical parameters were calculated for each protein with the R package Peptides. Protein half-life values were taken from mouse cortex data from (Fornasiero et al. 2018). The percentage of gene GC content was obtained from ENSEMBL Biomart (v108) (Cunningham et al. 2022), mapping ENSEMBL annotation against the *Nothobranchius furzeri* reference genome (Nfu_20150522, annotation nfurzeri_genebuild_v1.150922) using bedtools (Quinlan and Hall 2010). Multiple linear regression models were then performed using the `lm` base R function by keeping only complete and unique observations from the matrix generated. Features were scaled for each dataset, and a multiple linear regression model without intercept was fitted to the data.

Data integration

Log2 fold changes (for PTMs), ΔDIS (for detergent insolubility), or protein-transcript decoupling values were used as input for a GSEA analysis based on GO cellular component terms using the gseGO function from the clusterProfile (T. Wu et al. 2021) R package with the

following parameters minSize = 5 and maxSize = 400. For each GSEA, the normalized enrichment scores (NES) were taken and arranged in a matrix with different GO terms as rows and different datasets as columns. To visualize the relationship between the dataset, a principal component analysis was performed on the matrix. Missing GO terms in a given dataset were imputed as 0 values. The sum of the scores on the first two principal components was used to extract the most strongly affected GO terms from the combined integration of all the datasets.

Mitochondrial proteome composition

To calculate age-related changes in mitochondrial proteome composition (Figure 3H), raw DIA files coming from fraction 02 of the LOPIT-DC experiment were re-analyzed in Spectronaut (v16.2), using the same parameters as the other LOPIT-DC experiment. Fraction 02 represents the fraction where mitochondrial proteins are sedimenting in the LOPIT-DC experiment and, therefore, strongly enriched for mitochondrial proteins (Figure S1C-D). From the protein quantity matrix, mitochondrial proteins (according to Mitocarta3.0 annotation (Pagliarini et al. 2008)) were extracted, and their quantities log2 transformed and normalized by median centering. To detect changes in composition, a linear model on the log2 mitochondrial-centered values was implemented between the two age groups with the R package limma (Ritchie et al. 2015).

Ribo-seq data processing and analysis

Data processing and analysis was based on previously published protocol (Stein et al. 2022). Adapter sequences were removed from demultiplexed sequencing reads using Cutadapt v.1.4.2 (Martin 2011), followed by removal of the 5' nucleotide using FASTX-Trimmer. Reads mapping to ribosomal RNAs were removed using Bowtie v.1.3.1 (Langmead et al. 2009). Remaining reads were aligned to reference libraries that consisted of coding sequences containing 21 nucleotides flanking upstream of the start codon and downstream of the stop codon. To maximize unique mapping, a reference library was constructed using the longest transcripts for every 22757 genes. Bowtie alignment was performed using the following parameters: -y -a -m 1 -v 2 -norc -best -strata. A-site offset was estimated using riboWaltz (Lauria et al. 2018), and fragment lengths that do not exhibit 3-nucleotide periodicity were removed. Pause scores at each position were calculated by dividing the number of reads at each position by the average number of reads within the internal part of the transcript, excluding the first and last 20 codons. Positions with increased pausing during aging were identified following the previously published method (Stein et al. 2022). Briefly, for 6749 transcripts with sufficient coverage (>0.5 reads/codon and >64 reads/transcript) in all age groups, we used a two-tailed Fisher's exact test to compare each position (codon) between age groups to identify positions with statistically significant changes (Benjamini-Hochberg adjusted P-value < 0.05). These positions were further filtered to include positions with odds ratio greater than 1, pause score of the older sample greater than the pause score of younger sample, reads in the oldest sample greater than the average number of reads across the transcript, and a position in the internal part of the transcript to only select sites with high-confidence age-dependent changes in pausing. To visualize amino acids enriched in age-dependent pausing sites, we used the weighted Kullback Leibler method (Thomsen and Nielsen 2012) using the frequency of each amino acid in coding sequences as background. For metagene analysis around age-dependent pausing sites, reads were first aligned to these sites and normalized by dividing reads at each codon by the average reads per codon within

the analysis window to control for differences in expression and coverage. Mean and bootstrapped 95% confidence intervals of these normalized values were plotted. Only positions with sufficient coverage (reads/codon>0.5) in the analysis window were included. To identify sites with disome formation, we first identified sites with strong pausing in the old sample (pause score >6). Then, we calculated the average ribosome density of two regions for young and old samples; 1) analysis window (40 codons up/downstream from strong pause site) and 2) between 8 and 12 codons upstream from strong pause site (approximate position of trailing ribosome). Sites with higher ribosome density in 2) were identified as disome sites, and disomes sites unique to old samples were plotted. For comparisons to proteomics data sets, we included all sites with statistically significant changes (Benjamini-Hochberg adjusted P-value < 0.05) and used log2 of pause score ratio (Old/Young). For translation efficiency analysis, RNA-seq data was re-aligned to the same reference library used for Ribo-seq to compare transcript abundance. Changes in translation efficiency were calculated using DESeq2 (Love, Huber, and Anders 2014), using the following design ~assay + condition + assay:condition, where assay indicates the different counts from RNA-Seq and Ribo-Seq respectively, and condition indicated the different age groups.

Estimates of mRNA half-life variations

Exonic coordinates of protein-coding genes were extracted from the annotation nfurzeri_genebuild_v1.150922. Exonic and intronic read counts were obtained following the procedure suggested by (Gaidatzis et al. 2016). To this end, exonic coordinates were flanked on both sides by 10 nt and were grouped by gene. Intronic coordinates were obtained by subtracting the exonic coordinates from the gene-wise coordinates. For each gene, exonic and intronic read counts were obtained using the htseq-count function from HTSeq v2.0.2 (Putri et al. 2022) with the parameter -m set to intersection-strict to consider only reads that strictly fall within an exon or an intron. Additionally, in each sample, genes with less than 10 reads on both exons and introns were ignored (read counts set as missing values) in order to be robust against noisy estimates based on low read counts. Lastly, the log-transformed exonic-to-intronic read count ratio r was computed for each gene and sample as:

$$r = Log_2(exonic\ counts + 1) - Log_2(intronic\ counts + 1)$$

Gene-specific biases such as exonic and intronic lengths and GC content can affect exonic and intronic read counts. These biases cancel out when ratios between samples are considered, as they are typically multiplicative (Gaidatzis et al. 2016). The ratio between mRNA half-life in sample s_1 and sample s_2 is then estimated as:

$$Log_2\left(\frac{mRNA\ halflife\ s_1}{mRNA\ halflife\ s_2}\right) = \frac{r_1}{r_2}$$

Estimates of protein synthesis rate

To estimate k_i, 5'-UTRs sequences were retrieved from the *Nothobranchius furzeri* reference genome (Nfu_20150522, annotation nfurzeri_genebuild_v1.150922). The masked FASTA genome sequences were parsed using bedtools (Quinlan and Hall 2010). The translation starting codon "ATG" was identified from the `CDS` features from the GFF file. The region around the starting codon was extracted with +6 nucleotide upstream and +4 nucleotide downstream to match the pattern "NNNNNNATGNN". Only valid sequences (without

ambiguous nucleotides) with an ATG starting codon in the correct position were retained. 91% of the transcript annotated in the GFF file had a valid translation initiation region as described above. The k_i was then estimated using the dinucleotide position weight matrix from (Noderer et al. 2014). In case a single transcript had multiple starting sites, the k_i values were summarized by taking the median value. This led to the estimate of k_i for 59129 transcripts. Estimated protein synthesis rates were calculated as in (Mills and Green 2017; Khajuria et al. 2018). More in detail, the authors described the estimated synthesis rate as:

$$Q = mRk_i\,[1 - (L / ((k_e / (k_i R)) + (L - 1)))]$$

where Q refers to the estimated synthesis rate, m refers to individual mRNA expression level obtained from the median across sample log2(TPM) from RNA-Seq data and normalized between 0 and 1, R represents the total amount of available ribosomes, k_i indicates an mRNA-specific translation initiation rate as computed above and normalized between 0 and 1, L is the number of codons occupied by one ribosome, set to 10 (based on the average length of a ribosome footprint), and k_e is the termination rates arbitrarily set to 1. Estimated synthesis rates were then computed for different values of R ranging from 1.3 to 0.

Declaration of generative AI and AI-assisted technologies in the writing process: During the preparation of this work the author(s) used Chat GPT (v3.5) in order to improve readability of the manuscript. After using this tool/service, the author(s) reviewed and edited the content as needed and take(s) full responsibility for the content of the publication.

References

Alfonso, S. I., J. A. Callender, B. Hooli, C. E. Antal, K. Mullin, M. A. Sherman, S. E. Lesné, et al. 2016. “Gain-of-Function Mutations in Protein Kinase Cα (PKCα) May Promote Synaptic Defects in Alzheimer’s Disease.” *Science Signaling* 9 (427). https://doi.org/10.1126/scisignal.aaf6209.

Altschul, S. F., W. Gish, W. Miller, E. W. Myers, and D. J. Lipman. 1990. “Basic Local Alignment Search Tool.” *Journal of Molecular Biology* 215 (3): 403–10.

Aman, Yahyah, Tomas Schmauck-Medina, Malene Hansen, Richard I. Morimoto, Anna Katharina Simon, Ivana Bjedov, Konstantinos Palikaras, et al. 2021. “Autophagy in Healthy Aging and Disease.” *Nature Aging* 1 (8): 634–50.

Anisimova, A. S., M. B. Meerson, M. V. Gerashchenko, I. V. Kulakovskiy, S. E. Dmitriev, and V. N. Gladyshev. 2020. “Multifaceted Deregulation of Gene Expression and Protein Synthesis with Age.” *Proceedings of the National Academy of Sciences of the United States of America* 117 (27). https://doi.org/10.1073/pnas.2001788117.

Araujo, Mariana E. G. de, Gudrun Liebscher, Michael W. Hess, and Lukas A. Huber. 2020. “Lysosomal Size Matters.” *Traffic* 21 (1): 60–75.

Arthur, Laura, Slavica Pavlovic-Djuranovic, Kristin Smith-Koutmou, Rachel Green, Pawel Szczesny, and Sergej Djuranovic. 2015. “Translational Control by Lysine-Encoding A-Rich Sequences.” *Science Advances* 1 (6). https://doi.org/10.1126/sciadv.1500154.

Aviner, Ranen, Ting-Ting Lee, Vincent B. Masto, Dan Gestaut, Kathy H. Li, Raul Andino, and Judith Frydman. 2022. “Ribotoxic Collisions on CAG Expansions Disrupt Proteostasis and Stress Responses in Huntington’s Disease.” *bioRxiv*. https://doi.org/10.1101/2022.05.04.490528.

Bagnoli, Sara, Eva Terzibasi Tozzini, and Alessandro Cellerino. 2023. “Immunofluorescence and Aggresome Staining of Nothobranchius Furzeri Cryosections.” *Cold Spring Harbor Protocols*, March. https://doi.org/10.1101/pdb.prot107791.

Bagnoli, S., B. Fronte, C. Bibbiani, Tozzini E. Terzibasi, and A. Cellerino. 2022. “Quantification of Noradrenergic-, Dopaminergic-, and Tectal-Neurons during Aging in the Short-Lived Killifish Nothobranchius Furzeri.” *Aging Cell* 21 (9). https://doi.org/10.1111/acel.13689.

Bai, Bing, Xusheng Wang, Yuxin Li, Ping-Chung Chen, Kaiwen Yu, Kaushik Kumar Dey, Jay M. Yarbro, et al. 2020. “Deep Multilayer Brain Proteomics Identifies Molecular Networks in Alzheimer’s Disease Progression.” *Neuron* 106 (4): 700.

Baumgart, Mario, Steffen Priebe, Marco Groth, Nils Hartmann, Uwe Menzel, Luca Pandolfini, Philipp Koch, et al. 2016. “Longitudinal RNA-Seq Analysis of Vertebrate Aging Identifies Mitochondrial Complex I as a Small-Molecule-Sensitive Modifier of Lifespan.” *Cell Systems* 2 (2): 122–32.

Bazzini, Ariel A., Florencia Del Viso, Miguel A. Moreno-Mateos, Timothy G. Johnstone, Charles E. Vejnar, Yidan Qin, Jun Yao, Mustafa K. Khokha, and Antonio J. Giraldez. 2016. “Codon Identity Regulates mRNA Stability and Translation Efficiency during the Maternal-to-Zygotic Transition.” *The EMBO Journal* 35 (19): 2087–2103.

Bentley, David R., Shankar Balasubramanian, Harold P. Swerdlow, Geoffrey P. Smith, John Milton, Clive G. Brown, Kevin P. Hall, et al. 2008. “Accurate Whole Human Genome Sequencing Using Reversible Terminator Chemistry.” *Nature* 456 (7218): 53–59.

Bhadra, Malini, Porsha Howell, Sneha Dutta, Caroline Heintz, and William B. Mair. 2020. “Alternative Splicing in Aging and Longevity.” *Human Genetics* 139 (3): 357–69.

Bozukova, Mihaela, Chrysa Nikopoulou, Niklas Kleinenkuhnen, Dora Grbavac, Katrin Goetsch, and Peter Tessarz. 2022. “Aging Is Associated with Increased Chromatin Accessibility and Reduced Polymerase Pausing in Liver.” *Molecular Systems Biology* 18 (9): e11002.

Braeckman, Bart P., Koen Houthoofd, and Jacques R. Vanfleteren. 2002. “Assessing Metabolic Activity in Aging Caenorhabditis Elegans: Concepts and Controversies.” *Aging Cell* 1 (2): 82–88; discussion 102–3.

1767 Breckels, Lisa M., Claire M. Mulvey, Kathryn S. Lilley, and Laurent Gatto. 2016. “A
1768 Bioconductor Workflow for Processing and Analysing Spatial Proteomics Data.”
1769 *F1000Research* 5 (December): 2926.
1770 Buczak, Katarzyna, Joanna M. Kirkpatrick, Felicia Truckenmueller, Deolinda Santinha, Lino
1771 Ferreira, Stephanie Roessler, Stephan Singer, Martin Beck, and Alessandro Ori. 2020.
1772 “Spatially Resolved Analysis of FFPE Tissue Proteomes by Quantitative Mass
1773 Spectrometry.” *Nature Protocols* 15 (9): 2956–79.
1774 Caudron-Herger, Maiwen, Ralf E. Jansen, Elsa Wassmer, and Sven Diederichs. 2021.
1775 “RBP2GO: A Comprehensive Pan-Species Database on RNA-Binding Proteins, Their
1776 Interactions and Functions.” *Nucleic Acids Research* 49 (D1): D425–36.
1777 Chan, Leon Y., Christopher F. Mugler, Stephanie Heinrich, Pascal Vallotton, and Karsten
1778 Weis. 2018. “Non-Invasive Measurement of mRNA Decay Reveals Translation Initiation
1779 as the Major Determinant of mRNA Stability.” *eLife* 7 (September).
1780 https://doi.org/10.7554/eLife.32536.
1781 Chatterjee, Shreyasi, Megan Sealey, Eva Ruiz, Chrysia M. Pegasiou, Keeley Brookes, Sam
1782 Green, Anna Crisford, et al. 2023. “Age-Related Changes in Tau and Autophagy in
1783 Human Brain in the Absence of Neurodegeneration.” *PloS One* 18 (1): e0262792.
1784 Crook, Oliver M., Lisa M. Breckels, Kathryn S. Lilley, Paul D. W. Kirk, and Laurent Gatto.
1785 2019. “A Bioconductor Workflow for the Bayesian Analysis of Spatial Proteomics.”
1786 *F1000Research* 8 (April): 446.
1787 Cunningham, Fiona, James E. Allen, Jamie Allen, Jorge Alvarez-Jarreta, M. Ridwan Amode,
1788 Irina M. Armean, Olanrewaju Austine-Orimoloye, et al. 2022. “Ensembl 2022.” *Nucleic
1789 Acids Research* 50 (D1): D988–95.
1790 Datta, Dibyadeep, Shannon N. Leslie, Min Wang, Yury M. Morozov, Shengtao Yang,
1791 Sueann Mentone, Caroline Zeiss, et al. 2021. “Age-Related Calcium Dysregulation
1792 Linked with Tau Pathology and Impaired Cognition in Non-Human Primates.”
1793 *Alzheimer’s & Dementia: The Journal of the Alzheimer's Association* 17 (6): 920–32.
1794 David, Della C., Noah Ollikainen, Jonathan C. Trinidad, Michael P. Cary, Alma L.
1795 Burlingame, and Cynthia Kenyon. 2010. “Widespread Protein Aggregation as an
1796 Inherent Part of Aging in C. Elegans.” *PLoS Biology* 8 (8): e1000450.
1797 Debès, Cédric, Antonios Papadakis, Sebastian Grönke, Özlem Karalay, Luke S. Tain,
1798 Athanasia Mizi, Shuhei Nakamura, et al. 2023. “Ageing-Associated Changes in
1799 Transcriptional Elongation Influence Longevity.” *Nature* 616 (7958): 814–21.
1800 Dick, F., O. B. Tysnes, G. W. Alves, G. S. Nido, and C. Tzoulis. 2023. “Altered
1801 Transcriptome-Proteome Coupling Indicates Aberrant Proteostasis in Parkinson’s
1802 Disease.” *iScience* 26 (2). https://doi.org/10.1016/j.isci.2023.105925.
1803 Dobin, Alexander, Carrie A. Davis, Felix Schlesinger, Jorg Drenkow, Chris Zaleski, Sonali
1804 Jha, Philippe Batut, Mark Chaisson, and Thomas R. Gingeras. 2012. “STAR: Ultrafast
1805 Universal RNA-Seq Aligner.” *Bioinformatics* 29 (1): 15–21.
1806 Espada, Lilia, Alexander Dakhovnik, Prerana Chaudhari, Asya Martirosyan, Laura Miek,
1807 Tetiana Poliezhaieva, Yvonne Schaub, et al. 2020. “Loss of Metabolic Plasticity
1808 Underlies Metformin Toxicity in Aged Caenorhabditis Elegans.” *Nature Metabolism* 2
1809 (11): 1316–31.
1810 Fornasiero, Eugenio F., Sunit Mandad, Hanna Wildhagen, Mihai Alevra, Burkhard Rammner,
1811 Sarva Keihani, Felipe Opazo, et al. 2018. “Precisely Measured Protein Lifetimes in the
1812 Mouse Brain Reveal Differences across Tissues and Subcellular Fractions.” *Nature
1813 Communications* 9 (1): 1–17.
1814 Gaidatzis, Dimos, Lukas Burger, Maria Florescu, and Michael B. Stadler. 2016. “Erratum:
1815 Analysis of Intronic and Exonic Reads in RNA-Seq Data Characterizes Transcriptional
1816 and Post-Transcriptional Regulation.” *Nature Biotechnology* 34 (2): 210.
1817 Gatto, Laurent, Lisa M. Breckels, and Kathryn S. Lilley. 2019. “Assessing Sub-Cellular
1818 Resolution in Spatial Proteomics Experiments.” *Current Opinion in Chemical Biology* 48
1819 (February): 123–49.
1820 Geladaki, Aikaterini, Nina Kočevar Britovšek, Lisa M. Breckels, Tom S. Smith, Owen L.
1821 Vennard, Claire M. Mulvey, Oliver M. Crook, Laurent Gatto, and Kathryn S. Lilley. 2019.

"Combining LOPIT with Differential Ultracentrifugation for High-Resolution Spatial Proteomics." *Nature Communications*. https://doi.org/10.1038/s41467-018-08191-w.

Gerdes Gyuricza, Isabela, Joel M. Chick, Gregory R. Keele, Andrew G. Deighan, Steven C. Munger, Ron Korstanje, Steven P. Gygi, and Gary A. Churchill. 2022. "Genome-Wide Transcript and Protein Analysis Highlights the Role of Protein Homeostasis in the Aging Mouse Heart." *Genome Research* 32 (5): 838–52.

Gkotsi, Despoina, Rana Begum, Thomas Salt, Gerassimos Lascaratos, Chris Hogg, Kai-Yin Chau, Anthony H. V. Schapira, and Glen Jeffery. 2014. "Recharging Mitochondrial Batteries in Old Eyes. Near Infra-Red Increases ATP." *Experimental Eye Research* 122 (May): 50–53.

Gonskikh, Yulia, and Norbert Polacek. 2017. "Alterations of the Translation Apparatus during Aging and Stress Response." *Mechanisms of Ageing and Development* 168 (December): 30–36.

Gray, D. A., M. Tsirigotis, and J. Woulfe. 2003. "Ubiquitin, Proteasomes, and the Aging Brain." *Science of Aging Knowledge Environment: SAGE KE* 2003 (34). https://doi.org/10.1126/sageke.2003.34.re6.

Guillozet, Angela L., Sandra Weintraub, Deborah C. Mash, and M. Marsel Mesulam. 2003. "Neurofibrillary Tangles, Amyloid, and Memory in Aging and Mild Cognitive Impairment." *Archives of Neurology* 60 (5): 729–36.

Gyenis, Akos, Jiang Chang, Joris J. P. G. Demmers, Serena T. Bruens, Sander Barnhoorn, Renata M. C. Brandt, Marjolein P. Baar, et al. 2023. "Genome-Wide RNA Polymerase Stalling Shapes the Transcriptome during Aging." *Nature Genetics* 55 (2): 268–79.

Hansen, Malene, David C. Rubinsztein, and David W. Walker. 2018. "Autophagy as a Promoter of Longevity: Insights from Model Organisms." *Nature Reviews. Molecular Cell Biology* 19 (9): 579–93.

Harel, Itamar, Yiwen R. Chen, Inbal Ziv, Param Priya Singh, Paloma Navarro Negredo, Uri Goshtchevsky, Wei Wang, et al. 2022. "Identification of Protein Aggregates in the Aging Vertebrate Brain with Prion-like and Phase Separation Properties." *bioRxiv*. https://doi.org/10.1101/2022.02.26.482115.

Heiby, Julia C., and Alessandro Ori. 2022. "Organelle Dysfunction and Its Contribution to Metabolic Impairments in Aging and Age-Related Diseases." *Current Opinion in Systems Biology* 30 (June): 100416.

Higgins, Reneé, Joshua M. Gendron, Lisa Rising, Raymond Mak, Kristofor Webb, Stephen E. Kaiser, Nathan Zuzow, et al. 2015. "The Unfolded Protein Response Triggers Site-Specific Regulatory Ubiquitylation of 40S Ribosomal Proteins." *Molecular Cell* 59 (1): 35–49.

Hipp, Mark S., Prasad Kasturi, and F. Ulrich Hartl. 2019. "The Proteostasis Network and Its Decline in Ageing." *Nature Reviews. Molecular Cell Biology* 20 (7): 421–35.

Ingram, Thomas, and Lisa Chakrabarti. 2016. "Proteomic Profiling of Mitochondria: What Does It Tell Us about the Ageing Brain?" *Aging* 8 (12): 3161–79.

Iordanov, M. S., D. Pribnow, J. L. Magun, T. H. Dinh, J. A. Pearson, S. L. Chen, and B. E. Magun. 1997. "Ribotoxic Stress Response: Activation of the Stress-Activated Protein Kinase JNK1 by Inhibitors of the Peptidyl Transferase Reaction and by Sequence-Specific RNA Damage to the Alpha-Sarcin/ricin Loop in the 28S rRNA." *Molecular and Cellular Biology* 17 (6): 3373–81.

Janssens, Georges E., Anne C. Meinema, Javier González, Justina C. Wolters, Alexander Schmidt, Victor Guryev, Rainer Bischoff, Ernst C. Wit, Liesbeth M. Veenhoff, and Matthias Heinemann. 2015. "Protein Biogenesis Machinery Is a Driver of Replicative Aging in Yeast." *eLife* 4 (December): e08527.

Johnson, J. L., T. M. Yaron, E. M. Huntsman, A. Kerelsky, J. Song, A. Regev, T. Y. Lin, et al. 2023. "An Atlas of Substrate Specificities for the Human Serine/threonine Kinome." *Nature* 613 (7945). https://doi.org/10.1038/s41586-022-05575-3.

Kelmer Sacramento, Erika, Joanna M. Kirkpatrick, Mariateresa Mazzetto, Mario Baumgart, Aleksandar Bartolome, Simone Di Sanzo, Cinzia Caterino, et al. 2020. "Reduced Proteasome Activity in the Aging Brain Results in Ribosome Stoichiometry Loss and

Aggregation." *Molecular Systems Biology* 16 (6): e9596.
Khajuria, Rajiv K., Mathias Munschauer, Jacob C. Ulirsch, Claudia Fiorini, Leif S. Ludwig, Sean K. McFarland, Nour J. Abdulhay, et al. 2018. "Ribosome Levels Selectively Regulate Translation and Lineage Commitment in Human Hematopoiesis." *Cell* 173 (1): 90–103.e19.
Kluever, Verena, Belisa Russo, Sunit Mandad, Nisha Hemandhar Kumar, Mihai Alevra, Alessandro Ori, Silvio O. Rizzoli, Henning Urlaub, Anja Schneider, and Eugenio F. Fornasiero. 2022. "Protein Lifetimes in Aged Brains Reveal a Proteostatic Adaptation Linking Physiological Aging to Neurodegeneration." *Science Advances* 8 (20): eabn4437.
Koyuncu, Seda, Rute Loureiro, Hyun Ju Lee, Prerana Wagle, Marcus Krueger, and David Vilchez. 2021. "Rewiring of the Ubiquitinated Proteome Determines Ageing in C. Elegans." *Nature* 596 (7871): 285–90.
Labbadia, J., and R. I. Morimoto. 2015. "The Biology of Proteostasis in Aging and Disease." *Annual Review of Biochemistry*. https://www.annualreviews.org/doi/abs/10.1146/annurev-biochem-060614-033955.
Labbadia, Johnathan, and Richard I. Morimoto. 2015. "Repression of the Heat Shock Response Is a Programmed Event at the Onset of Reproduction." *Molecular Cell* 59 (4): 639–50.
Langmead, Ben, Cole Trapnell, Mihai Pop, and Steven L. Salzberg. 2009. "Ultrafast and Memory-Efficient Alignment of Short DNA Sequences to the Human Genome." *Genome Biology* 10 (3): R25.
Lauria, Fabio, Toma Tebaldi, Paola Bernabò, Ewout J. N. Groen, Thomas H. Gillingwater, and Gabriella Viero. 2018. "riboWaltz: Optimization of Ribosome P-Site Positioning in Ribosome Profiling Data." *PLoS Computational Biology* 14 (8): e1006169.
Liao, Yang, Gordon K. Smyth, and Wei Shi. 2013. "featureCounts: An Efficient General Purpose Program for Assigning Sequence Reads to Genomic Features." *Bioinformatics* 30 (7): 923–30.
Li, Longfei, Yanli Jiang, Jian-Zhi Wang, Rong Liu, and Xiaochuan Wang. 2022. "Tau Ubiquitination in Alzheimer's Disease." *Frontiers in Neurology* 12 (February). https://doi.org/10.3389/fneur.2021.786353.
Li, S., Z. Wu, I. Tantray, Y. Li, S. Chen, J. Dong, S. Glynn, H. Vogel, M. Snyder, and B. Lu. 2020. "Quality-Control Mechanisms Targeting Translationally Stalled and C-Terminally Extended poly(GR) Associated with ALS/FTD." *Proceedings of the National Academy of Sciences of the United States of America* 117 (40). https://doi.org/10.1073/pnas.2005506117.
López-Otín, Carlos, Maria A. Blasco, Linda Partridge, Manuel Serrano, and Guido Kroemer. 2023. "Hallmarks of Aging: An Expanding Universe." *Cell* 186 (2): 243–78.
Louka, A., S. Bagnoli, J. Rupert, B. Esapa, G. G. Tartaglia, A. Cellerino, A. Pastore, and Tozzini E. Terzibasi. 2022. "New Lessons on TDP-43 from Old N. Furzeri Killifish." *Aging Cell* 21 (1). https://doi.org/10.1111/acel.13517.
Love, Michael I., Wolfgang Huber, and Simon Anders. 2014. "Moderated Estimation of Fold Change and Dispersion for RNA-Seq Data with DESeq2." *Genome Biology* 15 (12): 550.
Martin, Marcel. 2011. "Cutadapt Removes Adapter Sequences from High-Throughput Sequencing Reads." *EMBnet.journal* 17 (1): 10.
Matsui, Hideaki, Naoya Kenmochi, and Kazuhiko Namikawa. 2019. "Age- and α-Synuclein-Dependent Degeneration of Dopamine and Noradrenaline Neurons in the Annual Killifish Nothobranchius Furzeri." *Cell Reports* 26 (7): 1727–33.e6.
McGlincy, Nicholas J., and Nicholas T. Ingolia. 2017. "Transcriptome-Wide Measurement of Translation by Ribosome Profiling." *Methods* 126 (August): 112–29.
Meyer, Cindy, Aitor Garzia, Pavel Morozov, Henrik Molina, and Thomas Tuschl. 2020. "The G3BP1-Family-USP10 Deubiquitinase Complex Rescues Ubiquitinated 40S Subunits of Ribosomes Stalled in Translation from Lysosomal Degradation." *Molecular Cell* 77 (6): 1193–1205.e5.

Mills, Eric W., and Rachel Green. 2017. “Ribosomopathies: There’s Strength in Numbers.” *Science* 358 (6363). https://doi.org/10.1126/science.aan2755.

Miyoshi, Noriyuki, Hammou Oubrahim, P. Boon Chock, and Earl R. Stadtman. 2006. “Age-Dependent Cell Death and the Role of ATP in Hydrogen Peroxide-Induced Apoptosis and Necrosis.” *Proceedings of the National Academy of Sciences of the United States of America* 103 (6): 1727–31.

Morshed, Nader, Meelim J. Lee, Felicia H. Rodriguez, Douglas A. Lauffenburger, Diego Mastroeni, and Forest M. White. 2021. “Quantitative Phosphoproteomics Uncovers Dysregulated Kinase Networks in Alzheimer’s Disease.” *Nature Aging* 1 (6): 550–65.

Noderer, William L., Ross J. Flockhart, Aparna Bhaduri, Alexander J. Diaz de Arce, Jiajing Zhang, Paul A. Khavari, and Clifford L. Wang. 2014. “Quantitative Analysis of Mammalian Translation Initiation Sites by FACS-Seq.” *Molecular Systems Biology* 10 (8): 748.

Ori, Alessandro, Brandon H. Toyama, Michael S. Harris, Thomas Bock, Murat Iskar, Peer Bork, Nicholas T. Ingolia, Martin W. Hetzer, and Martin Beck. 2015. “Integrated Transcriptome and Proteome Analyses Reveal Organ-Specific Proteome Deterioration in Old Rats.” *Cell Systems* 1 (3): 224–37.

Pagliarini, David J., Sarah E. Calvo, Betty Chang, Sunil A. Sheth, Scott B. Vafai, Shao-En Ong, Geoffrey A. Walford, et al. 2008. “A Mitochondrial Protein Compendium Elucidates Complex I Disease Biology.” *Cell* 134 (1): 112–23.

Putri, Givanna H., Simon Anders, Paul Theodor Pyl, John E. Pimanda, and Fabio Zanini. 2022. “Analysing High-Throughput Sequencing Data in Python with HTSeq 2.0.” *Bioinformatics* 38 (10): 2943–45.

Quinlan, Aaron R., and Ira M. Hall. 2010. “BEDTools: A Flexible Suite of Utilities for Comparing Genomic Features.” *Bioinformatics* 26 (6): 841–42.

Rimal, S., Y. Li, R. Vartak, J. Geng, I. Tantray, S. Li, S. Huh, et al. 2021. “Inefficient Quality Control of Ribosome Stalling during APP Synthesis Generates CAT-Tailed Species That Precipitate Hallmarks of Alzheimer’s Disease.” *Acta Neuropathologica Communications* 9 (1). https://doi.org/10.1186/s40478-021-01268-6.

Ritchie, Matthew E., Belinda Phipson, Di Wu, Yifang Hu, Charity W. Law, Wei Shi, and Gordon K. Smyth. 2015. “Limma Powers Differential Expression Analyses for RNA-Sequencing and Microarray Studies.” *Nucleic Acids Research* 43 (7): e47.

Safaiyan, Shima, Nirmal Kannaiyan, Nicolas Snaidero, Simone Brioschi, Knut Biber, Simon Yona, Aimee L. Edinger, Steffen Jung, Moritz J. Rossner, and Mikael Simons. 2016. “Age-Related Myelin Degradation Burdens the Clearance Function of Microglia during Aging.” *Nature Neuroscience* 19 (8): 995–98.

Schumacher, Björn, Joris Pothof, Jan Vijg, and Jan H. J. Hoeijmakers. 2021. “The Central Role of DNA Damage in the Ageing Process.” *Nature* 592 (7856): 695–703.

Schwartz, D. C., and R. Parker. 2000. “mRNA Decapping in Yeast Requires Dissociation of the Cap Binding Protein, Eukaryotic Translation Initiation Factor 4E.” *Molecular and Cellular Biology* 20 (21): 7933–42.

Sharma, Ajeet K., Johannes Venezian, Ayala Shiber, Günter Kramer, Bernd Bukau, and Edward P. O’Brien. 2021. “Combinations of Slow-Translating Codon Clusters Can Increase mRNA Half-Life in.” *Proceedings of the National Academy of Sciences of the United States of America* 118 (51). https://doi.org/10.1073/pnas.2026362118.

Silva, Pedro Tomaz da, Yujie Zhang, Evangelos Theodorakis, Laura D. Martens, Vicente A. Yépez, Vicent Pelechano, and Julien Gagneur. 2023. “Cellular Energy Regulates mRNA Translation and Degradation in a Codon-Specific Manner.” *bioRxiv*. https://doi.org/10.1101/2023.04.06.535836.

Smith, Tom, Andreas Heger, and Ian Sudbery. 2017. “UMI-Tools: Modeling Sequencing Errors in Unique Molecular Identifiers to Improve Quantification Accuracy.” *Genome Research* 27 (3): 491–99.

Stagi, Massimiliano, Zoe A. Klein, Travis J. Gould, Joerg Bewersdorf, and Stephen M. Strittmatter. 2014. “Lysosome Size, Motility and Stress Response Regulated by Fronto-Temporal Dementia Modifier TMEM106B.” *Molecular and Cellular Neurosciences* 61

(July): 226–40.
Stein, Kevin C., Fabián Morales-Polanco, Joris van der Lienden, T. Kelly Rainbolt, and Judith Frydman. 2022. “Ageing Exacerbates Ribosome Pausing to Disrupt Cotranslational Proteostasis.” *Nature* 601 (7894): 637–42.
Stoeger, Thomas, Rogan A. Grant, Alexandra C. McQuattie-Pimentel, Kishore R. Anekalla, Sophia S. Liu, Heliodoro Tejedor-Navarro, Benjamin D. Singer, et al. 2022. “Aging Is Associated with a Systemic Length-Associated Transcriptome Imbalance.” *Nature Aging* 2 (12): 1191–1206.
Strimmer, Korbinian. 2008. “Fdrtool: A Versatile R Package for Estimating Local and Tail Area-Based False Discovery Rates.” *Bioinformatics* 24 (12): 1461–62.
Sudmant, Peter H., Hyeseung Lee, Daniel Dominguez, Myriam Heiman, and Christopher B. Burge. 2018. “Widespread Accumulation of Ribosome-Associated Isolated 3’ UTRs in Neuronal Cell Populations of the Aging Brain.” *Cell Reports* 25 (9): 2447–56.e4.
Takemon, Yuka, Joel M. Chick, Isabela Gerdes Gyuricza, Daniel A. Skelly, Olivier Devuyst, Steven P. Gygi, Gary A. Churchill, and Ron Korstanje. 2021. “Proteomic and Transcriptomic Profiling Reveal Different Aspects of Aging in the Kidney.” *eLife* 10 (March). https://doi.org/10.7554/eLife.62585.
Tebbenkamp, Andrew T. N., and David R. Borchelt. 2009. “Protein Aggregate Characterization in Models of Neurodegenerative Disease.” *Neuroproteomics*, 85–91.
Thomsen, Martin Christen Frølund, and Morten Nielsen. 2012. “Seq2Logo: A Method for Construction and Visualization of Amino Acid Binding Motifs and Sequence Profiles Including Sequence Weighting, Pseudo Counts and Two-Sided Representation of Amino Acid Enrichment and Depletion.” *Nucleic Acids Research* 40 (Web Server issue): W281–87.
Tyshkovskiy, Alexander, Siming Ma, Anastasia V. Shindyapina, Stanislav Tikhonov, Sang-Goo Lee, Perinur Bozaykut, José P. Castro, et al. 2023. “Distinct Longevity Mechanisms across and within Species and Their Association with Aging.” *Cell* 186 (13): 2929–49.e20.
Valenzano, Dario R., Eva Terzibasi, Antonino Cattaneo, Luciano Domenici, and Alessandro Cellerino. 2006. “Temperature Affects Longevity and Age-Related Locomotor and Cognitive Decay in the Short-Lived Fish Nothobranchius Furzeri.” *Aging Cell* 5 (3): 275–78.
Vecchi, Giulia, Pietro Sormanni, Benedetta Mannini, Andrea Vandelli, Gian Gaetano Tartaglia, Christopher M. Dobson, F. Ulrich Hartl, and Michele Vendruscolo. 2020. “Proteome-Wide Observation of the Phenomenon of Life on the Edge of Solubility.” *Proceedings of the National Academy of Sciences of the United States of America* 117 (2): 1015–20.
Vilchez, David, Isabel Saez, and Andrew Dillin. 2014. “The Role of Protein Clearance Mechanisms in Organismal Ageing and Age-Related Diseases.” *Nature Communications* 5 (December): 5659.
Walther, D. M., P. Kasturi, M. Zheng, S. Pinkert, G. Vecchi, P. Ciryam, R. I. Morimoto, et al. 2015. “Widespread Proteome Remodeling and Aggregation in Aging C. Elegans.” *Cell* 161 (4). https://doi.org/10.1016/j.cell.2015.03.032.
Wang, Yipeng, and Eckhard Mandelkow. 2015. “Tau in Physiology and Pathology.” *Nature Reviews. Neuroscience* 17 (1): 22–35.
Wei, Yu-Ning, Hai-Yang Hu, Gang-Cai Xie, Ning Fu, Zhi-Bin Ning, Rong Zeng, and Philipp Khaitovich. 2015. “Transcript and Protein Expression Decoupling Reveals RNA Binding Proteins and miRNAs as Potential Modulators of Human Aging.” *Genome Biology* 16 (1): 41.
Wu, Tianzhi, Erqiang Hu, Shuangbin Xu, Meijun Chen, Pingfan Guo, Zehan Dai, Tingze Feng, et al. 2021. “clusterProfiler 4.0: A Universal Enrichment Tool for Interpreting Omics Data.” *Innovation (Cambridge (Mass.))* 2 (3): 100141.
Wu, Z., I. Tantray, J. Lim, S. Chen, Y. Li, Z. Davis, C. Sitron, et al. 2019. “MISTERMINATE Mechanistically Links Mitochondrial Dysfunction with Proteostasis Failure.” *Molecular Cell* 75 (4). https://doi.org/10.1016/j.molcel.2019.06.031.

Ximerakis, M., S. L. Lipnick, B. T. Innes, S. K. Simmons, X. Adiconis, D. Dionne, B. A. Mayweather, et al. 2019. “Single-Cell Transcriptomic Profiling of the Aging Mouse Brain.” *Nature Neuroscience* 22 (10). https://doi.org/10.1038/s41593-019-0491-3.

Yan, Liewei L., Carrie L. Simms, Fionn McLoughlin, Richard D. Vierstra, and Hani S. Zaher. 2019. “Oxidation and Alkylation Stresses Activate Ribosome-Quality Control.” *Nature Communications* 10 (1): 5611.

Yu, Qing, Haopeng Xiao, Mark P. Jedrychowski, Devin K. Schweppe, Jose Navarrete-Perea, Jeffrey Knott, John Rogers, Edward T. Chouchani, and Steven P. Gygi. 2020. “Sample Multiplexing for Targeted Pathway Proteomics in Aging Mice.” *Proceedings of the National Academy of Sciences of the United States of America* 117 (18): 9723–32.

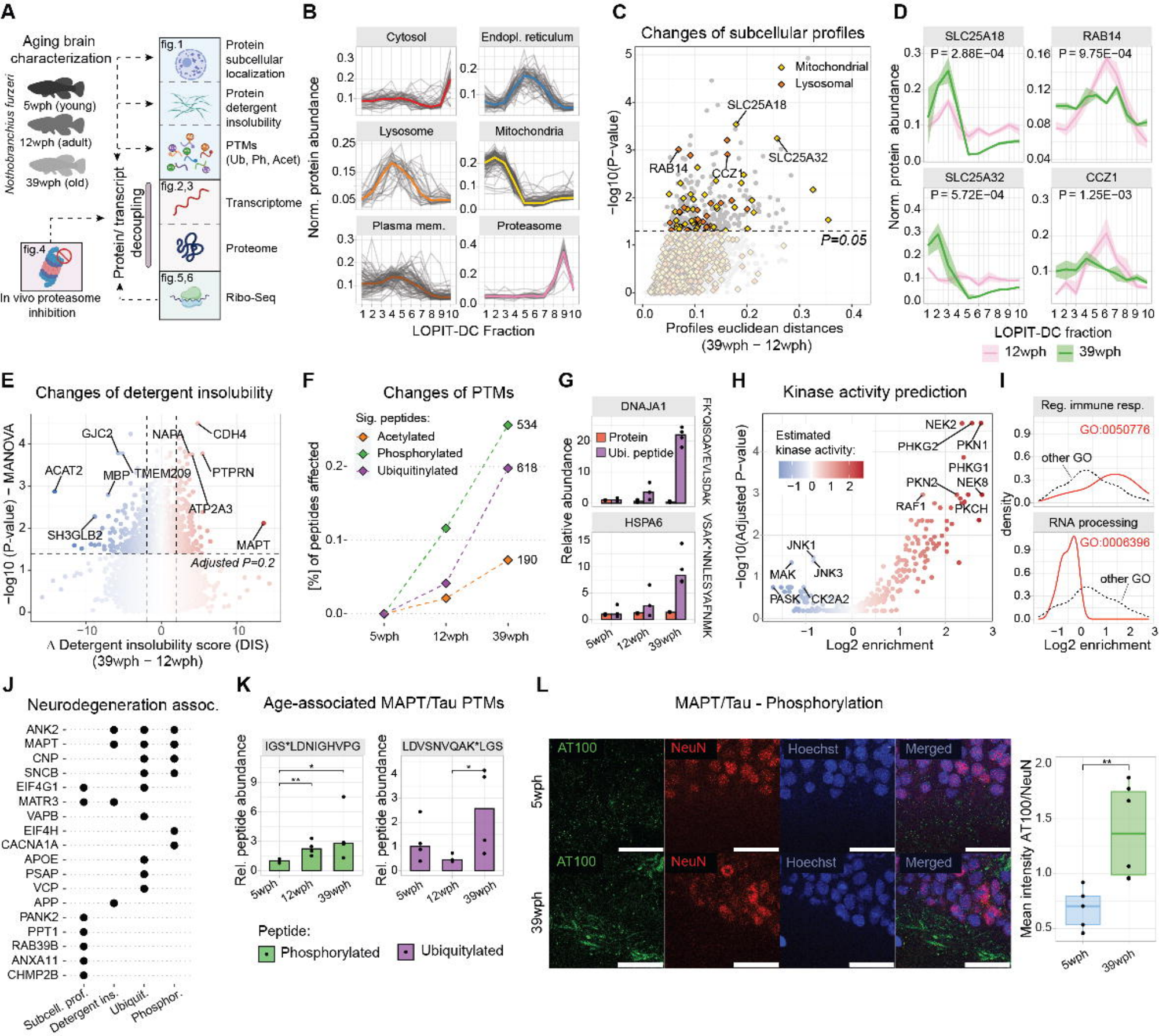
A
Aging brain characterization
Nothobranchius furzeri
5wph (young)
12wph (adult)
39wph (old)
fig.1
Protein subcellular localization
Protein detergent insolubility
PTMs (Ub, Ph, Acet)
fig.2,3
Transcriptome
Proteome
fig.5,6
Ribo-Seq
Protein/ transcript decoupling
fig.4
In vivo proteasome inhibition
B
Cytosol
Endopl. reticulum
Lysosome
Mitochondria
Plasma mem.
Proteasome
Norm. protein abundance
LOPIT-DC Fraction
C
Changes of subcellular profiles
Mitochondrial
Lysosomal
SLC25A18
SLC25A32
RAB14
CCZ1
P=0.05
−log10(P−value)
Profiles euclidean distances (39wph − 12wph)
D
SLC25A18
P = 2.88E−04
RAB14
P = 9.75E−04
SLC25A32
P = 5.72E−04
CCZ1
P = 1.25E−03
Norm. protein abundance
LOPIT-DC fraction
12wph
39wph
E
Changes of detergent insolubility
GJC2
NAPA
CDH4
ACAT2
MBP
TMEM209
PTPRN
ATP2A3
SH3GLB2
MAPT
Adjusted P=0.2
−log10 (P-value) − MANOVA
Δ Detergent insolubility score (DIS) (39wph − 12wph)
F
Changes of PTMs
Sig. peptides:
Acetylated
Phosphorylated
Ubiquitinylated
534
618
190
[%] of peptides affected
5wph
12wph
39wph
G
DNAJA1
Protein
Ubi. peptide
FK*QISQAYEVLSDAK
HSPA6
VSAK*NNLESYAFNMK
Relative abundance
H
Kinase activity prediction
Estimated kinase activity:
NEK2
PHKG2
PKN1
PHKG1
PKN2
NEK8
RAF1
PKCH
JNK1
MAK
JNK3
PASK
CK2A2
−log10(Adjusted P−value)
Log2 enrichment
I
Reg. immune resp.
GO:0050776
other GO
RNA processing
GO:0006396
other GO
density
Log2 enrichment
J
Neurodegeneration assoc.
ANK2
MAPT
CNP
SNCB
EIF4G1
MATR3
VAPB
EIF4H
CACNA1A
APOE
PSAP
VCP
APP
PANK2
PPT1
RAB39B
ANXA11
CHMP2B
Subcell. prof.
Detergent ins.
Ubiquit.
Phosphor.
K
Age-associated MAPT/Tau PTMs
IGS*LDNIGHVPG
LDVSNVQAK*LGS
Rel. peptide abundance
5wph
12wph
39wph
Peptide:
Phosphorylated
Ubiquitylated
L
MAPT/Tau - Phosphorylation
AT100
NeuN
Hoechst
Merged
5wph
39wph
Mean intensity AT100/NeuN

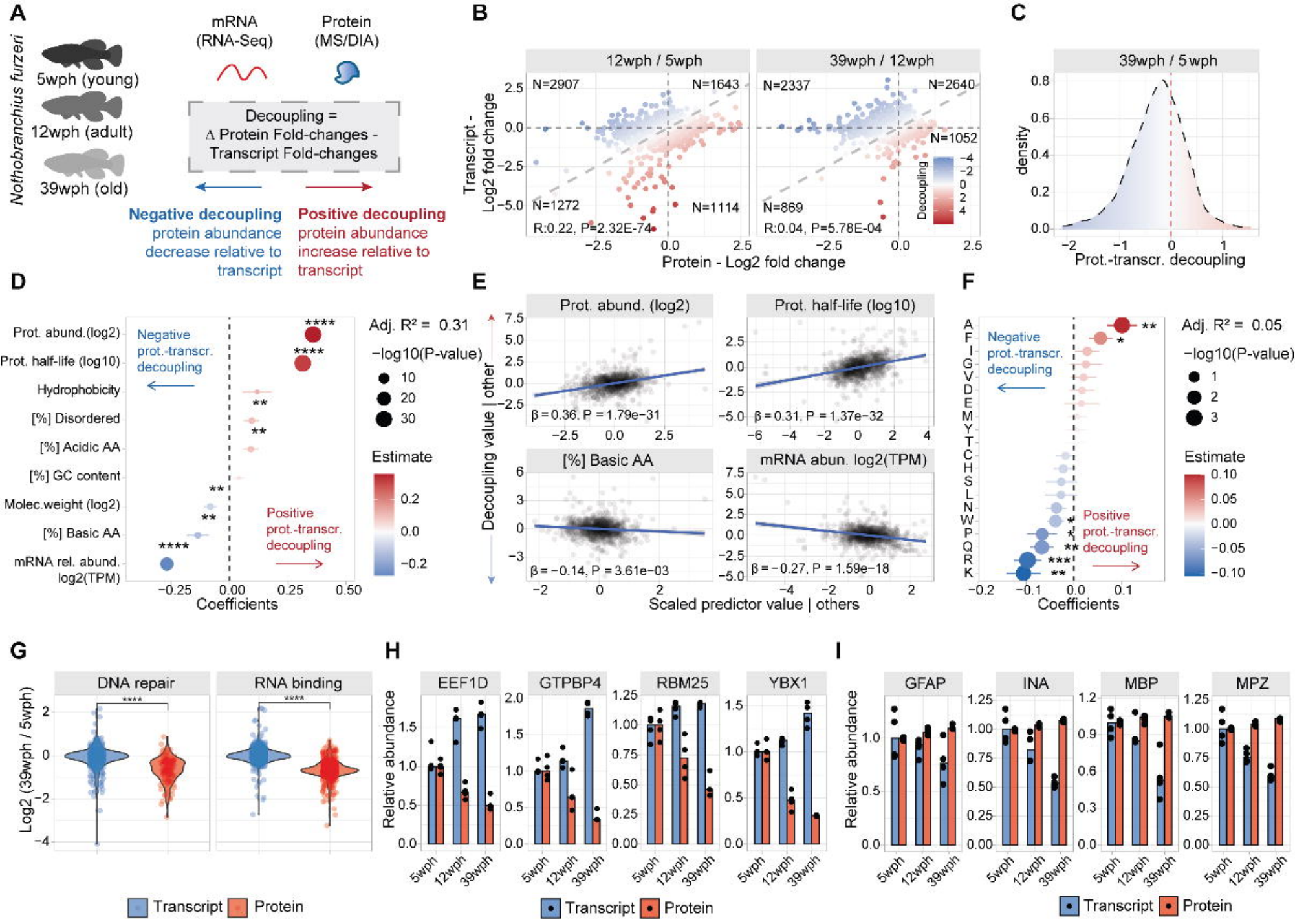
A
Nothobranchius furzeri
5wph (young)
12wph (adult)
39wph (old)
mRNA (RNA-Seq)
Protein (MS/DIA)
Decoupling = Δ Protein Fold-changes - Transcript Fold-changes
Negative decoupling
protein abundance decrease relative to transcript
Positive decoupling
protein abundance increase relative to transcript
B
12wph / 5wph
39wph / 12wph
N=2907
N=1643
N=1272
N=1114
N=2337
N=2640
N=1052
N=869
R:0.22, P=2.32E-74
R:0.04, P=5.78E-04
Decoupling
Transcript - Log2 fold change
Protein - Log2 fold change
C
39wph / 5wph
density
Prot.-transcr. decoupling
D
Prot. abund.(log2)
Prot. half-life (log10)
Hydrophobicity
[%] Disordered
[%] Acidic AA
[%] GC content
Molec.weight (log2)
[%] Basic AA
mRNA rel. abund. log2(TPM)
Negative prot.-transcr. decoupling
Positive prot.-transcr. decoupling
Adj. R² = 0.31
−log10(P-value)
Estimate
Coefficients
E
Prot. abund. (log2)
Prot. half-life (log10)
[%] Basic AA
mRNA abun. log2(TPM)
β = 0.36, P = 1.79e−31
β = 0.31, P = 1.37e−32
β = −0.14, P = 3.61e−03
β = −0.27, P = 1.59e−18
Decoupling value | other
Scaled predictor value | others
F
Negative prot.-transcr. decoupling
Positive prot.-transcr. decoupling
Adj. R² = 0.05
−log10(P-value)
Estimate
Coefficients
G
DNA repair
RNA binding
Log2 (39wph / 5wph)
Transcript
Protein
H
EEF1D
GTPBP4
RBM25
YBX1
Relative abundance
5wph
12wph
39wph
Transcript
Protein
I
GFAP
INA
MBP
MPZ
Relative abundance
5wph
12wph
39wph
Transcript
Protein

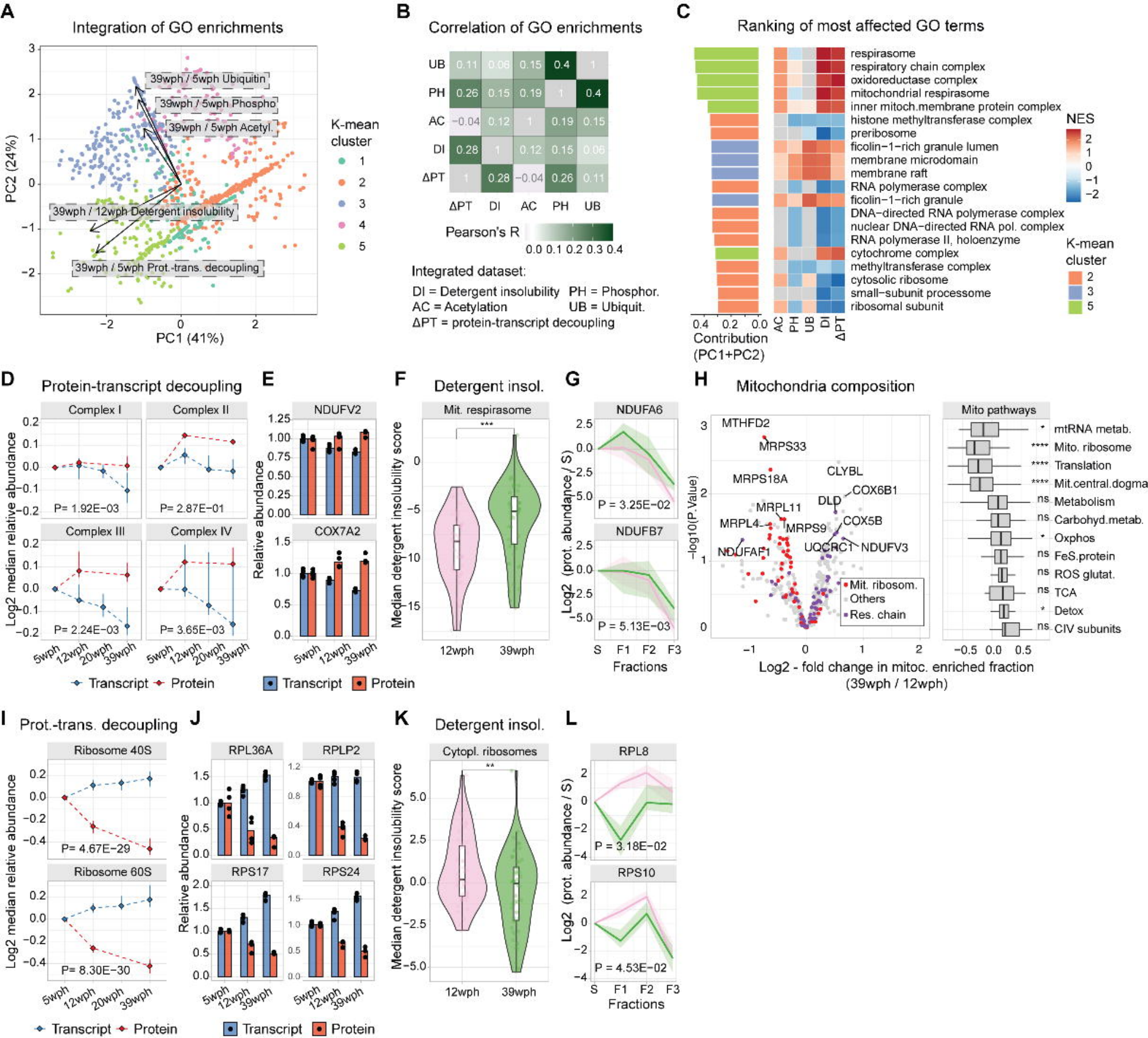
A
Integration of GO enrichments
39wph / 5wph Ubiquitin
39wph / 5wph Phospho
39wph / 5wph Acetyl.
39wph / 12wph Detergent insolubility
39wph / 5wph Prot.-trans. decoupling
PC1 (41%)
PC2 (24%)
K-mean cluster
1
2
3
4
5
B
Correlation of GO enrichments
UB 0.11 0.06 0.15 0.4 1
PH 0.26 0.15 0.19 1 0.4
AC −0.04 0.12 1 0.19 0.15
DI 0.28 1 0.12 0.15 0.06
ΔPT 1 0.28 −0.04 0.26 0.11
ΔPT DI AC PH UB
Pearson's R
0.0 0.1 0.2 0.3 0.4
Integrated dataset:
DI = Detergent insolubility PH = Phosphor.
AC = Acetylation UB = Ubiquit.
ΔPT = protein-transcript decoupling
C
Ranking of most affected GO terms
respirasome
respiratory chain complex
oxidoreductase complex
mitochondrial respirasome
inner mitoch.membrane protein complex
histone methyltransferase complex
preribosome
ficolin−1−rich granule lumen
membrane microdomain
membrane raft
RNA polymerase complex
ficolin−1−rich granule
DNA−directed RNA polymerase complex
nuclear DNA−directed RNA pol. complex
RNA polymerase II, holoenzyme
cytochrome complex
methyltransferase complex
cytosolic ribosome
small−subunit processome
ribosomal subunit
Contribution (PC1+PC2)
AC PH UB DI ΔPT
NES
K-mean cluster
2
3
5
D
Protein-transcript decoupling
Complex I
Complex II
Complex III
Complex IV
P= 1.92E−03
P= 2.87E−01
P= 2.24E−03
P= 3.65E−03
Log2 median relative abundance
5wph 12wph 20wph 39wph
Transcript Protein
E
NDUFV2
COX7A2
Relative abundance
5wph 12wph 20wph 39wph
Transcript Protein
F
Detergent insol.
Mit. respirasome
***
Median detergent insolubility score
12wph 39wph
G
NDUFA6
P = 3.25E−02
NDUFB7
P = 5.13E−03
Log2 (prot. abundance / S)
S F1 F2 F3
Fractions
H
Mitochondria composition
MTHFD2
MRPS33
MRPS18A
CLYBL
COX6B1
DLD
MRPL11
MRPL4
MRPS9
COX5B
NDUFAF1
UQCRC1
NDUFV3
Mit. ribosom.
Others
Res. chain
−log10(P.Value)
Log2 - fold change in mitoc. enriched fraction
(39wph / 12wph)
Mito pathways
mtRNA metab. *
Mito. ribosome ****
Translation ****
Mit.central.dogma ****
Metabolism ns
Carbohyd.metab. ns
Oxphos *
FeS.protein ns
ROS glutat. ns
TCA ns
Detox *
CIV subunits ns
I
Prot.-trans. decoupling
Ribosome 40S
Ribosome 60S
P= 4.67E−29
P= 8.30E−30
Log2 median relative abundance
5wph 12wph 20wph 39wph
Transcript Protein
J
RPL36A
RPLP2
RPS17
RPS24
Relative abundance
5wph 12wph 39wph
Transcript Protein
K
Detergent insol.
Cytopl. ribosomes
**
Median detergent insolubility score
12wph 39wph
L
RPL8
P = 3.18E−02
RPS10
P = 4.53E−02
Log2 (prot. abundance / S)
S F1 F2 F3
Fractions

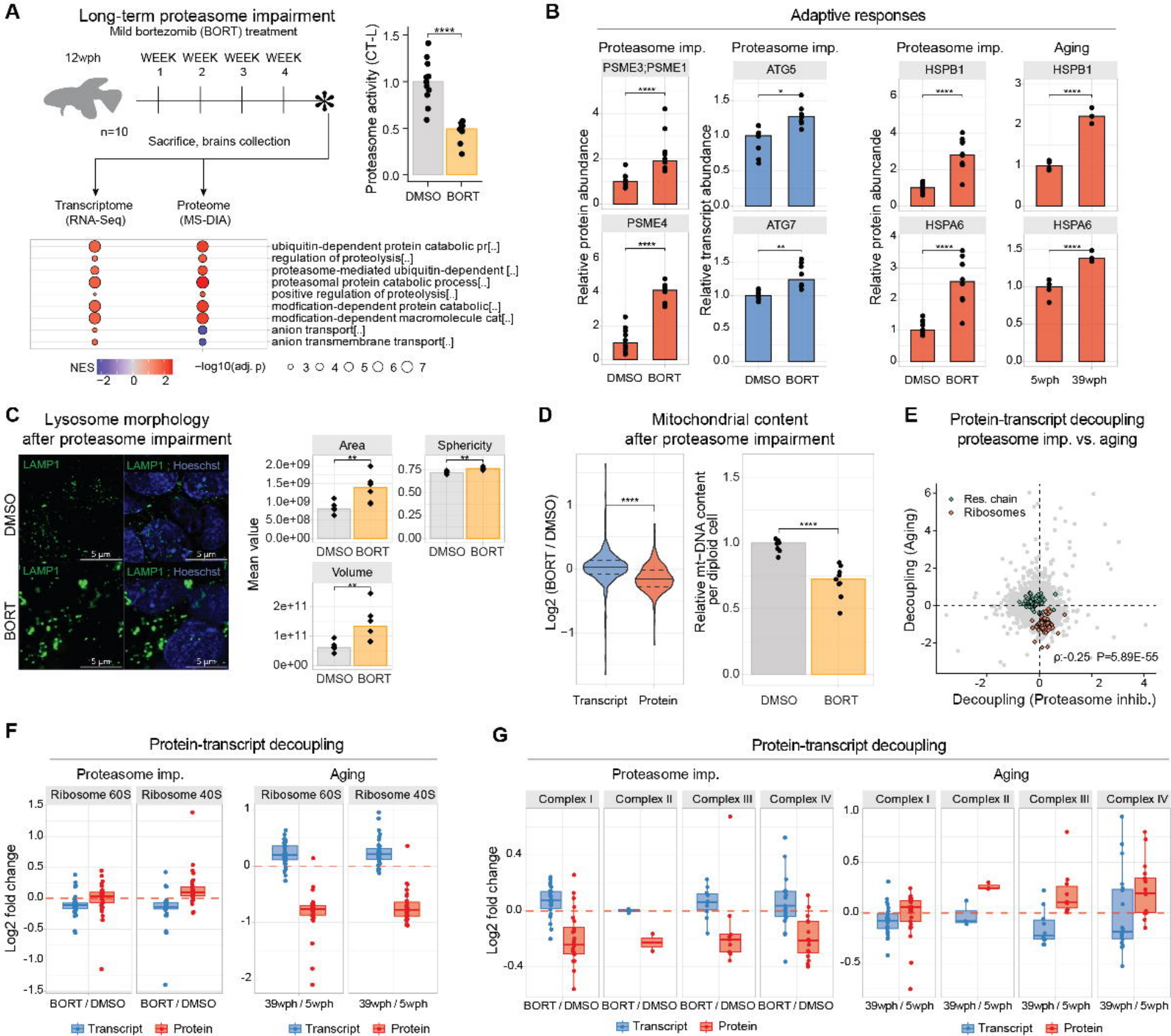
A
Long-term proteasome impairment
Mild bortezomib (BORT) treatment
12wph
WEEK 1
WEEK 2
WEEK 3
WEEK 4
n=10
Sacrifice, brains collection
Transcriptome (RNA-Seq)
Proteome (MS-DIA)
Proteasome activity (CT-L)
DMSO BORT
ubiquitin-dependent protein catabolic pr[..]
regulation of proteolysis[..]
proteasome-mediated ubiquitin-dependent [..]
proteasomal protein catabolic process[..]
positive regulation of proteolysis[..]
modfication-dependent protein catabolic[..]
modfication-dependent macromolecule cat[..]
anion transport[..]
anion transmembrane transport[..]
NES
−log10(adj. p)
B
Adaptive responses
Proteasome imp.
Aging
PSME3;PSME1
PSME4
ATG5
ATG7
HSPB1
HSPA6
Relative protein abundance
Relative transcript abundance
Relative protein abuncande
DMSO BORT
5wph 39wph
C
Lysosome morphology after proteasome impairment
LAMP1
LAMP1 ; Hoeschst
DMSO
BORT
Area
Sphericity
Volume
Mean value
D
Mitochondrial content after proteasome impairment
Log2 (BORT / DMSO)
Transcript Protein
Relative mt−DNA content per diploid cell
E
Protein-transcript decoupling proteasome imp. vs. aging
Res. chain
Ribosomes
Decoupling (Aging)
Decoupling (Proteasome inhib.)
ρ:-0.25 P=5.89E-55
F
Protein-transcript decoupling
Proteasome imp.
Aging
Ribosome 60S
Ribosome 40S
Log2 fold change
BORT / DMSO
39wph / 5wph
Transcript
Protein
G
Protein-transcript decoupling
Proteasome imp.
Aging
Complex I
Complex II
Complex III
Complex IV
Log2 fold change
BORT / DMSO
39wph / 5wph
Transcript
Protein

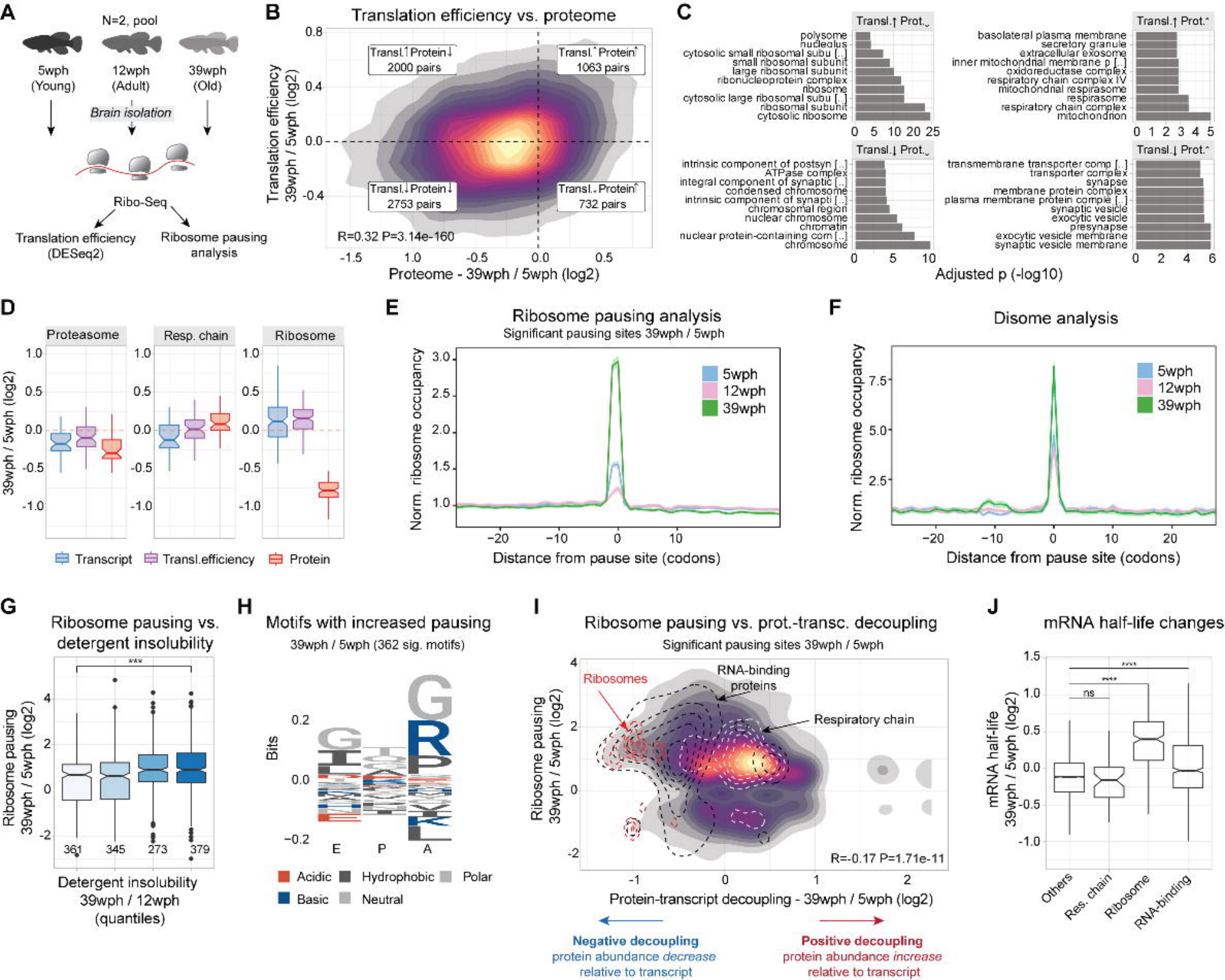
A
N=2, pool
5wph (Young)
12wph (Adult)
39wph (Old)
Brain isolation
Ribo-Seq
Translation efficiency (DESeq2)
Ribosome pausing analysis
B
Translation efficiency vs. proteome
Transl.↑ Protein↓ 2000 pairs
Transl.↑ Protein↑ 1063 pairs
Transl.↓ Protein↓ 2753 pairs
Transl.↓ Protein↑ 732 pairs
R=0.32 P=3.14e-160
Translation efficiency 39wph / 5wph (log2)
Proteome - 39wph / 5wph (log2)
C
Transl.↑ Prot.⌄
polysome
nucleolus
cytosolic small ribosomal subu [..]
small ribosomal subunit
large ribosomal subunit
ribonucleoprotein complex
ribosome
cytosolic large ribosomal subu [..]
ribosomal subunit
cytosolic ribosome
Transl.↑ Prot.⌃
basolateral plasma membrane
secretory granule
extracellular exosome
inner mitochondrial membrane p [..]
oxidoreductase complex
respiratory chain complex IV
mitochondrial respirasome
respirasome
respiratory chain complex
mitochondrion
Transl.↓ Prot.⌄
intrinsic component of postsyn [..]
ATPase complex
integral component of synaptic [..]
condensed chromosome
intrinsic component of synapti [..]
chromosomal region
nuclear chromosome
chromatin
nuclear protein-containing com [..]
chromosome
Transl.↓ Prot.⌃
transmembrane transporter comp [..]
transporter complex
synapse
membrane protein complex
plasma membrane protein comple [..]
synaptic vesicle
exocytic vesicle
presynapse
exocytic vesicle membrane
synaptic vesicle membrane
Adjusted p (-log10)
D
Proteasome
Resp. chain
Ribosome
39wph / 5wph (log2)
Transcript
Transl.efficiency
Protein
E
Ribosome pausing analysis
Significant pausing sites 39wph / 5wph
Norm. ribosome occupancy
5wph
12wph
39wph
Distance from pause site (codons)
F
Disome analysis
Norm. ribosome occupancy
5wph
12wph
39wph
Distance from pause site (codons)
G
Ribosome pausing vs. detergent insolubility
Ribosome pausing 39wph / 5wph (log2)
361
345
273
379
Detergent insolubility 39wph / 12wph (quantiles)
H
Motifs with increased pausing
39wph / 5wph (362 sig. motifs)
Bits
E
P
A
Acidic
Hydrophobic
Polar
Basic
Neutral
I
Ribosome pausing vs. prot.-transc. decoupling
Significant pausing sites 39wph / 5wph
Ribosomes
RNA-binding proteins
Respiratory chain
R=-0.17 P=1.71e-11
Ribosome pausing 39wph / 5wph (log2)
Protein-transcript decoupling - 39wph / 5wph (log2)
Negative decoupling
protein abundance decrease
relative to transcript
Positive decoupling
protein abundance increase
relative to transcript
J
mRNA half-life changes
mRNA half-life 39wph / 5wph (log2)
ns
Others
Res. chain
Ribosome
RNA-binding

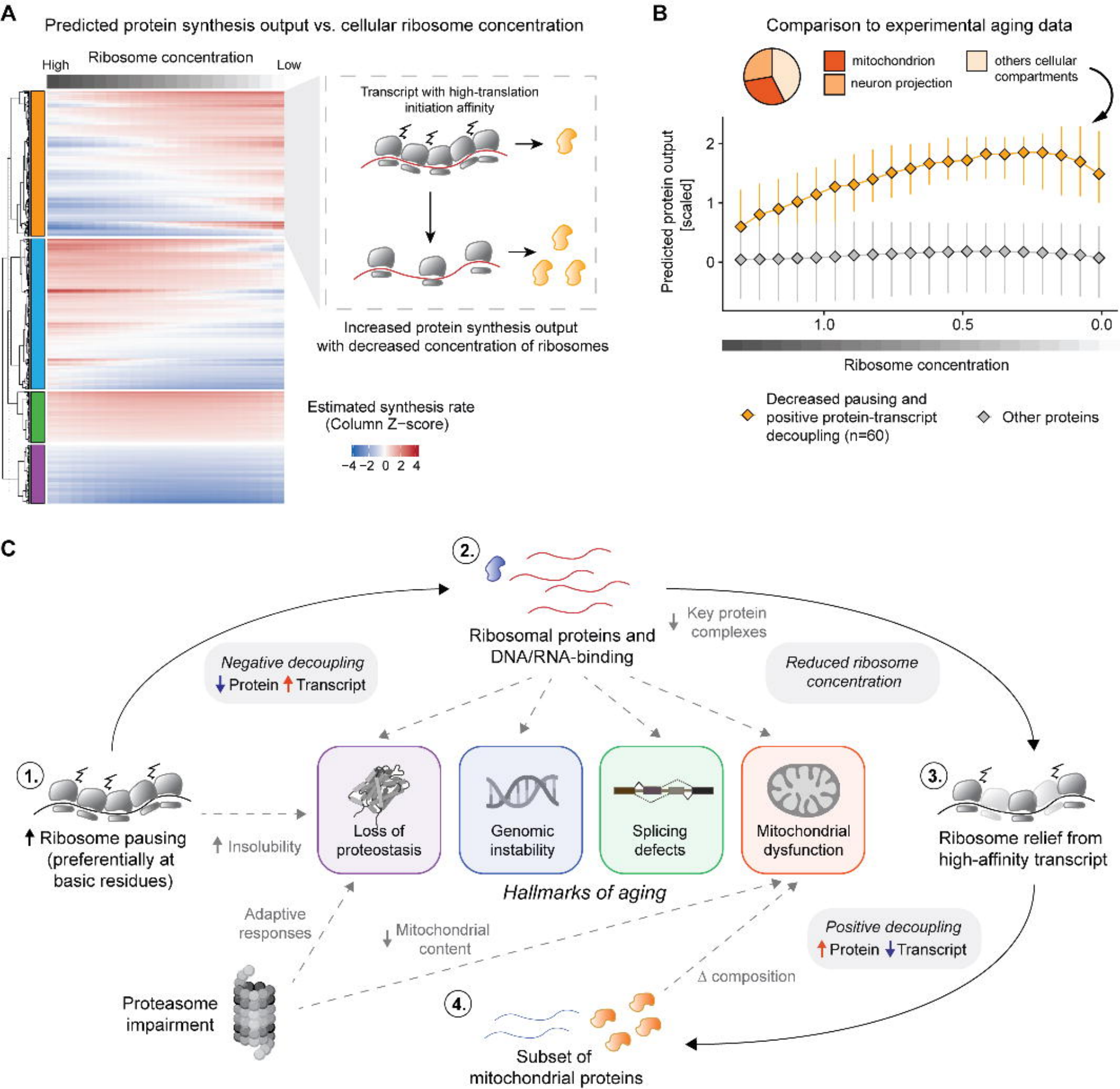
A
Predicted protein synthesis output vs. cellular ribosome concentration
High
Ribosome concentration
Low
Transcript with high-translation initiation affinity
Increased protein synthesis output with decreased concentration of ribosomes
Estimated synthesis rate (Column Z−score)
−4 −2 0 2 4
B
Comparison to experimental aging data
mitochondrion
neuron projection
others cellular compartments
Predicted protein output [scaled]
2
1
0
1.0
0.5
0.0
Ribosome concentration
Decreased pausing and positive protein-transcript decoupling (n=60)
Other proteins
C
2.
Ribosomal proteins and DNA/RNA-binding
Key protein complexes
Negative decoupling
Protein Transcript
Reduced ribosome concentration
1.
Ribosome pausing (preferentially at basic residues)
Insolubility
Loss of proteostasis
Genomic instability
Splicing defects
Mitochondrial dysfunction
3.
Ribosome relief from high-affinity transcript
Hallmarks of aging
Adaptive responses
Mitochondrial content
Positive decoupling
Protein Transcript
Δ composition
Proteasome impairment
4.
Subset of mitochondrial proteins

Nothobranchius furzeri - brain aging

5wph (young) 12wph (adult) 39wph (old)

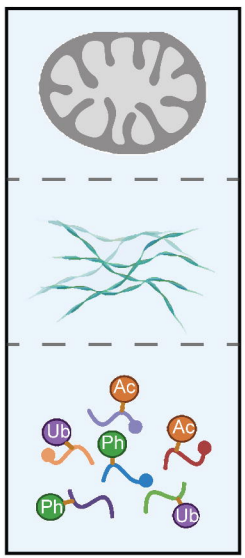

Organelle composition

Proteome solubility

Post-transl. modification

Mitochondria & OXPHOS

Ribosomes

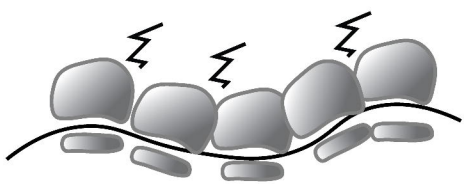

K,R
aa

Ribosome pausing
=
Loss of basic proteins
(Ribosomal proteins,
RNA/DNA binding)

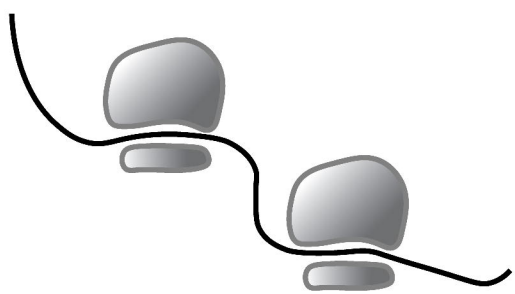

Remodelling of protein synthesis

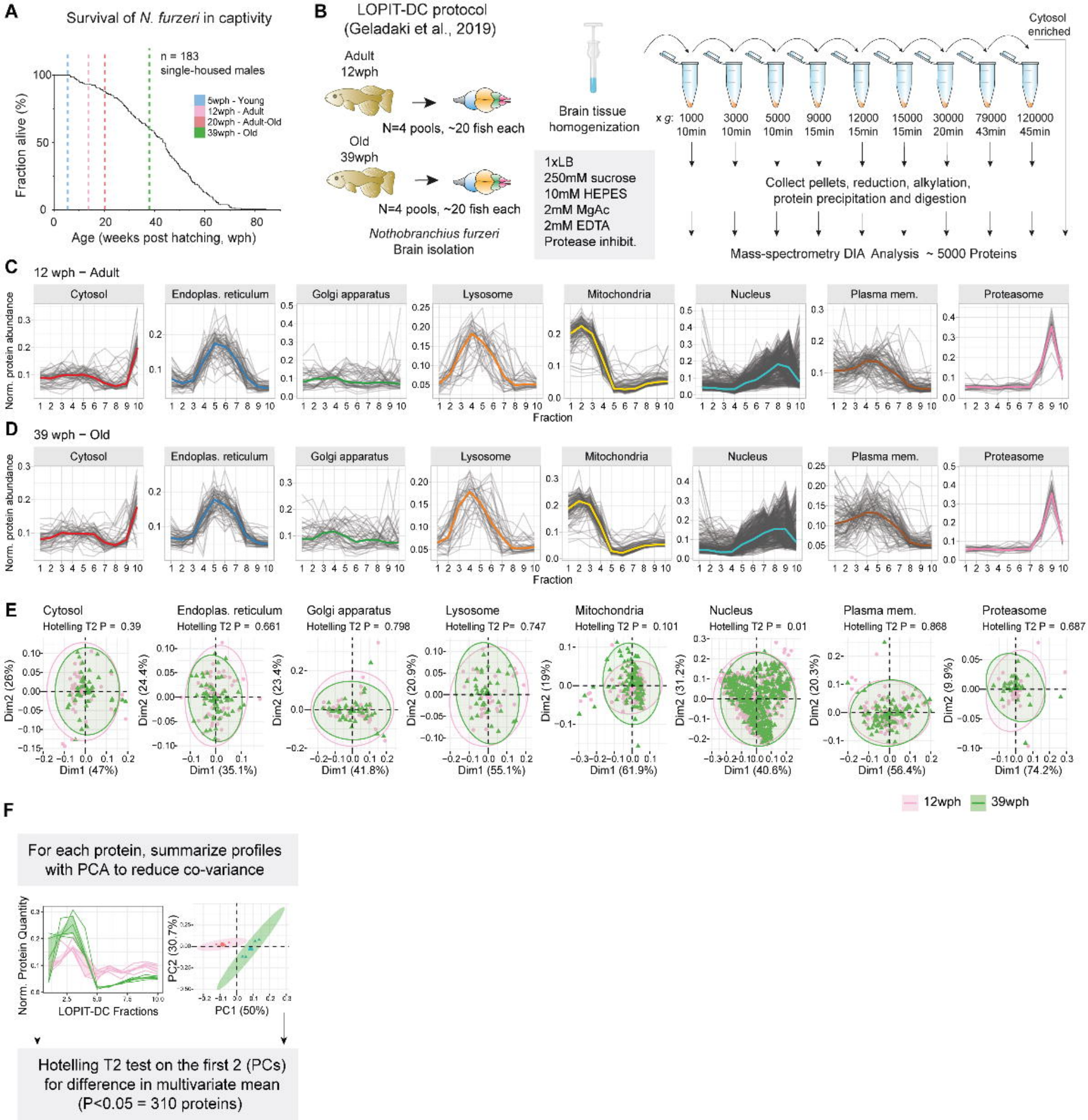
A
Survival of N. furzeri in captivity
n = 183
single-housed males
5wph - Young
12wph - Adult
20wph - Adult-Old
39wph - Old
Fraction alive (%)
Age (weeks post hatching, wph)
B
LOPIT-DC protocol
(Geladaki et al., 2019)
Adult
12wph
N=4 pools, ~20 fish each
Old
39wph
N=4 pools, ~20 fish each
Nothobranchius furzeri
Brain isolation
Brain tissue
homogenization
1xLB
250mM sucrose
10mM HEPES
2mM MgAc
2mM EDTA
Protease inhibit.
Cytosol
enriched
x g: 1000 10min
3000 10min
5000 10min
9000 15min
12000 15min
15000 15min
30000 20min
79000 43min
120000 45min
Collect pellets, reduction, alkylation,
protein precipitation and digestion
Mass-spectrometry DIA Analysis ~ 5000 Proteins
C
12 wph − Adult
Cytosol
Endoplas. reticulum
Golgi apparatus
Lysosome
Mitochondria
Nucleus
Plasma mem.
Proteasome
Norm. protein abundance
Fraction
D
39 wph − Old
Cytosol
Endoplas. reticulum
Golgi apparatus
Lysosome
Mitochondria
Nucleus
Plasma mem.
Proteasome
Norm. protein abundance
Fraction
E
Cytosol
Hotelling T2 P = 0.39
Endoplas. reticulum
Hotelling T2 P = 0.661
Golgi apparatus
Hotelling T2 P = 0.798
Lysosome
Hotelling T2 P= 0.747
Mitochondria
Hotelling T2 P = 0.101
Nucleus
Hotelling T2 P = 0.01
Plasma mem.
Hotelling T2 P = 0.868
Proteasome
Hotelling T2 P = 0.687
Dim2 (26%)
Dim1 (47%)
Dim2 (24.4%)
Dim1 (35.1%)
Dim2 (23.4%)
Dim1 (41.8%)
Dim2 (20.9%)
Dim1 (55.1%)
Dim2 (19%)
Dim1 (61.9%)
Dim2 (31.2%)
Dim1 (40.6%)
Dim2 (20.3%)
Dim1 (58.4%)
Dim2 (9.9%)
Dim1 (74.2%)
12wph
39wph
F
For each protein, summarize profiles
with PCA to reduce co-variance
Norm. Protein Quantity
LOPIT-DC Fractions
PC2 (30.7%)
PC1 (50%)
Hotelling T2 test on the first 2 (PCs)
for difference in multivariate mean
(P<0.05 = 310 proteins)

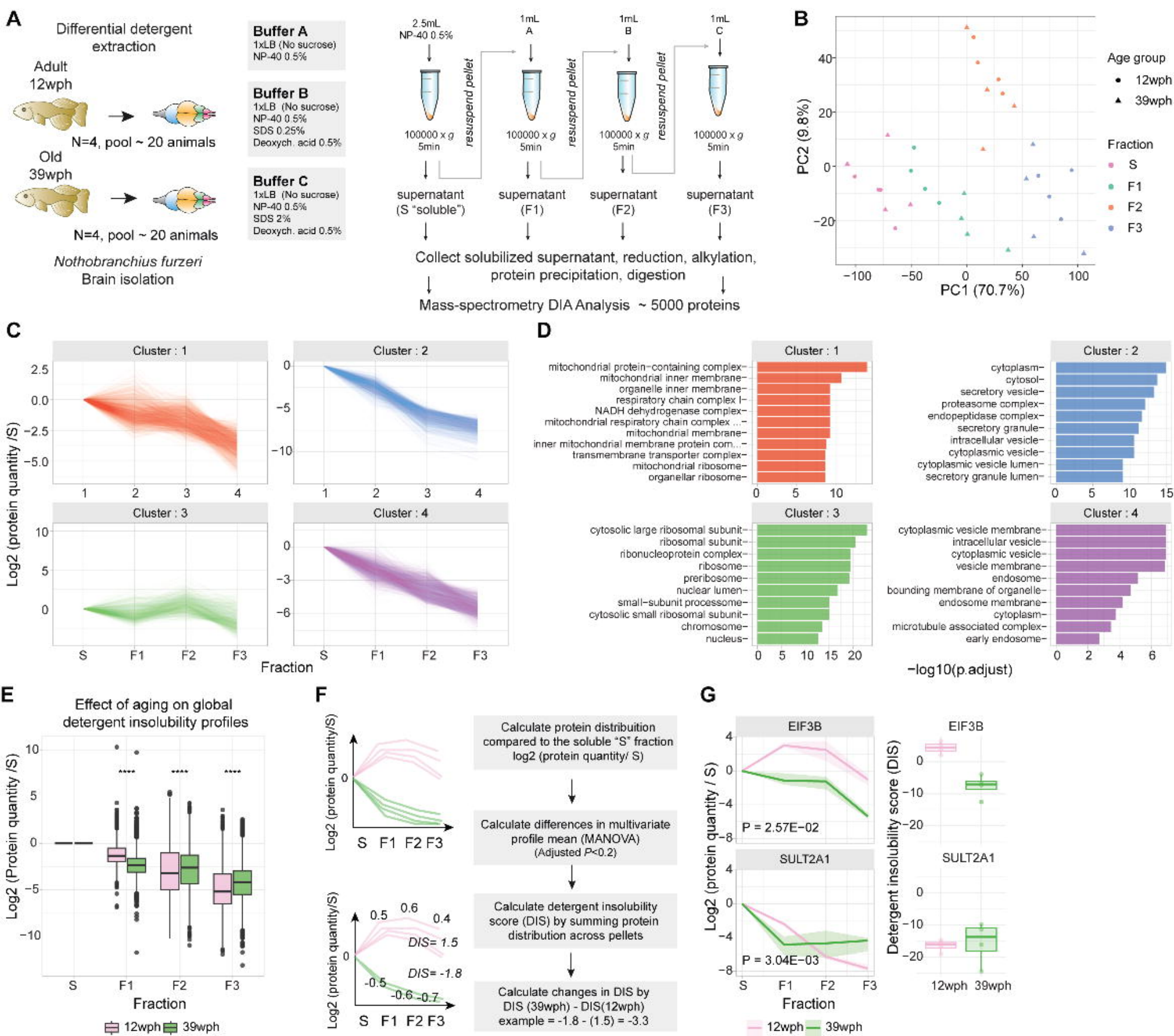
A
Differential detergent extraction
Adult 12wph
N=4, pool ~ 20 animals
Old 39wph
N=4, pool ~ 20 animals
Nothobranchius furzeri
Brain isolation
Buffer A
1xLB (No sucrose)
NP-40 0.5%
Buffer B
1xLB (No sucrose)
NP-40 0.5%
SDS 0.25%
Deoxych. acid 0.5%
Buffer C
1xLB (No sucrose)
NP-40 0.5%
SDS 2%
Deoxych. acid 0.5%
2.5mL NP-40 0.5%
1mL A
1mL B
1mL C
resuspend pellet
100000 x g 5min
supernatant (S "soluble")
supernatant (F1)
supernatant (F2)
supernatant (F3)
Collect solubilized supernatant, reduction, alkylation, protein precipitation, digestion
Mass-spectrometry DIA Analysis ~ 5000 proteins
B
PC2 (9.8%)
PC1 (70.7%)
Age group
12wph
39wph
Fraction
S
F1
F2
F3
C
Cluster : 1
Cluster : 2
Cluster : 3
Cluster : 4
Log2 (protein quantity /S)
Fraction
D
mitochondrial protein−containing complex
mitochondrial inner membrane
organelle inner membrane
respiratory chain complex I
NADH dehydrogenase complex
mitochondrial respiratory chain complex ...
mitochondrial membrane
inner mitochondrial membrane protein com...
transmembrane transporter complex
mitochondrial ribosome
organellar ribosome
cytoplasm
cytosol
secretory vesicle
proteasome complex
endopeptidase complex
secretory granule
intracellular vesicle
cytoplasmic vesicle
cytoplasmic vesicle lumen
secretory granule lumen
cytosolic large ribosomal subunit
ribosomal subunit
ribonucleoprotein complex
ribosome
preribosome
nuclear lumen
small−subunit processome
cytosolic small ribosomal subunit
chromosome
nucleus
cytoplasmic vesicle membrane
intracellular vesicle
cytoplasmic vesicle
vesicle membrane
endosome
bounding membrane of organelle
endosome membrane
cytoplasm
microtubule associated complex
early endosome
−log10(p.adjust)
E
Effect of aging on global detergent insolubility profiles
Log2 (Protein quantity /S)
Fraction
12wph
39wph
F
Log2 (protein quantity/S)
DIS= 1.5
DIS= -1.8
Calculate protein distribuition compared to the soluble "S" fraction log2 (protein quantity/ S)
Calculate differences in multivariate profile mean (MANOVA) (Adjusted P<0.2)
Calculate detergent insolubility score (DIS) by summing protein distribution across pellets
Calculate changes in DIS by DIS (39wph) - DIS(12wph) example = -1.8 - (1.5) = -3.3
G
EIF3B
SULT2A1
Log2 (protein quantity / S)
P = 2.57E−02
P = 3.04E−03
Detergent insolubility score (DIS)
12wph
39wph

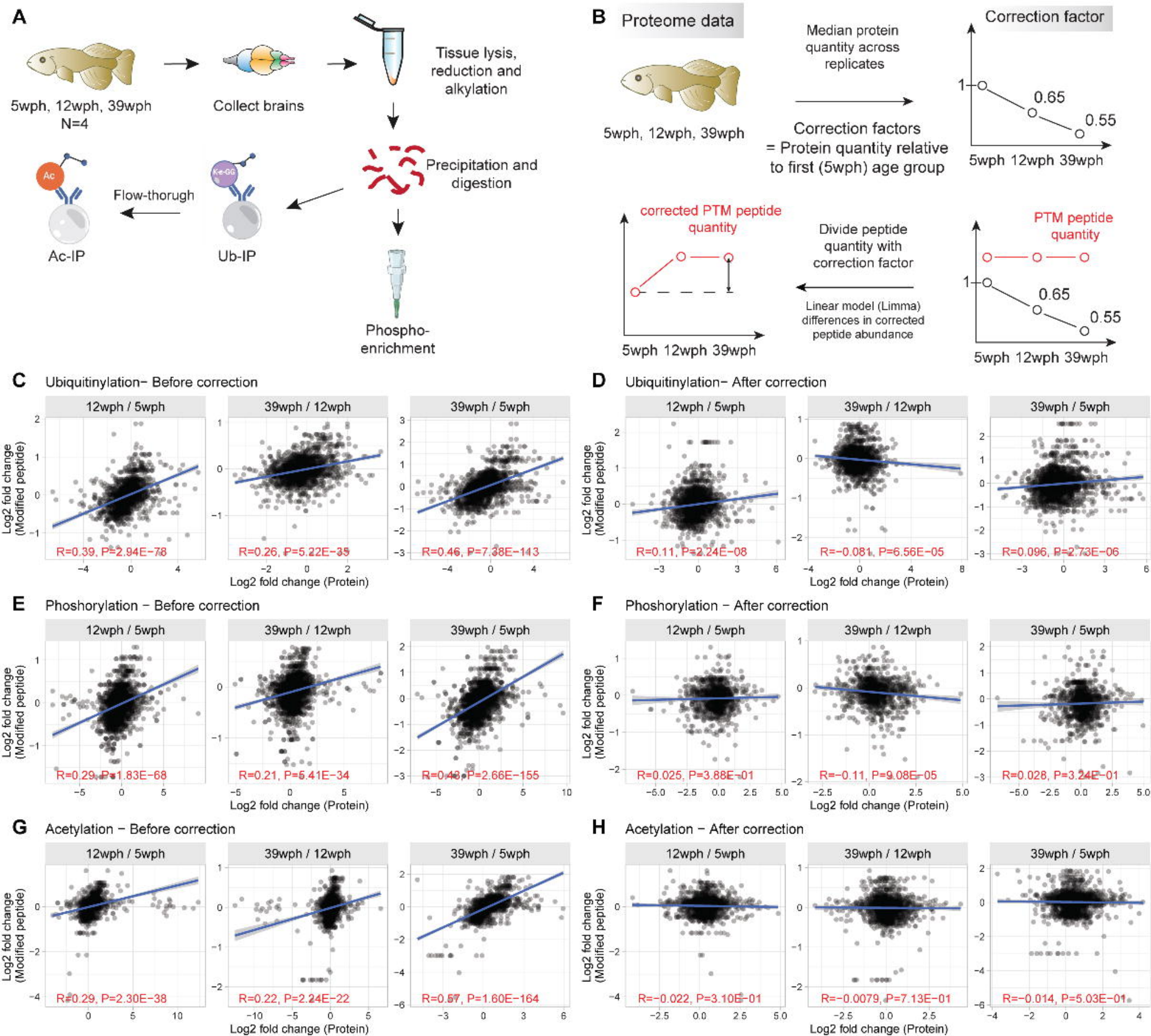
A
5wph, 12wph, 39wph
N=4
Collect brains
Tissue lysis, reduction and alkylation
Precipitation and digestion
Phospho-enrichment
Ac-IP
Ub-IP
Flow-thorugh
B
Proteome data
5wph, 12wph, 39wph
Median protein quantity across replicates
Correction factors = Protein quantity relative to first (5wph) age group
Correction factor
1
0.65
0.55
5wph 12wph 39wph
corrected PTM peptide quantity
Divide peptide quantity with correction factor
Linear model (Limma) differences in corrected peptide abundance
PTM peptide quantity
C
Ubiquitinylation− Before correction
D
Ubiquitinylation− After correction
E
Phoshorylation − Before correction
F
Phoshorylation − After correction
G
Acetylation − Before correction
H
Acetylation − After correction
12wph / 5wph
39wph / 12wph
39wph / 5wph
Log2 fold change (Modified peptide)
Log2 fold change (Protein)
R=0.39, P=2.94E−78
R=0.26, P=5.22E−35
R=0.46, P=7.38E−143
R=0.11, P=2.24E−08
R=−0.081, P=6.56E−05
R=0.096, P=2.73E−06
R=0.29, P=1.83E−68
R=0.21, P=5.41E−34
R=0.48, P=2.66E−155
R=0.025, P=3.88E−01
R=−0.11, P=9.08E−05
R=0.028, P=3.24E−01
R=0.29, P=2.30E−38
R=0.22, P=2.24E−22
R=0.57, P=1.60E−164
R=−0.022, P=3.10E−01
R=−0.0079, P=7.13E−01
R=−0.014, P=5.03E−01

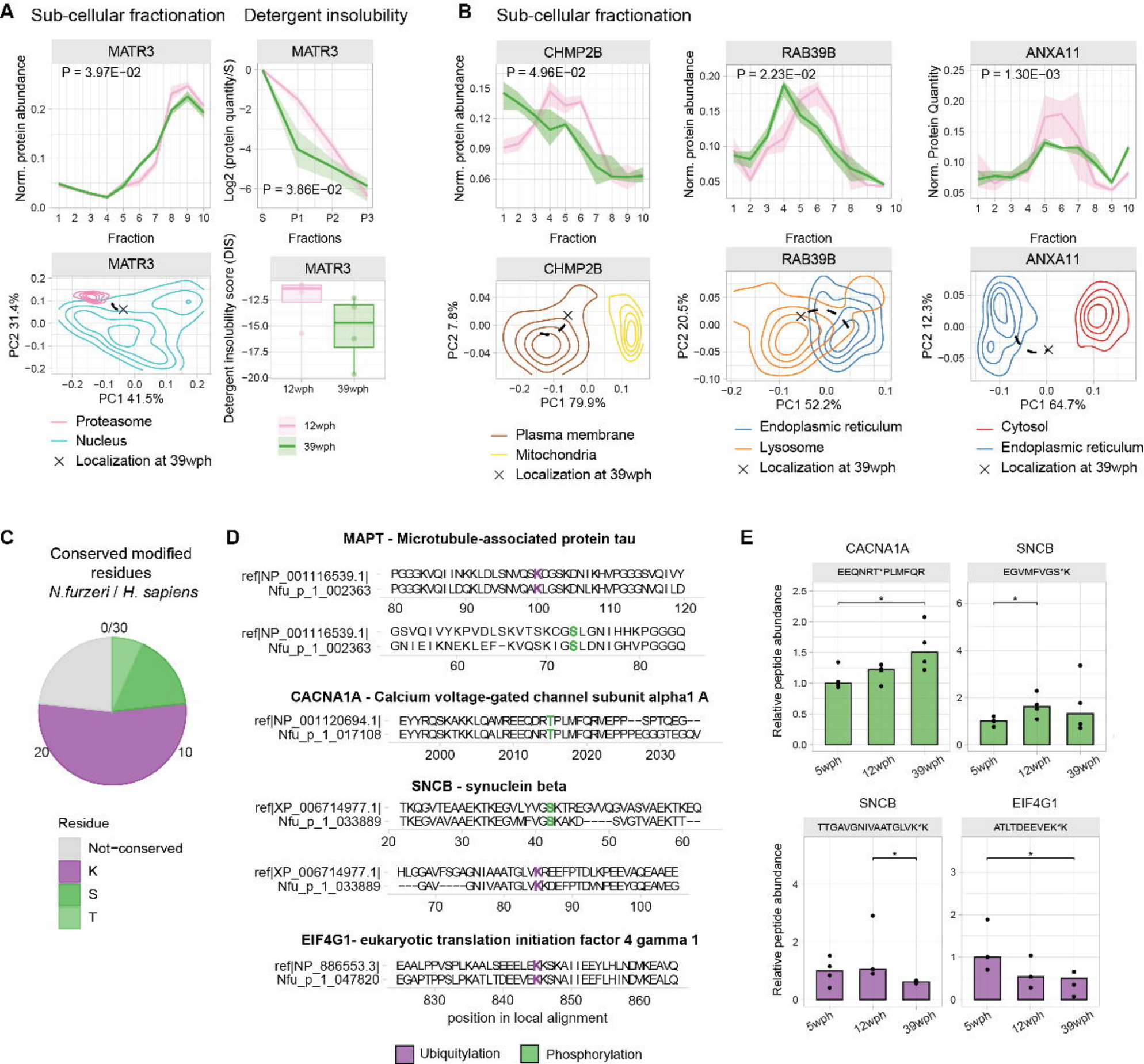
A
Sub-cellular fractionation
Detergent insolubility
MATR3
P = 3.97E−02
Norm. protein abundance
Fraction
MATR3
P = 3.86E−02
Log2 (protein quantity/S)
Fractions
MATR3
PC2 31.4%
PC1 41.5%
MATR3
Detergent insolubility score (DIS)
12wph
39wph
Proteasome
Nucleus
Localization at 39wph
12wph
39wph
B
Sub-cellular fractionation
CHMP2B
P = 4.96E−02
RAB39B
P = 2.23E−02
ANXA11
P = 1.30E−03
Norm. protein abundance
Norm. Protein Quantity
Fraction
CHMP2B
PC2 7.8%
PC1 79.9%
RAB39B
PC2 20.5%
PC1 52.2%
ANXA11
PC2 12.3%
PC1 64.7%
Plasma membrane
Mitochondria
Localization at 39wph
Endoplasmic reticulum
Lysosome
Localization at 39wph
Cytosol
Endoplasmic reticulum
Localization at 39wph
C
Conserved modified residues
N.furzeri / H. sapiens
0/30
20
10
Residue
Not−conserved
K
S
T
D
MAPT - Microtubule-associated protein tau
ref|NP_001116539.1| PGGGKVQIINKKLDLSNVQSKCGSKDNIKHVPGGGSVQIVY
Nfu_p_1_002363 PGGGKVQILDQKLDVSNVQAKLGSKDNLKHVPGGGNVQILD
80 90 100 110 120
ref|NP_001116539.1| GSVQIVYKPVDLSKVTSKCGSLGNIHHKPGGGQ
Nfu_p_1_002363 GNIEIKNEKLEF−KVQSKIGSLDNIGHVPGGGQ
60 70 80
CACNA1A - Calcium voltage-gated channel subunit alpha1 A
ref|NP_001120694.1| EYYRQSKAKKLQAMREEQDRTPLMFQRMEPP−−SPTQEG−−
Nfu_p_1_017108 EYYRQSKTKKLQALREEQNRTPLMFQRMEPPPEGGGTEGQV
2000 2010 2020 2030
SNCB - synuclein beta
ref|XP_006714977.1| TKQGVTEAAEKTKEGVLYVGSKTREGVVQGVASVAEKTKEQ
Nfu_p_1_033889 TKEGVAVAAEKTKEGVMFVGSKAKD−−−−SVGTVAEKTT−−
20 30 40 50 60
ref|XP_006714977.1| HLGGAVFSGAGNIAAATGLVKREEFPTDLKPEEVAQEAAEE
Nfu_p_1_033889 −−−GAV−−−−GNIVAATGLVKKDEFPTDVNPEEYGQEAMEG
70 80 90 100
EIF4G1- eukaryotic translation initiation factor 4 gamma 1
ref|NP_886553.3| EAALPPVSPLKAALSEEELEKKSKAIIEEYLHLNDMKEAVQ
Nfu_p_1_047820 EGAPTPPSLPKATLTDEEVEKKSNAIIEEFLHINDVKEALQ
830 840 850 860
position in local alignment
Ubiquitylation
Phosphorylation
E
CACNA1A
EEQNRT*PLMFQR
SNCB
EGVMFVGS*K
Relative peptide abundance
5wph 12wph 39wph
SNCB
TTGAVGNIVAATGLVK*K
EIF4G1
ATLTDEEVEK*K
Relative peptide abundance
5wph 12wph 39wph

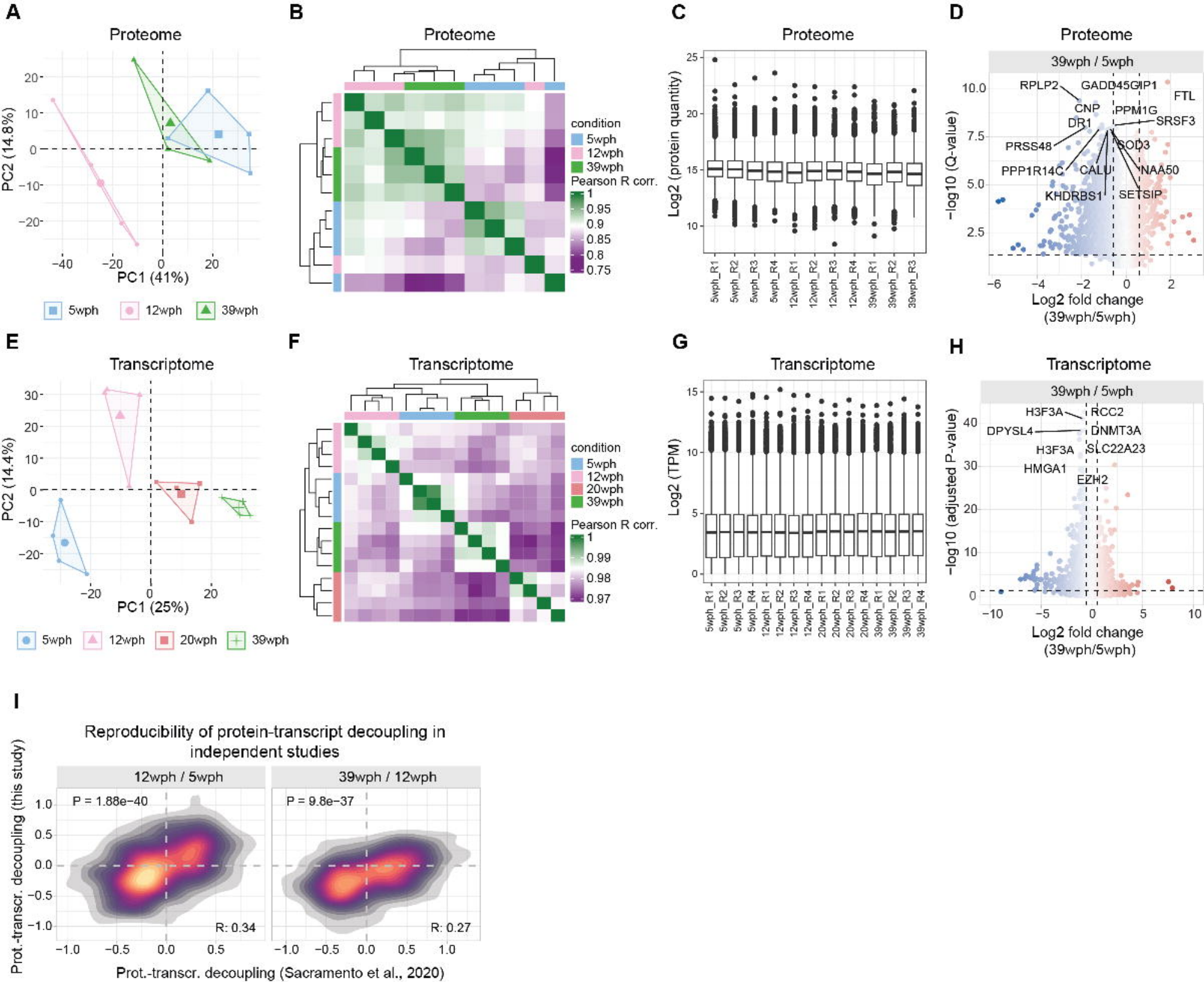
A
Proteome
PC2 (14.8%)
PC1 (41%)
5wph
12wph
39wph
B
Proteome
condition
5wph
12wph
39wph
Pearson R corr.
1
0.95
0.9
0.85
0.8
0.75
C
Proteome
Log2 (protein quantity)
5wph_R1
5wph_R2
5wph_R3
5wph_R4
12wph_R1
12wph_R2
12wph_R3
12wph_R4
39wph_R1
39wph_R2
39wph_R3
D
Proteome
39wph / 5wph
RPLP2
GADD45GIP1
FTL
CNP
PPM1G
DR1
SRSF3
PRSS48
SOD3
PPP1R14C
CALU
NAA50
KHDRBS1
SETSIP
−log10 (Q-value)
Log2 fold change
(39wph/5wph)
E
Transcriptome
PC2 (14.4%)
PC1 (25%)
5wph
12wph
20wph
39wph
F
Transcriptome
condition
5wph
12wph
20wph
39wph
Pearson R corr.
1
0.99
0.98
0.97
G
Transcriptome
Log2 (TPM)
5wph_R1
5wph_R2
5wph_R3
5wph_R4
12wph_R1
12wph_R2
12wph_R3
12wph_R4
20wph_R1
20wph_R2
20wph_R3
20wph_R4
39wph_R1
39wph_R2
39wph_R3
39wph_R4
H
Transcriptome
39wph / 5wph
H3F3A
RCC2
DPYSL4
DNMT3A
H3F3A
SLC22A23
HMGA1
EZH2
−log10 (adjusted P-value)
Log2 fold change
(39wph/5wph)
I
Reproducibility of protein-transcript decoupling in independent studies
12wph / 5wph
39wph / 12wph
P = 1.88e−40
P = 9.8e−37
R: 0.34
R: 0.27
Prot.-transcr. decoupling (this study)
Prot.-transcr. decoupling (Sacramento et al., 2020)

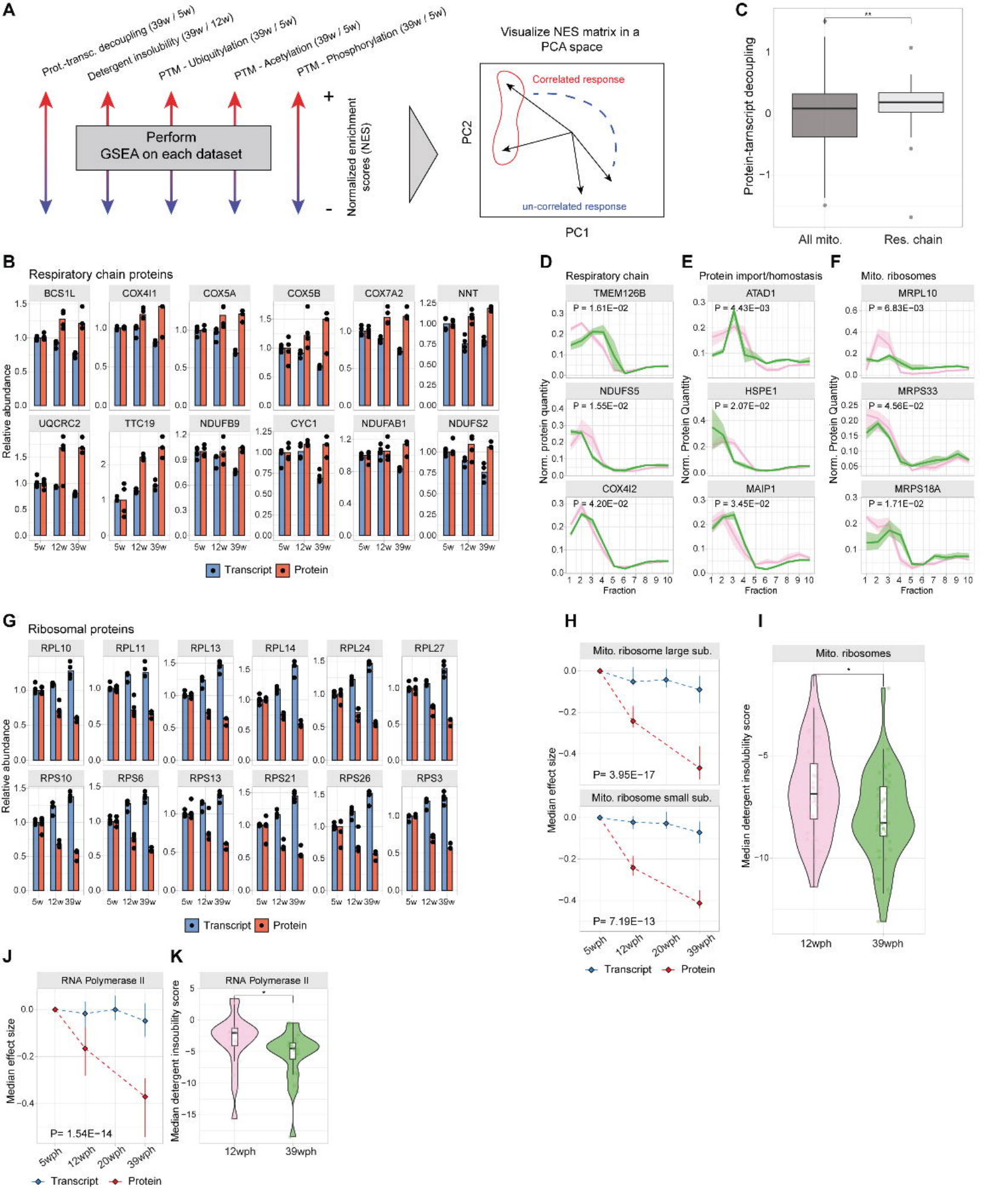
A
Prot.-transc. decoupling (39w / 5w)
Detergent insolubility (39w / 12w)
PTM - Ubiquitylation (39w / 5w)
PTM - Acetylation (39w / 5w)
PTM - Phosphorylation (39w / 5w)
Perform GSEA on each dataset
+
-
Normalized enrichment scores (NES)
Visualize NES matrix in a PCA space
Correlated response
un-correlated response
PC2
PC1
C
Protein-tarnscript decoupling
**
All mito.
Res. chain
B
Respiratory chain proteins
BCS1L
COX4I1
COX5A
COX5B
COX7A2
NNT
UQCRC2
TTC19
NDUFB9
CYC1
NDUFAB1
NDUFS2
Relative abundance
5w 12w 39w
Transcript
Protein
D
Respiratory chain
TMEM126B
P = 1.61E−02
NDUFS5
P = 1.55E−02
COX4I2
P = 4.20E−02
Norm. protein quantity
Fraction
E
Protein import/homostasis
ATAD1
P = 4.43E−03
HSPE1
P = 2.07E−02
MAIP1
P = 3.45E−02
Norm. Protein Quantity
Fraction
F
Mito. ribosomes
MRPL10
P = 6.83E−03
MRPS33
P = 4.56E−02
MRPS18A
P = 1.71E−02
Norm. Protein Quantity
Fraction
G
Ribosomal proteins
RPL10
RPL11
RPL13
RPL14
RPL24
RPL27
RPS10
RPS6
RPS13
RPS21
RPS26
RPS3
Relative abundance
5w 12w 39w
Transcript
Protein
H
Mito. ribosome large sub.
P= 3.95E−17
Mito. ribosome small sub.
P= 7.19E−13
Median effect size
5wph
12wph
20wph
39wph
Transcript
Protein
I
Mito. ribosomes
*
Median detergent insolubility score
12wph
39wph
J
RNA Polymerase II
P= 1.54E−14
Median effect size
5wph
12wph
20wph
39wph
Transcript
Protein
K
RNA Polymerase II
*
Median detergent insoubility score
12wph
39wph

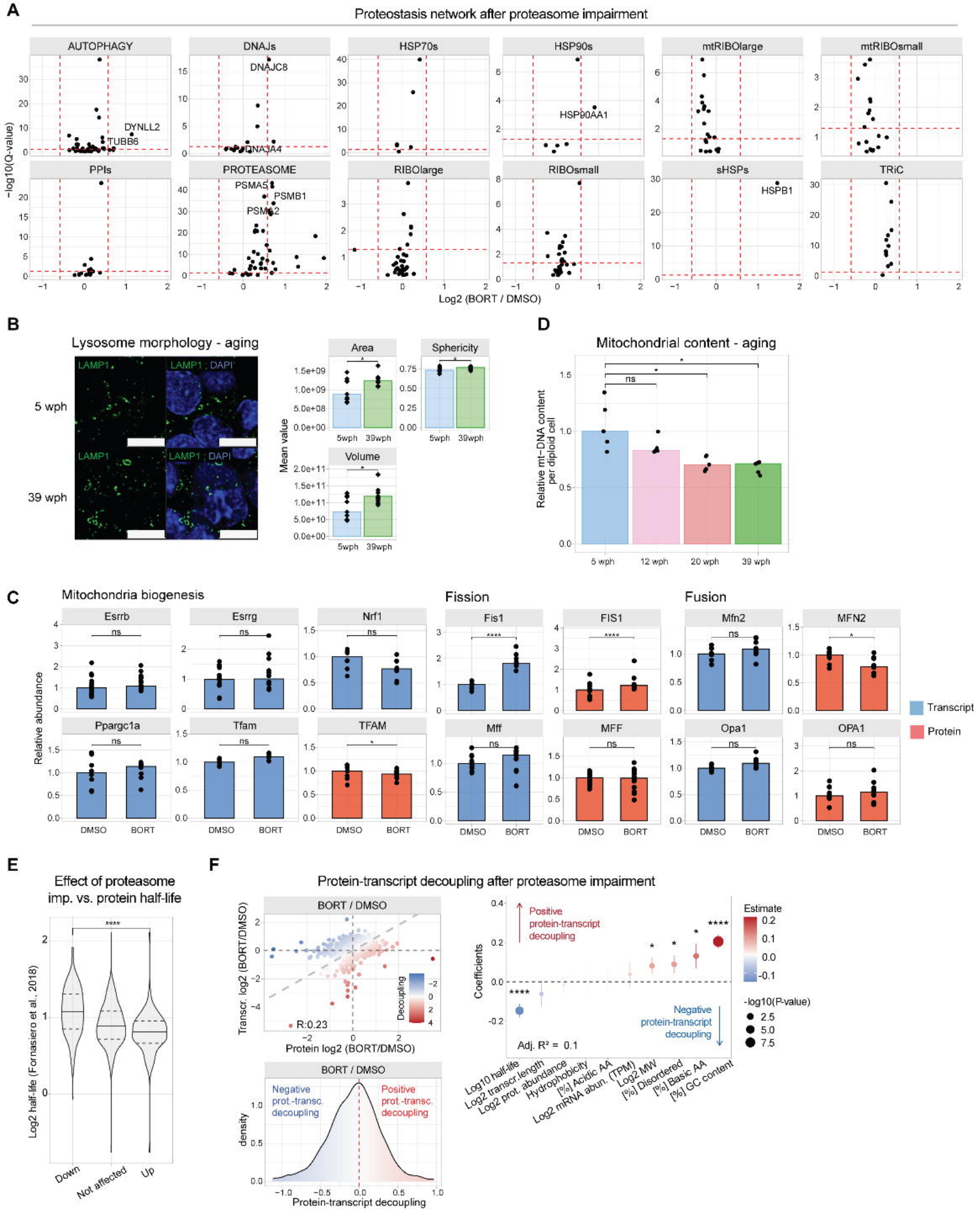
A
Proteostasis network after proteasome impairment
AUTOPHAGY
DNAJs
HSP70s
HSP90s
mtRIBOlarge
mtRIBOsmall
PPIs
PROTEASOME
RIBOlarge
RIBOsmall
sHSPs
TRiC
DYNLL2
TUBB6
DNAJC8
DNAJA4
HSP90AA1
HSPB1
PSMA5
PSMB1
PSMC2
−log10(Q-value)
Log2 (BORT / DMSO)
B
Lysosome morphology - aging
LAMP1
LAMP1 ; DAPI
5 wph
39 wph
Area
Sphericity
Volume
Mean value
5wph
39wph
D
Mitochondrial content - aging
Relative mt−DNA content per diploid cell
ns
5 wph
12 wph
20 wph
39 wph
C
Mitochondria biogenesis
Fission
Fusion
Esrrb
Esrrg
Nrf1
Fis1
FIS1
Mfn2
MFN2
Ppargc1a
Tfam
TFAM
Mff
MFF
Opa1
OPA1
Relative abundance
DMSO
BORT
Transcript
Protein
E
Effect of proteasome imp. vs. protein half-life
Log2 half-life (Fornasiero et al., 2018)
Down
Not affected
Up
F
Protein-transcript decoupling after proteasome impairment
BORT / DMSO
Transcr. log2 (BORT/DMSO)
Protein log2 (BORT/DMSO)
R:0.23
Decoupling
density
Negative prot.-transc. decoupling
Positive prot.-transc. decoupling
Protein-transcript decoupling
Positive protein-transcript decoupling
Negative protein-transcript decoupling
Coefficients
Adj. R² = 0.1
Estimate
-log10(P-value)
Log10 half-life
Log2 transcr. length
Log2 prot. abundance
Hydrophobicity
[%] Acidic AA
Log2 mRNA abun. (TPM)
Log2 MW
[%] Disordered
[%] Basic AA
[%] GC content

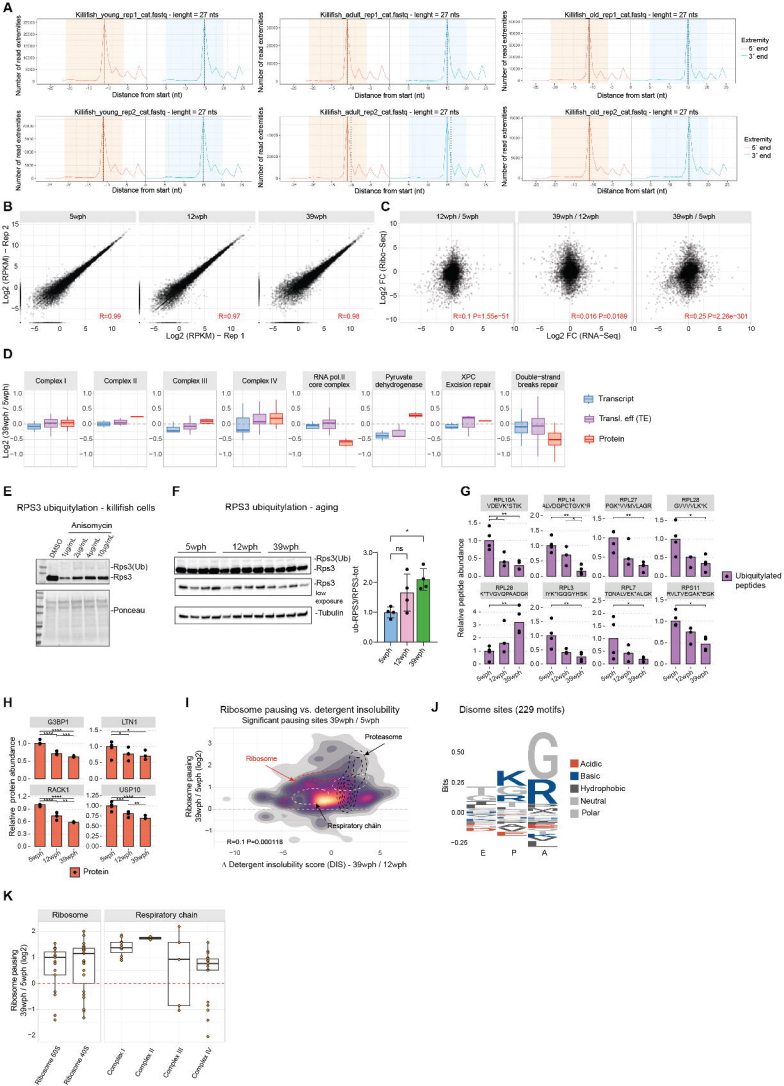
A
Killifish_young_rep1_cat.fastq - lenght = 27 nts
Killifish_adult_rep1_cat.fastq - lenght = 27 nts
Killifish_old_rep1_cat.fastq - lenght = 27 nts
Killifish_young_rep2_cat.fastq - lenght = 27 nts
Killifish_adult_rep2_cat.fastq - lenght = 27 nts
Killifish_old_rep2_cat.fastq - lenght = 27 nts
Number of read extremities
Distance from start (nt)
Extremity
5' end
3' end
B
5wph
12wph
39wph
Log2 (RPKM) − Rep 2
Log2 (RPKM) − Rep 1
R=0.99
R=0.97
R=0.98
C
12wph / 5wph
39wph / 12wph
39wph / 5wph
Log2 FC (Ribo−Seq)
Log2 FC (RNA−Seq)
R=0.1 P=1.55e−51
R=0.016 P=0.0189
R=0.25 P=2.26e−301
D
Complex I
Complex II
Complex III
Complex IV
RNA pol II core complex
Pyruvate dehydrogenase
XPC Excision repair
Double−strand breaks repair
Log2 (39wph / 5wph)
Transcript
Transl. eff (TE)
Protein
E
RPS3 ubiquitylation - killifish cells
Anisomycin
DMSO
1ug/mL
2ug/mL
4ug/mL
10ug/mL
-Rps3(Ub)
-Rps3
-Ponceau
F
RPS3 ubiquitylation - aging
5wph
12wph
39wph
-Rps3(Ub)
-Rps3
-Rps3 low exposure
-Tubulin
ns
*
ub-RPS3/RPS3.tot
G
RPL10A
VDEVK*STIK
RPL14
ILVDGPCTGVKR
RPL27
PGK*VAAVLAGR
RPL28
GVAVVLK*K
RPL29
K*TVGVQRAADGR
RPL3
IYK*TQQGSYHSK
RPL7
TQNALVEK*ALGK
RPS11
RVLTVEGAK*DGK
Relative peptide abundance
Ubiquitylated peptides
H
G3BP1
LTN1
RACK1
USP10
Relative protein abundance
Protein
I
Ribosome pausing vs. detergent insolubility
Significant pausing sites 39wph / 5wph
Proteasome
Ribosome
Respiratory chain
R=0.1 P=0.000118
Ribosome pausing 39wph / 5wph (log2)
Δ Detergent insolubility score (DIS) - 39wph / 12wph
J
Disome sites (229 motifs)
Bits
Acidic
Basic
Hydrophobic
Neutral
Polar
E
P
A
K
Ribosome
Respiratory chain
Ribosome pausing 39wph / 5wph (log2)
Ribosome 60S
Ribosome 40S
Complex I
Complex II
Complex III
Complex IV